DESIGN, FABRICATION, AND CHARACTERIZATION OF PHOTONIC DEVICES ON LITHIUM-NIOBATE-ON-INSULATOR PLATFORM

by

YIJUN XIE

B.E., University of Electronic Science and Technology of China, 2014
M.S., University of Electronic Science and Technology of China, 2017

A thesis submitted to the
Faculty of the Graduate School of the
University of Colorado in partial fulfillment
of the requirement for the degree of
Doctor of Philosophy
Department of Electrical, Computer, and Energy Engineering
2025

Committee Members:
Shu-Wei Huang, chair
Scott Diddams
Juliet Gopinath
Chun-Chieh Chang
Chloe Doiron

Yijun Xie

Design, Fabrication, and Characterization of Photonic Devices on Lithium Niobate on Insulator Platform

Thesis directed by Professor Shu-Wei Huang

The unique combination of exceptional material properties of lithium niobate (LN) including nonlinear optical, electro-optic, acoustic-optic, and piezoelectric with the flexibility of dispersion engineering and strong optical mode confinement of the integrated photonics has made lithium-niobate-on-insulator a prominent platform enabling a wide variety of applications spanning nonlinear optics, telecommunications, quantum optics, and microwave photonics. The integrated fabrication on lithium-niobate-on-insulator platform with high quality is the key to fulfilling the full potential of lithium niobate.

We develop and optimize the fabrication process with electron beam lithography and ion beam mill for lithium niobate, and accurately characterize the quality, the etch depth, and the base angle of the structure to help build simulation models with high fidelity. We also experimentally demonstrate an inversely designed grating coupler featuring -3.8 dB coupling loss with 1-dB and 3-dB bandwidth of 71.7 nm and over 120 nm, respectively, and propose a design with double layer inverse taper to achieve -1 dB coupler loss over 100 nm bandwidth for applications that demand ultra-low loss.

Benefitting from the optimized fabrication process, we also demonstrate a dispersion-engineered micro-ring resonator with pulley-type coupler enhancing coupling strength between bus waveguide and the resonator featuring the loaded quality factor up to 2.2 million, which corresponds to the cavity finesse of over 3000.

Furthermore, we demonstrate highly efficient second harmonic generation with normalized conversion efficiency of 5200%/W/cm^2 in a quasi-phase-matched waveguide by electric field periodic poling. Finally, we demonstrate cross-polarized Stimulated Brillouin Scattering gain on a 14 cm-long waveguide on 450 nm-thick lithium-niobate-on-insulator platform with the normalized Stimulated Brillouin Scattering gain of 17 /W/m.

Acknowledgements

The journey of completing a PhD is a long and transformative experience, one that has tested my perseverance, shaped my academic and personal growth, and inspired me in countless ways. As I stand at the threshold of completing this chapter, I am filled with deep gratitude for everyone who has supported and guided me throughout this arduous yet rewarding journey.

First and foremost, I owe my deepest thanks to my advisor, Dr. Shu-Wei Huang. Without your unwavering guidance, mentorship, patience, and encouragement, this thesis would not have been possible. I am incredibly grateful for all the opportunities you provided and for always believing in my work, even when I doubted myself.

I would also like to express my gratitude to the members of my thesis committee, Dr. Chun-Chieh Chang, Dr. Chloe Doiron, Dr. Juliet Gopinath, and Dr. Scott Diddams, for their constructive feedback, insightful comments, and invaluable guidance.

I am especially thankful to our postdoctoral researchers (now professors in UESTC), Mingming Nie, and Bowen Li, whose guidance and support have been a cornerstone of my academic development. Working alongside you has been an enriching experience. Besides, I would like to thank my ex-colleague Dr. Neeraj Prakash and all my current colleagues, Ghazaleh Hajimazdarani, Jonathan Musgrave, Jan Bartos, Bruno Novak, and Mir Ashib Ullah for your support and your hard work.

I also want to express my greatest gratitude to Anthony James, John Nogan, and Denise Webb for your patience, expertise, willingness to share your knowledge and continuous effort in maintaining a healthy working environment in the cleanroom, which plays such an important role in the completion of my PhD. I also want to thank the other staff members at CINT, Douglas Pete, Michael De La Garza, and Willard Ross for the help you provided as well as all the fantastic researchers I met at CINT, Lala Rukh, Dr. Viktoriia Babicheva, Dr. Hyunseung Jung, Dr. Pingping Chen, Dr. Sueli Skinner, and Dr. Prasad Iyer.

I would also like to thank Dr. Bo Xu, Dr. Michael Greyson, and Bright Lu from Dr. Wounjhang Park's group for fruitful discussions and knowledge in fabrication, Lauren Kennedy and Dr. Tsung-Han Wu from Dr. Scott Diddams's group for the help with periodic poling, and Gregory Kruper from Dr. Juliet Gopinath's group.

I am particularly thankful to all the friends along the way. Your kindness, encouragement, and understanding have been a source of strength when the pressures of PhD life seemed overwhelming.

Most importantly, I would like to express my heartfelt gratitude to my family, who have been my rock throughout this journey. To my parents, Jie Qiu, and Donghui Xie and my grandparents Xiuzhen Xie, Shilong Dong, and Jianquan Wei, thank you for your boundless love, for always believing in me, and for instilling in me the value of education and hard work. Your sacrifices, unwavering faith, and continuous support have been the foundation on which I have built my characters.

Thank you all from the bottom of my heart!

Contents

Chapter

I. Introduction 1

1.1 Bulk lithium niobate and lithium-niobate-on-insulator 1

1.1.1 Bulk LN 1

1.1.2 LNOI 2

1.2 Frequency combs/soliton based on $\chi^{(2)}$ and $\chi^{(3)}$ 3

1.2.1 Dissipative quadratic solitons 4

1.2.2 Parametrically driven dissipative Kerr soliton 6

1.3 Thesis outline 8

II. Development and optimization of fabrication process for LN........... 10

2.1 Mask selection and optimization.. 11

2.2 Etching techniques of LN 15

2.3 Post etching process.. 17

2.4 Etching depth and cross-section characterization....................... 18

2.5 Summary 20

III. Design and fabrication of input/output coupler 22

3.1 Edge coupler 23

3.2 Grating coupler with linear apodization and chirping 25

3.3 Grating coupler by inverse design method 30

3.4 Single layer inverse taper 39

3.5 Doubler layer inverse taper 41

    3.5.1 Design with polymer waveguide 41

    3.5.2 Design with SiO_2 cladding 45

3.6 Summary 48

IV. Dispersion engineered micro-ring resonators 49

4.1 Single-point bus waveguide coupler 50

4.2 Pulley-type coupler 53

4.3 Dispersion engineering 56

4.4 Characterization of micro-ring resonators 58

4.5 Summary 63

V. Second harmonic generation on Z-cut LNOI waveguide 64

5.1 Analytical solution of SHG conversion efficiency 65

5.2 Phase matching 69

    5.2.1 Phase mismatch 70

    5.2.2 Modal phase matching 71

    5.2.3 Quasi phase matching and periodic poling 72

5.3 Refractive indices measurement of LN and design for SHG 74

5.4 Fabrication of waveguides for SHG 76

5.5 SHG characterization 78

5.6 Summary 85

VI. Stimulated Brillouin scattering on Z-cut LNOI 86

6.1 Introduction and motivation 86

6.2 Design of waveguides on Z-cut LNOI... 88

6.3 Fabrication of spiral waveguides on Z-cut LNOI 91

6.4 Cross-polarized SBS gain characterization 92

6.5 Summary 98

VII. Conclusion and outlook 99

7.1 Conclusion 99

7.2 Future work 101

7.2.1 Parametrically driven Kerr dissipative soliton 101

7.2.2 Microwave filter with ultra-narrow linewidth............. 103

Reference.. 106

Tables

Table

3.1. Widths of grating pillars and trenches after optimization……32

Figures

Figure

1.1. Effective third-order nonlinearity vs phase mismatch 5

1.2. Minimal group velocity mismatch under different effective second-order nonlinearity to access soliton............................... 7

1.3. Spectrum comparison at the start and end of 10000 roundtrips .. 8

2.1. SEM image of Al_2O_3 of a grating coupler 12

2.2. Thickness measurement of ZEP 520A by Filmetrics................... 13

2.3. SEM images of grating couplers with different doses 14

2.4. SEM images of micro-ring resonators 15

2.5. SEM images of micro-ring resonators by ICP-RIE 16

2.6. SEM image of micro-ring resonators by ion mill 16

2.7. SEM images of micro-ring resonators after residual mask removal and redeposition removal 18

2.8. AFM trace of a waveguide.. 19

2.9. SEM image of the cross section of a waveguide 20

3.1. Mode profile and cross section of waveguides after dicing and polishing 24

3.2. 2D schematic of grating coupler simulation................................ 27

3.3. Coupling efficiency comparison of 2D and 3D FDTD 29

3.4. Coupling efficiency comparison of grating coupler between uniform grating and with apodization and chirping 29

3.5. Flow chart of grating coupler design by inverse design method . 31

3.6. Coupling efficiency before and after optimization 33

3.7. Fabrication tolerance analysis of the proposed grating coupler.. 34

3.8. SEM images of the fabricated grating coupler............................ 36

3.9. Simulation and experiment results comparison 37

3.10. Mode profile and performance of single layer inverse taper 40

3.11. The simulation schematic of double layer inverse taper 42

3.12. Performance of a double layer inverse taper and SEM images of the fabricated device with polymer waveguide........................ 43

3.13. Mode profile of a double layer inverse taper with SiO2 cladding at different locations 45

3.14. Performance of double layer inverse taper with SiO2 cladding .. 46

3.15. SEM images of the bottom tip and facet 47

4.1. Schematic of single-point bus coupler and its performance 52

4.2. Schematic of pulley-type coupler and its performance 53

4.3. Coupler ratio of pulley-type coupler with different parameters . 55

4.4. GVM of bulk LN and dispersion engineered waveguide 55

4.5. GVD of bulk LN and dispersion engineered waveguide 58

4.6. SEM images of fabricated micro-ring resonator 59

4.7. Experimental schematic of dispersion characterization............. 60

4.8. Transmission and resonance profile of micro-ring resonator 61

4.9. Quality factor, loading factor and GVD of micro-ring resonator. 62

5.1. SHG conversion efficiency vs phase mismatch 70

5.2. Effective indices of FF and SH components of a waveguide 71

5.3. Modal phase matching and mode profiles of FF and SH 72

5.4. Schematic of electric field periodic poling setup 74

5.5. Effective indices of waveguide using different Sellmeier equations 75

5.6. The design of waveguide for SHG 76

5.7. Microscope images of E-beam mask and electrodes 77

5.8. SEM images of waveguides after periodic poling 78

5.9. Experimental schematic of SHG characterization 79

5.10. Experiment and simulation results comparison of SHG 80

5.11. SHG experimental results analysis 82

5.12. Normalized conversion efficiency of SHG comparison with correction dispersion terms 84

5.13. Temperature dependence of conversion efficiency of SHG 84

6.1. Simulated SBS gain with different waveguide orientations 90

6.2. Simulated SBS gain with different waveguide geometries 91

6.3. Microscope and SEM images of fabricated spiral waveguides 92

6.4. Schematic of experimental setup for SBS gain characterization 94

6.5. Measured SBS gain spectra with waveguide top width 2 μm 95

6.6. SBS gain under different pump power 97

6.7. Main SBS gain spectrum with waveguide top width 1.5 μm 97

6.8. SBS gain comparison between simulations and experiments..... 98

7.1. Simulated spectra of PDDKS and microscope image and SEM image of the fabricated micro-ring resonator 102

7.2. Microscope and SEM images of the fabricated EO modulators 104

7.3. Measured modulated voltage output from EO modulators 105

Chapter I

Introduction

1.1 Bulk lithium niobate and lithium-niobate-on-insulator

1.1.1 Bulk LN

Lithium niobate ($LiNbO_3$, LN) is a remarkable and popular material that has been widely used in different applications due to its exceptionally versatile properties: It has large transparency window (0.35 μm to 4.5 μm) and relatively large refractive indices (~2.2 at 1550 nm) making it a good medium for the telecommunications. In nonlinear optics regime, it has very comparable third-order nonlinearity ($\chi^{(3)}$) ($n_2 = 1.8 \times 10^{-19}\ \mathrm{m^2/W}$ at 1550 nm) among other common materials for nonlinear optical devices such as Si [1], SiN [2], and AlN [3], meanwhile it is one of non-centrosymmetric materials possessing strong second-order nonlinearity ($\chi^{(2)}$) ($d_{33} = 27\ \mathrm{pm/V}$ at 1550 nm) making it perfect platform for second harmonic generation (SHG) [4], optical parametric amplifier (OPA) [5], and optical parametric oscillator (OPO) [6]. It also has high electro-optic (EO) coefficient ($r_{33} = 30.9\ \mathrm{pm/V}$) so it works well as high-speed EO modulators [7]. However, apart from being limited by the size of the crystal, it only offers weak optical signal confinement thus reducing the efficiency of optical nonlinear process and being deprived from the capability of dispersion engineering, which is essential to most of the optical nonlinear process. Furthermore, LN's high photo-elastic and piezoelectric coefficients cannot be utilized due to the poor acoustic-optical interactions from its weak surface acoustic wave (SAW) confinement in the bulk LN.

1.1.2 LNOI

With the development and refinement of so called "Smart-Cut" technology [8,9], high-quality LN thin film on Si or sapphire substrates can be manufactured in large volume. With LN thin film sitting on the top of an insulator layer typically SiO_2 whose refractive index is lower than LN on the top of the substrate, the optical signal can be better confined in the layer of LN thin film resulting in minimized propagation on this type of platform called lithium niobate on insulator (LNOI). Thanks to the numerous efforts that have been put in the fabrication of LN, the propagation, scattering, and bending loss have been further optimized in the waveguides and the microresonators making LNOI an even better platform for optical applications compared to bulk LN [10]. Benefitting from the compactness of the integrated photonic components that can be made on LNOI, the power consumption and requirement can be reduced compared to bulk LN.

EO modulator plays an important role in a lot of applications such as optical communications, microwave photonics, computing, and quantum photonics [11,12,13,14]. With LN's large EO coefficient and reduced footprint of the integrated photonic components, LNOI is also a suitable platform for the high-speed EO modulators with high sensitivity and high efficiency [15,22].

Compared to the low surface acoustic wave (SAW) velocity of SiO_2 (~2400 m/s), LN has relatively high SAW velocity (~4000 m/s) making SAW be well confined at the surface of LN once generated without being leaked to SiO_2 substrate enhancing the interaction between optical and acoustic waves inside LN. Therefore, LNOI also becomes a platform for efficient acoustic-optical modulations and frequency shifter [93,94,95,96,97,98,99].

Dispersion engineering, which is a necessity for most of the optical nonlinear process, can be easily achieved on LNOI platform by changing the thickness, etch depth, and the width of the waveguide and the microresonators. Besides, the strength of the optical nonlinear interactions can be significantly enhanced by the reduced small mode area, making LNOI a suitable platform for conventional dissipative Kerr frequency combs/soliton generation unlocking a lot of applications such as dual-comb spectroscopy, optical atomic clock, optical frequency synthesizer, optical ranging and biomedical imaging as other integrated photonics platforms with $\chi^{(3)}$ [25,46,47,48,50,51,52,53,54,55,56,57,58].

What makes LNOI special is that the coexistence of $\chi^{(2)}$ and $\chi^{(3)}$, which most of the conventional $\chi^{(3)}$ platforms do not have, has sparked new mechanisms of soliton generation with reduced threshold power and higher conversion efficiency compared to conventional dissipative Kerr soliton (DKS).

1.2 Frequency combs/soliton based on $\chi^{(2)}$ and $\chi^{(3)}$

While the microresonators are operating close to the phase matching condition between the fundamental frequency (FF) and second harmonic (SH) components where the phase mismatch between those two components is compensated via periodic poling, second-order nonlinearity exhibits an effective third-order nonlinearity consisting of the real part that mimics the behavior of two-photon absorption and the imaginary part that mimics the behavior of Kerr nonlinearity but orders of magnitudes stronger than the material third-order nonlinearity.

Depending on the group velocity mismatch (GVM) between FF and SH components as well as the group velocity dispersion (GVD) of these two components, solitons can be accessed with different mechanisms possessing various advantages over the conventional DKS.

1.2.1 Dissipative quadratic soliton

When the microresonator is operating at group velocity matching point where the group velocity of FF component is the same as it of SH component, the second-order nonlinearity induces a strong effective third-order nonlinearity. When the phase mismatch in a roundtrip between SH and FF components equals $\pm 2\pi$, the real part of the effective third-order nonlinearity, which mimics two-photon absorption, completely disappears while the imaginary part of the effective third-order nonlinearity, which mimics Kerr nonlinearity, is around 20 times of the material nonlinearity as shown in figure 1.1.

This effective Kerr nonlinearity dominates in the Kerr Soliton generation making this process much more efficient, and the soliton state can be accessed with pump power as low as 3 mW [42], called dissipative quadratic soliton (DQS). The soliton state at SH component can also be accessed simultaneously from the back-to-back three-wave mixing processes arising from second-order nonlinearity such as second harmonic generation (SHG), sum frequency generation (SFG), different frequency generation (DFG), and optical parametric generation (OPG) and the cascaded four-wave mixing process with the coexistence of second-order and third-order nonlinearity.

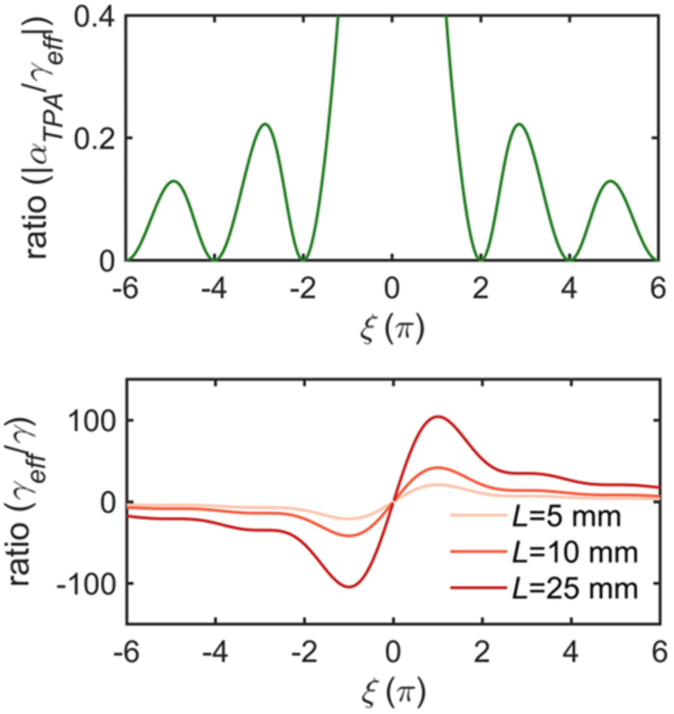

Figure 1.1: The ratio between the effective two-photon absorption and material Kerr nonlinearity and the effective Kerr nonlinearity and material Kerr nonlinearity under different phase mismatch between FF and SH components with different cavity length.

In particular, when the phase mismatch equals -2π, the sign of the effective Kerr nonlinearity has the opposite sign of the material Kerr nonlinearity making the overall Kerr nonlinearity a negative value, which makes the soliton state accessible with normal dispersion of the pump where conventional dissipative Kerr soliton cannot be accessed.

DQS with two solitons at both FF and SH components can be extremely valuable for on-chip f-2f self-referencing system for soliton stabilization. However, DQS requires intensive dispersion engineering to make the group velocity of FF the same as SH. Besides, to utilize the highest second-order nonlinearity d_{33}, transverse-magnetic (TM) modes have to be used for both FF and SH components on the Z-cut LNOI platform making group velocity match between these two components even more difficult.

1.2.2 Parametrically driven dissipative Kerr soliton

After relaxing the requirement of group velocity matching between FF and SH components, the soliton state can still be accessed at FF component when pumped with SH component called parametrically driven dissipative Kerr soliton (PD-DKS). In this case, effective Kerr nonlinearity is much weaker than the material Kerr nonlinearity when the system is operating at the phase matching point between FF and SH components. Effective Kerr nonlinearity induced by effective second-order nonlinearity is considered a perturbance of the system, which is responsible for the higher-order solitons annihilation resulting in deterministic single soliton generation while material Kerr nonlinearity dominates in the system and governs the properties of the generated soliton [41].

Dispersion engineering becomes much easier compared to the case of DQS, in fact, there is a threshold of group velocity mismatch for a specific effective second-order nonlinearity d_{eff} that is adopted. The deterministic single soliton can be accessed only when operating above that threshold group velocity mismatch as shown in figure 1.2.

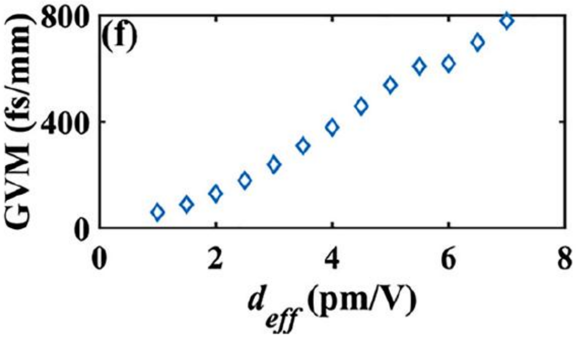

Figure 1.2: Required minimal group velocity mismatch under different effective second-order nonlinearity to access deterministic single soliton state [41].

As shown in the figure, when d_{eff} equals 1.5 pm/V, which is approximately the value when both FF and SH components are selected to be transverse-electric (TE) modes, the minimal group velocity mismatch to access single soliton state is around 100 fs/mm, which can be readily achieved by a lot of micro-ring resonator geometries on Z-cut LNOI platform.

Another main advantage of PD-DKS over DQS is that high quality factor of the micro-ring resonators can be more easily realized since mode confinement of fundamental TE modes is better than fundamental TM modes, which is beneficial to soliton generation with large bandwidth under low pump power. One of the examples is given in figure 1.3, a single soliton with 10-dB bandwidth of 20 THz is achieved with on-chip continuous wave pump power at SH component of only 10 mW.

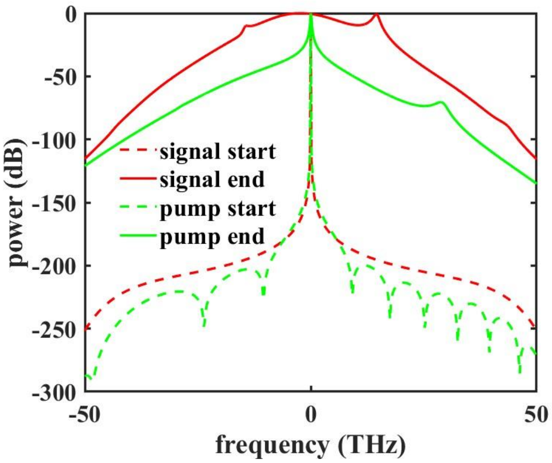

Figure 1.3: Comparison of the spectrum of input pump (SH) and signal (FF), and the output pump (SH) and signal after 10000 roundtrips in the micro-ring resonator.

1.3 Thesis outline

In this chapter, we introduce LN and its exceptional properties over other platforms. Then we talk about how LNOI can extend the advantages of bulk LN and achieve much more. Furthermore, we provide DQS and PD-DKS as rising methods of solitons generation enabled by second-order nonlinearity on the dispersion engineered Z-cut LNOI platform.

Although the fabrication of LNOI remains challenging, there is a yearning need of the fabrication and integration of photonic devices with ultra-high quality on LNOI platform as well as a more reliable way of modeling for the dispersion engineering design and predicting the phase mismatch between SH and FF component more accurately, and the eventual delivery of the design in the fabricated photonic devices to fulfill the full potentials of LNOI platform, and these are the main motivation and what we try to address and solve in this thesis.

In chapter 2, we talk about the optimization of the fabrication process of Z-cut LNOI for high-quality optical devices and the characterization of the quality and the geometry of the fabricated structures, which is the foundation of any photonic devices and their applications.

In chapter 3, we explore and demonstrate different methods for on-chip coupling with large bandwidth and low coupling loss to effectively reduce optical power requirement and consumption.

In chapter 4, we talk about the pulley-type coupler providing high coupling ratio from bus waveguide to the micro-ring resonator, the importance of dispersion engineering and how we achieve it, and the characterization and the demonstration of the micro-ring resonator with high quality factor being the perfect medium for optical nonlinear interactions.

In chapter 5, we first theoretically derive the conversion efficiency of SHG in waveguide and demonstrate high-efficiency SHG in quasi phase matched Z-cut LNOI waveguide through electric field periodic poling paving the way for $\chi^{(2)}$ based nonlinear optical applications.

In chapter 6, we, as one of the first two groups, experimentally demonstrate the cross-polarized Stimulated Brillouin Scattering (SBS) gain on LNOI, which potentially enhances the performance of existing nonlinear optical applications such as soliton generation.

In the last chapter, we summary what we have achieved on LNOI and propose two research directions – parametrically driven Dissipative Kerr soliton and tunable RF filter with ultra-narrow bandwidth that combine advantages of LNOI in different regimes for the foreseeable future.

Chapter II

Development and optimization of fabrication process for lithium niobate

Developing and optimizing the fabrication process of photonic devices on lithium niobate with high quality is the very first step to fulfilling the full potential of the versatile properties of LN in different areas mentioned in the previous chapter. Thanks to the recent development in the commercial manufacturing of thin film lithium niobate on insulator, we purchase the LN thin film with different thicknesses on 2 μm-thick silica (SiO_2) on Si wafer diced into 1 cm^2 chips from NanoLN with decent uniformity in terms of thickness and reduced defects on the thin film.

In this chapter, we will first talk about how the mask for etching LN is selected and the proper condition to pattern the mask with reduced sidewall roughness and critical dimension delivery. Subsequently, we will compare the results of LN etching with different techniques and introduce the development of post-etching process to improve the quality of the fabricated devices. Finally, we will talk about quantitative measurement of the geometry of the fabricated devices to examine whether the design matches with the design, which is directly related to dispersion engineering.

2.1 Mask selection and optimization

The choice and the optimization of the mask is the foundation of having good etching quality as any imperfection will be most likely transferred to the etched structure. Hard masks made of dielectrics or metals generally have good etching resistance providing higher selectivity during etching process. Most of the hard masks will have even less than 1:1 etching selectivity for LN meaning the hard mask must be thicker than 450 nm, which is extremely difficult to acquire, to achieve the etch depth of LN of at least 450 nm to have stronger mode confinement for reduced propagation loss and flexibility of dispersion engineering for different applications.

The only practical choice is aluminum oxide (Al_2O_3) that can provide almost 3:1 selectivity for LN etching. Despite not being etched easily even by inductively coupled plasma reactive ions etching (ICP-RIE), Al_2O_3 can be patterned by the lift-off process: First, a bi-layer of 495 PMMA A6 and 950 PMMA A6 is spin-coated on a LNOI chip and patterned by an electron beam lithography (EBL) system JEOL JBX 6300-fs. Second, a layer of 150 nm-thick Al_2O_3 is deposited on the top of patterned resist using a physical vapor evaporator with the deposition rate of 1 Å/s. Then the chip is dipped in remover PG solvent at 80 °C to remove the resist and Al_2O_3 on top of it, and Al_2O_3 on the top of exposed region will be left on LN. The SEM image of Al_2O_3 mask of a grating coupler structure is shown in figure 2.1.

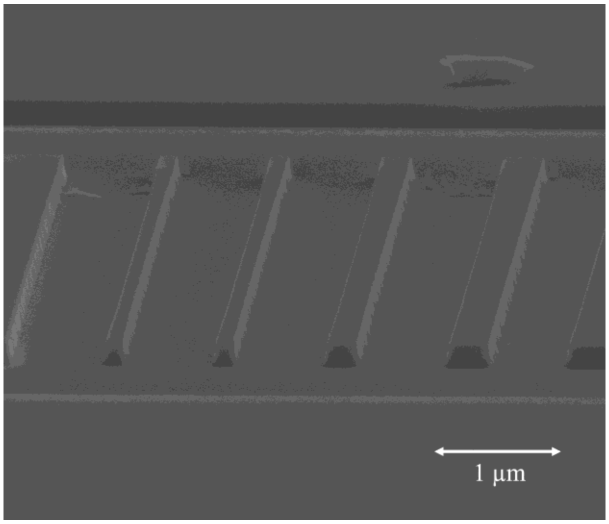

Figure 2.1: SEM image of the Al_2O_3 mask of a grating coupler.

The sidewall Al_2O_3 mask is rough due to the possible damage on the bi-layer resist during the deposition process from the high temperature of evaporating Al_2O_3, which will result in rough sidewall on the devices in the subsequent etching process.

For the soft mask, PMMA is not suitable for the etching process because of its poor etching resistance while ZEP 520A from ZEONREX® has high decent dry etching resistance, high resolution, and high thermal stability. Besides, ZEP 520A supports structure with a large ratio of thickness and width, which is invaluable to deep etching.

To make sure the structures are well protected, during the etching process, we adopt two-step spin-coating procedures to stack up the resist: First layer of ZEP 520A is spin-coated with 3000 rpms at the ramp of 3000 rpm/s for 30 seconds. After 5 minutes of baking at 180 °C for 5 minutes and a 1-minute cooling, another spin-coating with the exact same parameters is conducted, and another 15 minutes of baking at 180 °C to further improve the dry etching resistance of the mask. The total thickness of ZEP 520A after this two-step spin coating is around 873 nm as shown in figure 2.2 measured by Filmetrics with goodness of fit over 98%.

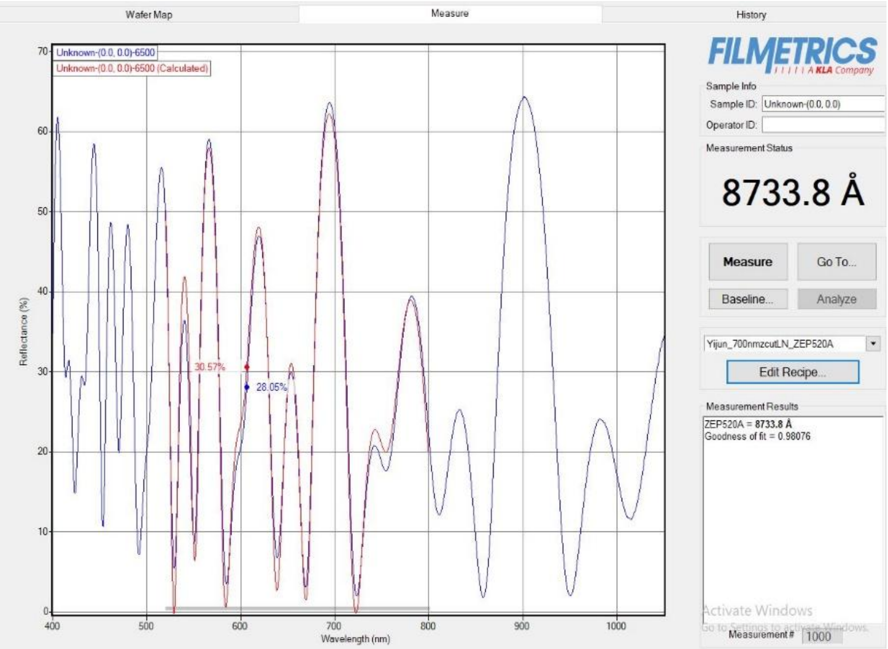

Sample Info

Sample ID: Unknown-(0.0, 0.0)

Operator ID:

Measurement Status

8733.8 Å

Yijun_700nmzcutLN_ZEP520A

Measurement Results

ZEP520A = **8733.8 Å**
Goodness of fit = 0.98076

Measurement # 1000

Figure 2.2: Measured thickness of ZEP 520A on a 700 nm-thick LNOI chip by Filmetrics.

Despite various advantages of ZEP 520A, it is sensitive to the exposure dose during the EBL process, especially for structures with narrow width. Figure 2.3 (a) to (d) depict the SEM images of ZEP 520 A mask of a grating coupler with the exposure dose being high and undercut happens where the bottom width of the structure gets narrower than the top width of the structure due to the scattering of the electrons, with the exposure dose being low where under-exposure happens that some exposed regions remain after development, with the proper exposure dose, and with the proper exposure dose under higher magnification, respectively.

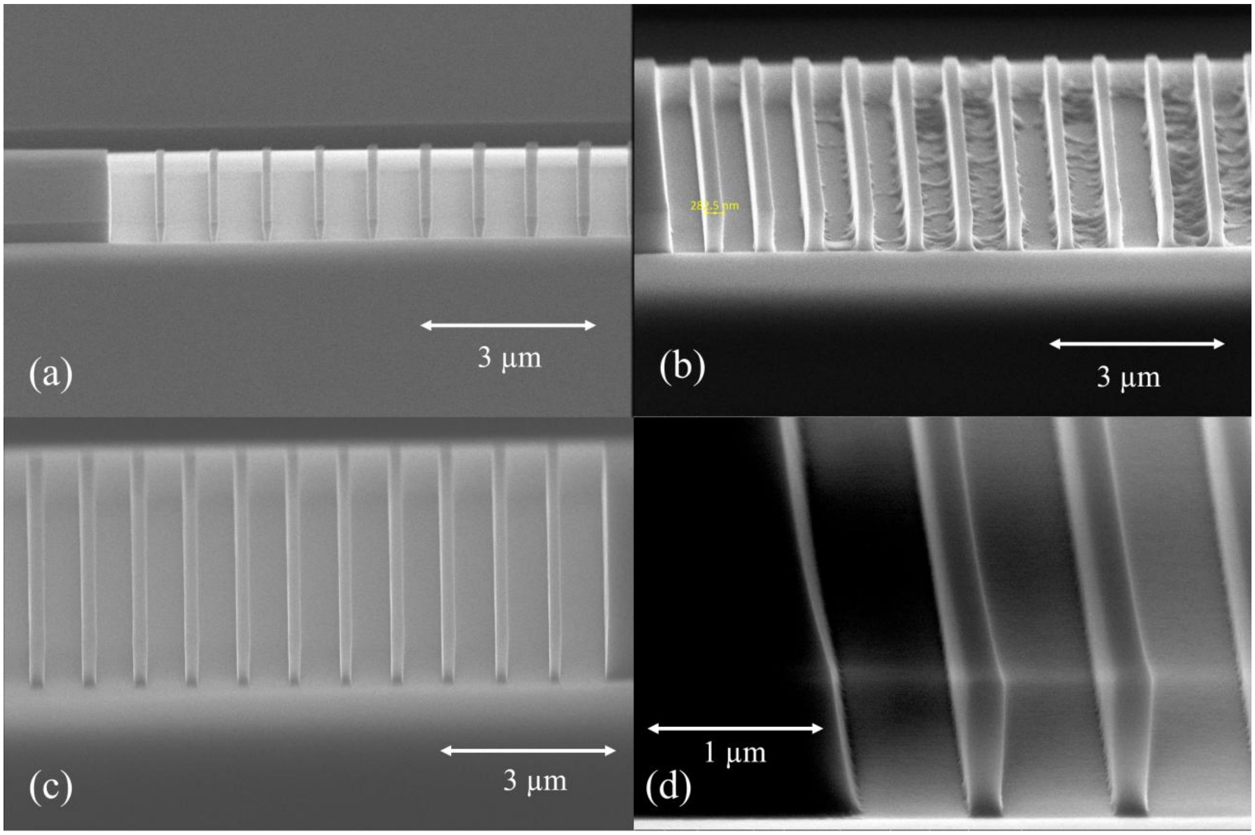

Figure 2.3: SEM images of a grating coupler (a) With high exposure dose resulting in undercut; (b) With low exposure dose resulting in under-exposure; (c) With proper dose; (d) With proper dose under higher magnification.

The proper dose range for such thick ZEP 520A is only 12 μC/cm^2 from 224 μC/cm^2 to 236 μC/cm^2 to avoid any over or under exposure, but the overall quality, especially the sidewall roughness, has been drastically improved from Al_2O_3 mask shown in figure 2.1. Besides, to further reduce the sidewall roughness of the structure and the clearing of the exposed regions, four-pass exposure instead of single-pass exposure strategy is adopted, and figure 2.4 (a) and (b) illustrate the SEM images of ZEP 520A mask on part of the micro-ring resonator with single pass and 4 passes, respectively.

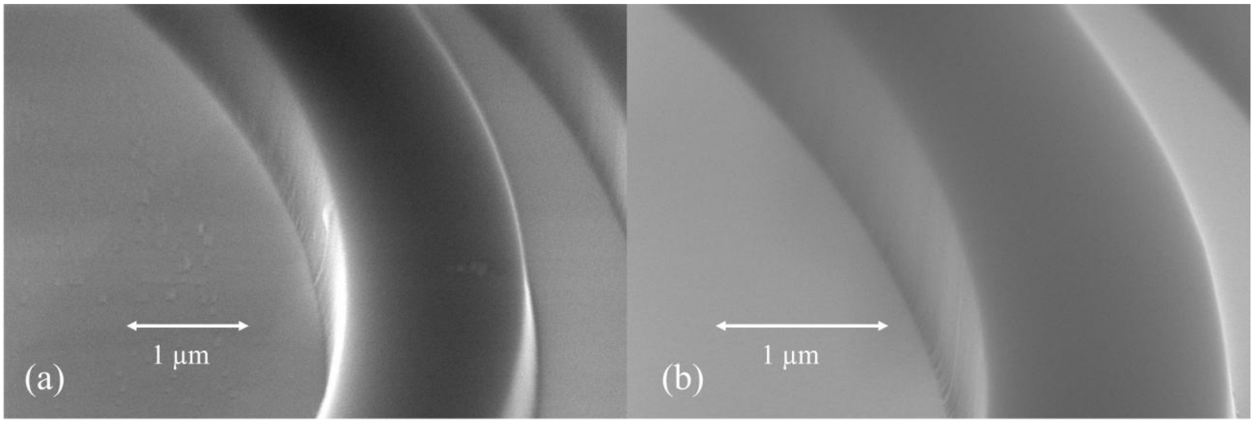

Figure 2.4: SEM images of ZEP 520A mask on part of the micro-ring resonator (a) with single pass; (b) with 4 passes.

2.2 Etching techniques of LN

There is no fluorine-based gas that can provide passivation layer for LN etching in fluorine ICP-RIE to prevent LN from being transverse etched resulting in extremely flat sidewall angle as shown in figure 2.5 (a), while chlorine-based gases erode ZEP 520A mask much faster, and only a thin layer of LN can be etched before mask is completely consumed resulting in rough top surface at edge of the structures as shown in figure 2.5 (b).

Ion mill providing pure physical bombardment etches LN physically with good directionality from accelerated neutralized Argon (Ar) ions that are focus to a-few-centimeter beam. It can etch LN at the etch rate of 25 to 45 nm/s with steep sidewall angle of around 60 to 80 degrees while it etches ZEP 520A mask at a much slower rate without the presence of any chemical reactions. The SEM image on the part of the micro-ring resonator right after ion mill etching for 13 minutes is shown in figure 2.6.

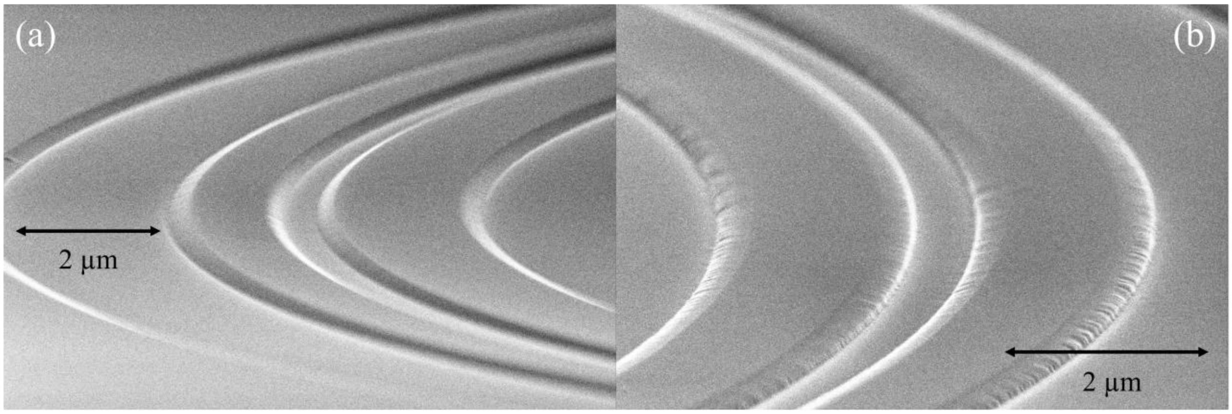

Figure 2.5: SEM images of the micro-ring resonator after redeposition removal (a) etched by fluorine ICP-RIE; (b) etched by chlorine ICP-RIE.

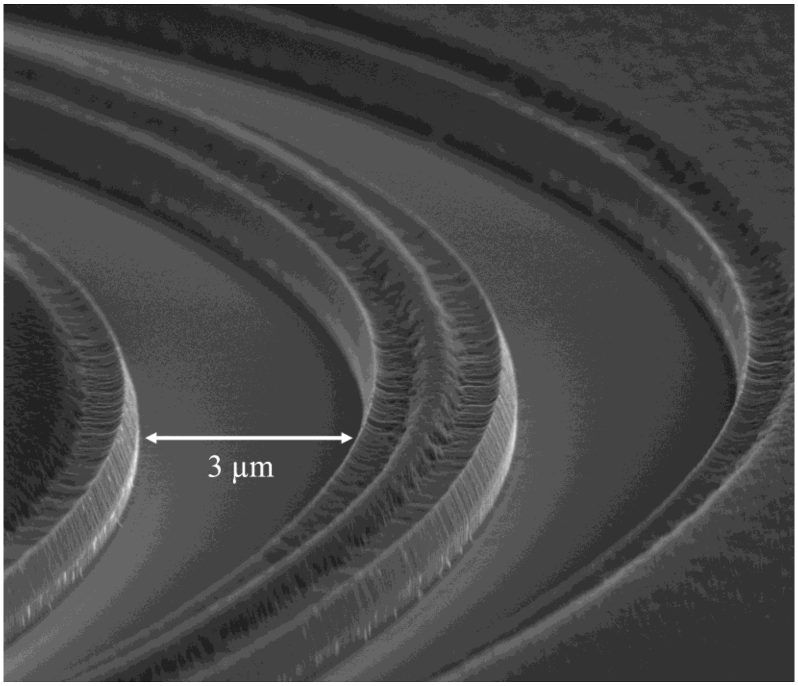

Figure 2.6: SEM image of part of the micro-ring resonator right after ion mill etching for 13 minutes.

After etching, the micro-ring resonator structure gets well protected during the etching process as there is still a good amount of residual ZEP 520A mask left on the top of it. The etched surface shows good uniformity without too much roughness indicating the good etching quality. One thing worth noticing is that ZEP 520A at the edge of all structures gets etched slightly faster than the rest of the structure, therefore, it needs to be taken into consideration when calculating the required thickness of the mask.

2.3 Post etching process

After 13 minutes' etching process, the residual mask gets a little bit carbonized making it hard to be removed by regular method with dipping the sample in remover PG at 75 °C. Instead, we use the ultrasonication machine (sonicator) to create some physical agitation to help the residual mask get detached from LN in the heated remover PG for an entire hour. The SEM image in figure 2.6 (a) depicts the part of the micro-ring resonator after the residual mask removal.

As shown in figure 2.6 (a), the sidewall of all the structures is rough due to the re-deposition of LN during the ion mill etching process that cannot be removed by remover PG. RCA mixture, a mixture of hydrogen peroxide (H_2O_2), ammonia hydroxide (NH_4OH), and de-ionized water (DI water) that is widely used for cleaning process for some wafers, has been proven effective for re-deposition removal for LN [1]. We optimize the ratio of RCA with H_2O_2:NH_4OH:DI water 1:1:5 at process temperature of 65 °C for 20 – 30 minutes depending on the etched depth instead of the RCA ratio of 2:2:1 with the process temperature of 85 °C reported, which is later used in LN etching directly [18].

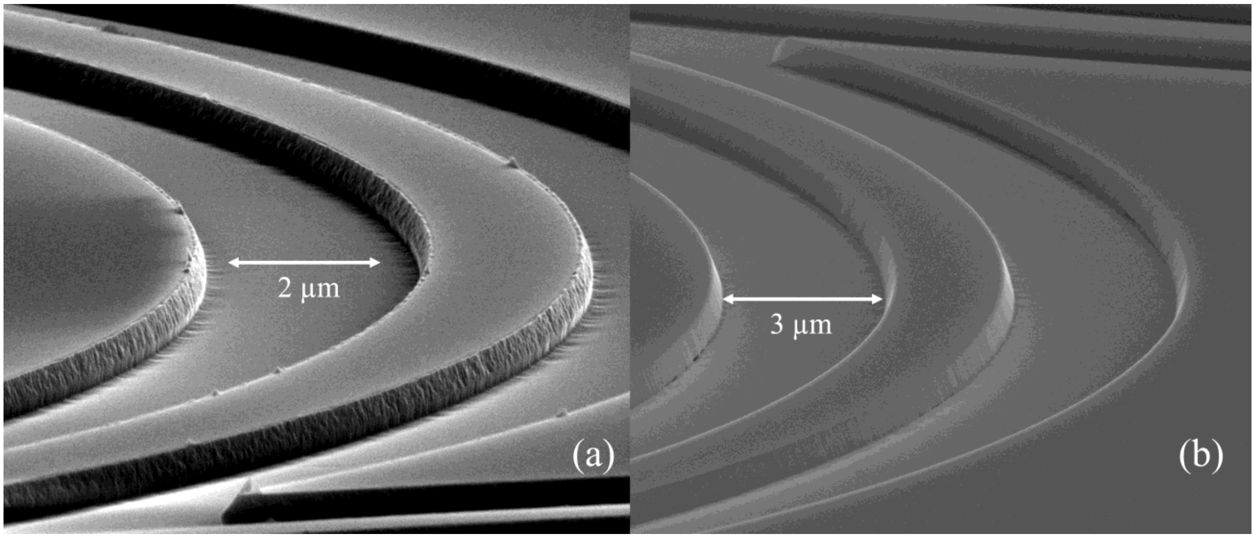

Figure 2.7: SEM image of part of the micro-ring resonator (a) After residual mask removal by heated remover PG in in ultrasonication machine; (b) After re-deposition removal by RCA mixture.

The SEM image of the micro-ring resonator after the re-deposition removal is shown in figure 2.6 (b). After the re-deposition is removed, the real sidewall is revealed, which is much smoother than before the re-deposition removal, and that will be of great help for the reduction of propagation loss for waveguides and microresonators. As clearly shown in figure 2.6 (b), the sidewall is not vertical to the base due to the re-deposition during the ion mill etching process, and it is important to characterize the base angle of the structure so that it can be included in the simulation files to get more authentic designs.

2.4 Etching depth and cross-section characterization

To characterize the etched depth, an atomic force microscope (AFM) is used to scan from one side of the waveguide to another side, and the scan trace is plotted in figure 2.8.

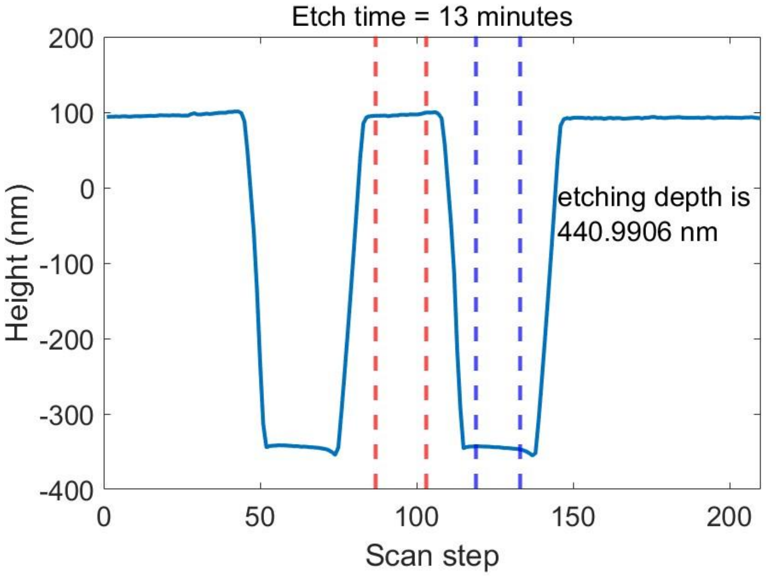

Figure 2.8: AFM trace of a waveguide with etch time 13 minutes.

By calculating the height difference between the top of the waveguide and the trenches on both sides of the waveguides, the total etch depth of around 441 nm in 13 minutes, which corresponds to average etch rate of around 34 nm/min. Noticeably, the sidewall of the waveguide is not vertical even though it cannot be quantitatively calculated from the AFM trace. To measure the exact sidewall angle, a waveguide is cleaved, and the chip is mounted vertically on the SEM chuck so that the dimensions of the exposed facet can be measured more accurately.

While the dimensions measured directly by the in-built tool of SEM might not be accurate due to the uncalibrated pixel size of the image, the SEM image is saved in tiff format, and it is processed in software ProSEM (GenISys). By using the known dimension – the total thickness of LN layer, the pixel size thus other dimensions are calibrated, and the base angle of the waveguide is calculated to be 70 degrees. The SEM image of the cross section of the cleaved waveguide after process with dimensions labeled is shown in figure 2.8.

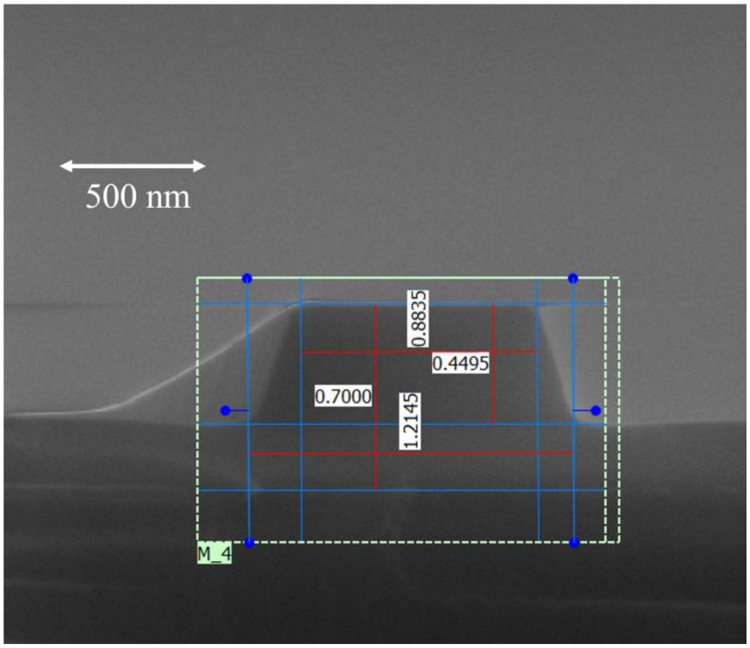

Figure 2.9: SEM image of the cross section of a waveguide processed by ProSEM.

Typically, the rendered base angle of all the structures patterned by the same ion beam mill is similar. This characterized base angle is then applied to all the etched structures in simulation models for photonic devices on LNOI to make the simulation results more reliable.

2.5 Summary

In this chapter, we describe in detail how we develop and optimize the fabrication process of lithium niobate starting from the optimization of soft mask ZEP 520A, the etching of lithium niobate, to the post-etching processes to finally get structures with smooth sidewall and excepted geometry, which is the very basis of the on-chip photonic devices and their applications. At last, we talk about how we measure the etch depth and the sidewall angle accurately, so they can be implemented in the simulation for more authentic photonic devices design.

Chapter III

Design and fabrication of input/output coupler

For almost all on-chip applications based on waveguides and microresonators, input/output coupler is a necessity to bring the optical power onto the chip and extract the power out of the chip for measurement. Couplers with high coupling efficiency, which deliver high on-chip power more efficiently, are favored by applications such as second harmonic generation and optical parametric oscillation whose absolute efficiency is directionally proportional to the on-chip power [19,20,21]. Such couplers are also essential to quantum applications that have stringent requirements on the coupling loss.

Apart from the coupling efficiency, couplers with broad bandwidth that helps retain the spectral information and accommodate the spectral tunability over a large bandwidth are also very important to the applications where broadband transmission and tunability are needed such as supercontinuum generation, tunable lasers, femtosecond pulse generators, dissipative Kerr frequency combs/solitons generation, quadratic solitons, and electro-optic modulators [22,23,24,25,26].

In this chapter, we will first introduce the edge coupler defined by dicing and polishing that is generally suitable for applications with low coupling efficiency requirements. Then, we will talk about the design of a grating coupler optimized by inverse design method featuring -3.8 dB coupling efficiency with 1-dB and 3-dB bandwidths of 71.7 nm and over 120 nm, respectively from the fabricated grating couplers. Finally, we will discuss the design of a double layer inverse taper, a better way to achieve better mode matching on 700 nm-thick LNOI platform, which realizes ultra-high coupling efficiency of sub -1 dB with over 100 nm 1-dB bandwidth.

3.1 Edge coupler

The simplest and the most straightforward way to achieve optical power coupling is through the edge coupler with end-facet coupling setup with either objective lenses or optical lensed fibers. We fabricate a straight waveguide on a 700-nm-thick Z-cut LNOI platform with 450 nm etched depth, 70 degrees base angle, and 1.8 μm top width to match with the mode from lensed fiber purchase from OZ optics along the transverse direction, which is typically 2 μm. The simulated fundamental transverse-electric mode distribution of the waveguide with the cross-section mentioned above is shown in figure 3.1 (a).

The fabricated waveguide is extended to 1 mm away from the edge of the chip on both sides, and we use dicing machine to release the facets 200 μm away from the end of the waveguides. Figure 3.1 (b) depicts the SEM image of the cleaned facet right after dicing, and it is nowhere close to being ready for coupling. The 2-step polishing process is conducted with Allied polishing tool. First, the facet is mounted parallelly to the polishing film of 0.5 μm grain size and polished for 40 minutes under the rotational rate of 25 rpm/min. Second, a fine polishing step with the polishing film of 0.1 μm grain size is taken for only 3 minutes. Third, the polished sample is dipped into RCA solution (1:1:5 of H_2O_2, NH_4OH, de-ionized water) at 65 ℃ for 15 minutes to remove any residual of lithium niobate that is stuck on the facet and the surrounding waveguide. At last, a final cleaning process of remover PG at 70 ℃ for

20 minutes with ultra-sound sonicator is conducted and the SEM image of the polished facet after the cleaning process is shown in figure 3.1 (c).

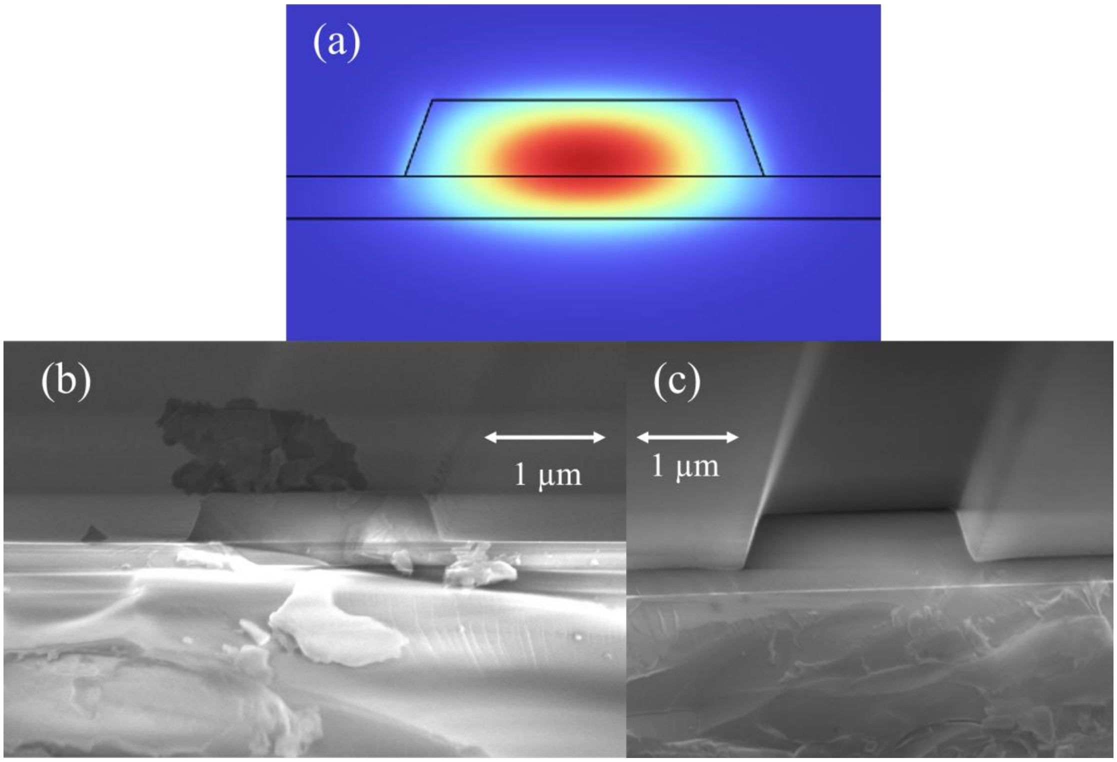

Figure 3.1: (a) Normalized electric field distribution of the fundamental transverse-electric field of the waveguide with 1.8 um top width, 450 nm etch depth, and 70 degrees base angle on a 700 nm-thick Z-cut LNOI platform, (b) SEM of the facet of the waveguide after dicing process, (c) SEM of the facet of the waveguide after polishing process.

The coupling efficiency we can usually get from this edge coupler is -5 dB to -9 dB depending on the quality of the polishing. The coupling efficiency is limited by the mode mismatch between the waveguide and optical lensed fiber along vertical direction even though the perfect matching could be achieved by varying the top width of the waveguide as well as the imperfect polishing. This type of edge coupler does not require specific design. However, it is highly dependent on facets as smooth as possible using polishing tools, which is unfortunately not usually accessible in many the nano/micro fabrication facilities. This type of couplers is not suitable for most of the on-chip applications due to the intrinsic limitation on coupling efficiency.

3.2 Grating coupler with linear apodization and chirping

Grating couplers as one of the better options for coupling offer high coupling efficiency over a large bandwidth. Instead of coupling light from the end-facet, which requires well-polished facets, while grating couplers couple light from the top of the sample making the placement of them very flexible, and the best performance can be obtained with simply single-mode fibers without the need of specialized lensed fiber or objective that provide small spot size and large numerical aperture. Furthermore, the grating couplers can be along with the fiber array, which enables multi-device characterization, improves the efficiency of measurement.

There have been several successful designs and demonstrations of grating couplers with decent performance on lithium-niobate-on-insulator platform with lithium niobate thin film thickness of 300 nm or 400 nm with either bottom metal reflector layer to improve the directionality of power going upwards or patterned over-layer to reduce the refractive index contrast between lithium niobate and the surrounding environment to better extract the power out, which will both impose excessive fabrication complexity compromising the performance and the reliability of the devices [27,28,29,30,31,32]. Despite the good performance in terms of peak coupling efficiency from some of these demonstrations, such grating couplers on thin lithium niobate platform will not be generally compatible with most of the other photonic devices such micro-ring resonators and electro-optic modulators with the lack of good mode confinement and the flexibility of dispersion engineering.

The demonstrated grating coupler compatible with those devices with the best performance so far only provides -6.3 dB peak coupling efficiency with 3-dB bandwidth around 90 nm [33].

Conventionally, the periodicity Λ of a grating coupler is a fixed value given by equation 3.1:

$$\Lambda = \frac{\lambda}{n_{eff} - n_{bg} * \sin\theta} \tag{3.1}$$

where λ, n_{bg}, and θ stand for the center wavelength of the light, refractive index of background material usually being air, and the diffraction angle, respectively. n_{eff} is the effective index of the grating structure defined as shown in the equation 3.2:

$$n_{eff} = F * n_p + (1 - F) * n_e \tag{3.2}$$

where F, n_p, and n_e stand for the filling factor, the effective index of the grating pillar structure, and the effective index of the etched trench structure, respectively. The optimal coupling efficiency can be obtained when the fiber approaches the grating structure aligned with the diffraction angle.

The performance of this grating coupler can be improved by introducing linear apodization where the filling factor is no longer a fixed value for each grating period but a function of coordinate of grating position given by equation 3.3:

$$F(x) = F_o - R * x \tag{3.3}$$

in which F_o, and R represent the initial filling factor and the apodization factor, respectively, describing how the filling factor varies with the position of the grating pitch x with respect to the onset of first grating trench resulting in effective index of each grating period being a function of the grating position as well while the periodicity of each grating period still needs to satisfy equation 3.1. Therefore, the periodicity of each grating period will change accordingly.

We use finite-difference-time-domain (FDTD) provided by Lumerical (Ansys) as our simulation solver. The two-dimensional (2D) view of the schematic of grating coupler simulation is shown in figure 3.2.

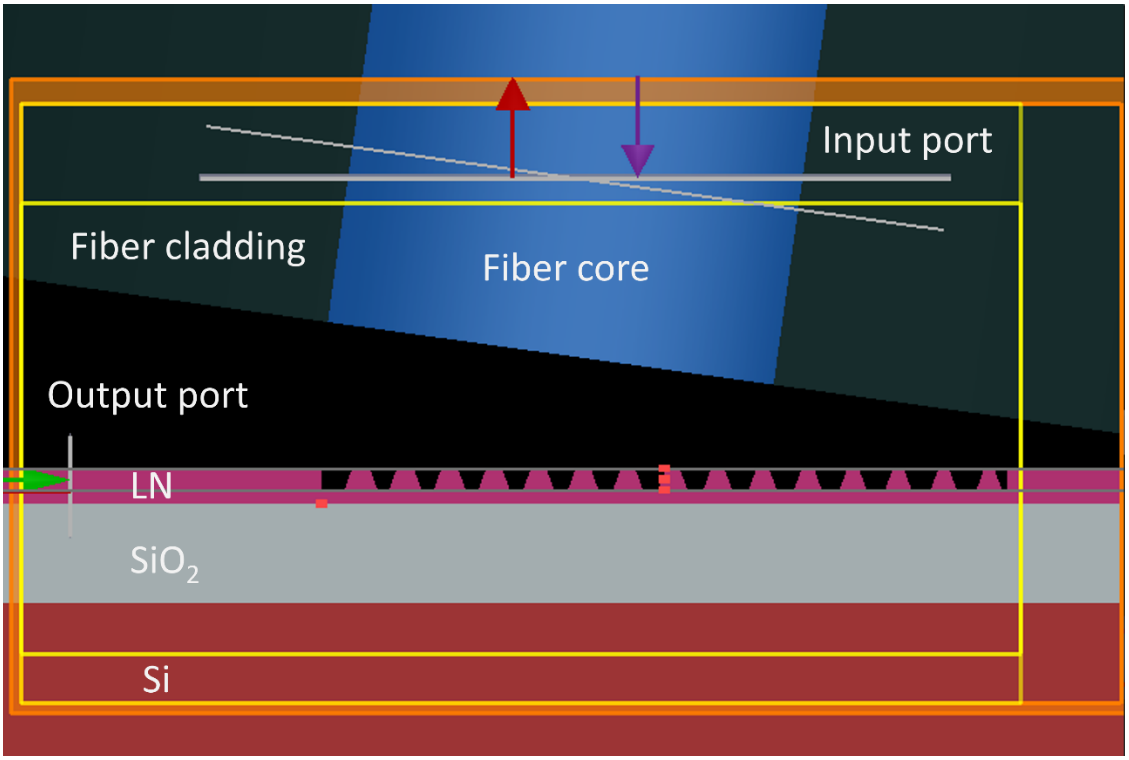

Figure 3.2: 2D view of the schematic of the grating coupler simulation.

As shown in the schematic, the single mode fiber at telecom band is positioned 8 µm above the grating coupler with a tilting angle with respect to the normal direction of the grating coupler that corresponds to the diffraction angle of the grating structure in equation 2.1. The input port is placed at the location of fiber with the same tilting angle and the fundamental transverse-electric (TE) mode as the mode input for the simulation while the output port is placed at the waveguide region to calculate the coupling efficiency of the grating coupler from the fiber.

The total thickness of lithium niobate thin film and etch depth are chosen to be 700 nm and 450 nm, respectively, for the compatibility with other optical devices such as micro-ring resonators. The inevitable base angle of the grating structures 70 degrees, which is characterized by the prior fabricated devices, is also incorporated to ensure the accuracy of the results. The grating coupler structures are closed by a 6 μm-long waveguide on the right-hand side of the simulation region. The length of each grating pillar along the out-of-plane direction in the schematic, which is also the top width of the waveguide, is set to be 12 μm to better match the mode of the fiber along that direction. This length is at least 15 times longer than the width of grating pillars along the in-plane direction, which is typically 300 nm to 500 nm, making the slab waveguide approximation stand so that the simulation results given by three-dimensional (3D) FDTD are almost the same as the results provided by 2D FDTD as illustrated in figure 3.3.

For the optimization, the tilting angle and the position of the fiber are swept for each apodization factor to find out where the best performance occurs for each apodization factor which will be subsequently swept to maximize the coupling efficiency.

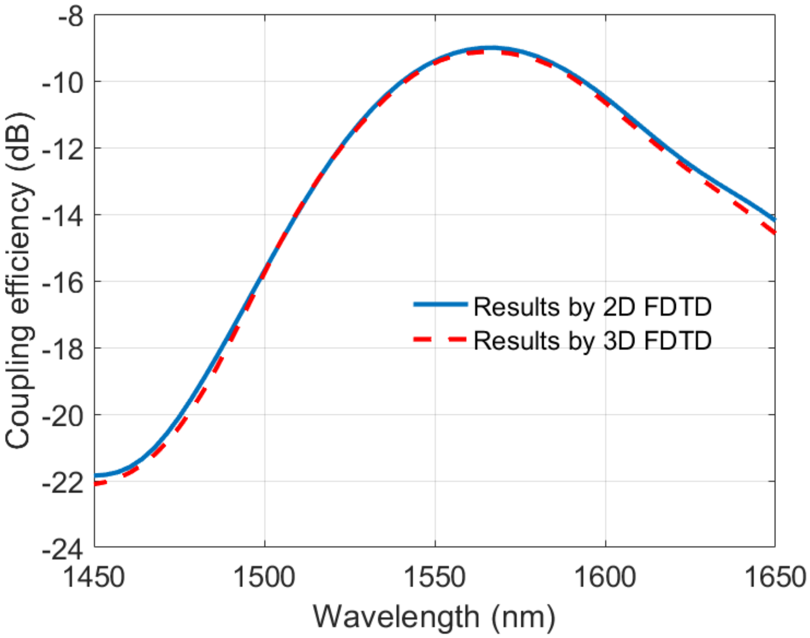

Figure 3.3: Comparison of the results provided by 2D FDTD and 3D FDTD of grating coupler.

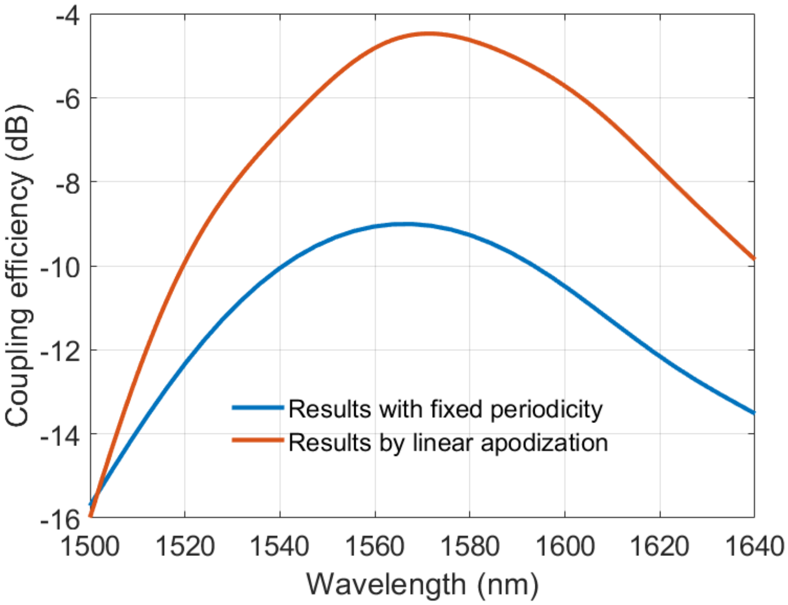

Figure 3.4: Comparison of the results between the grating coupler with fixed periodicity and filling factor and the one with linear apodization and chirping after optimization.

Figure 3.4 depicts the coupling efficiency comparison between the grating coupler with fixed periodicity and filling factor and the one with linear apodization and chirping after optimization.

Although the peak coupling efficiency is improved from -9 dBm to almost -4 dBm without the degradation of the bandwidth, the optimization is limited by the restriction of the dimensions of all grating structures dictated by equation 3.1.

3.3 Grating coupler by inverse design method

On the top of the optimized design with linear apodization and chirping, we incorporate inverse design method based on gradient descent algorithm to further optimize the grating coupler [34]. There are two conditions we set up first for the entire optimization process to ensure the reliability of the design: first, we enforce all the grating structures to be strips with the characterized base angle 70 degrees and the same etch depth 450 nm so that abstract structures can be avoided and all the grating structures can be defined in only single set of e-beam lithography and etching process. Second, we add hard constraint on the minimal feature size of 150 nm to avoid imposing further challenges on fabricating the device [35,36].

We then grant lift the constraint of limiting the dimension of each grating pillar and trench so that they can be changed independently as long as they are larger than 150 nm to further optimize the figure of merit (FOM) defined as the negative value of the average coupling efficiency over a bandwidth of our interest, which is chosen to be 1555 nm to 1595 nm with the frequency interval of 0.8 nm (51 frequency points in total) as defined in equation 3.4:

$$FOM = -\frac{\sum_{i=1}^{N} CE_i}{N}. \tag{3.4}$$

where CE_i stands for the coupling efficiency at frequency point i. The tilting angle of the fiber is fixed at 6 degrees, and the position of the fiber is fixed as well since the relative location of all the grating structures can be changed with respect to the center of the fiber.

We start off with calculating the FOM of the initial design from previous section and then calculate the gradient of FOM with respect to each grating pillar and trench dimensions with the assist of adjoint method, which enables fast gradient evaluation with only two 2D FDTD simulations regardless of the number of parameters. Then the system will evaluate whether the stopping criteria, which is set to be FOM equals -0.5, is met. If not, the widths of each pillar and trench will be changed accordingly based on the minimizer and based on which will FOM be calculated again.

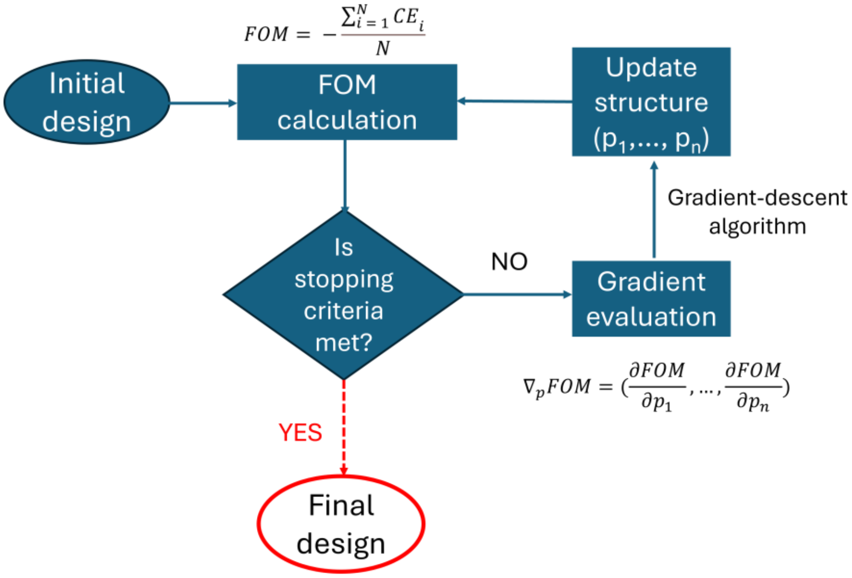

Figure 3.5: Flow chart of grating coupler optimized by inverse design method.

This optimization procedure will run iteratively until the stopping criteria is met or the global minimum is reached as shown in figure 3.5. The dimensions of all the grating pillars and trenches with the final FOM as listed in table 3.1.

Table 3.1 The dimensions of grating pillars and trenches after optimization based on inverse design.

Trench size (nm)	t_1	t_2	t_3	t_4	t_5	t_6	t_7	t_8
	285	542	859	726	684	681	685	670
	t_9	t_{10}	t_{11}	t_{12}	t_{13}	t_{14}	t_{15}	
	601	678	634	644	606	659	722	
Grating size (nm)	w_1	w_2	w_3	w_4	w_5	w_6	w_7	w_8
	302	157	161	230	272	248	257	295
	w_9	w_{10}	w_{11}	w_{12}	w_{13}	w_{14}	w_{15}	
	253	280	252	210	196	175	6000	

As shown in the table, the minimal structure size is 157 nm, which is not super difficult to fabricate such structure with good quality. Furthermore, the tilting angle and the position of the fiber with respect to the grating coupler are subsequently swept to ensure the best performance has been achieved. The peak coupling efficiency of -2.94 dB loss at 1572. 4 nm with 1-dB and 3-dB bandwidths of 69 nm and 113 nm, respectively, is obtained when the fiber is 6 μm away from the first trench of the grating coupler with the tilting angle of 8 degrees.

Compared to the optimized grating coupler design with linear apodization and chirping, the grating coupler by inverse design method has seen 42 %, 56 %, and 37 % improvement in the peak coupling efficiency, 1-dB bandwidth, and 3-dB bandwidth, respectively, as shown in figure 3.6.

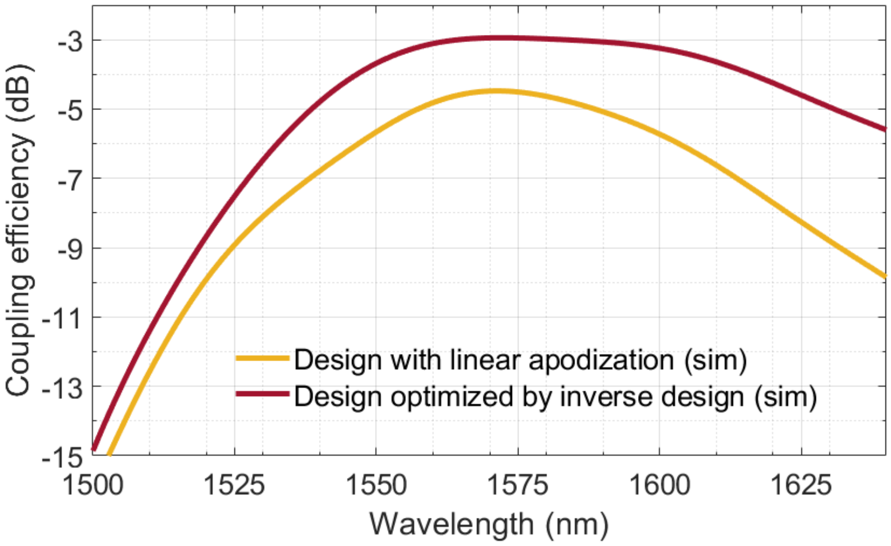

Figure 3.6: Simulated performance comparison between the grating coupler with linear apodization and chirping and the grating coupler optimized by inverse design method.

To examine the fabrication tolerance of the this grating coupler, we the peak coupling efficiency and the 1-dB bandwidth are calculated with the etch depth varied from 400 nm to 500 nm (designed value 450 nm) with fixed base angle of 70 degrees, the base angle varied from 60 degrees to 80 degrees with fixed etch depth of 450 nm (designed value 70 degrees) given that different etching tools will render different base angle for the grating structures, as well as independent random dimension variation on each grating pillar and trench from ±1 % to ±5 % (every ±1 %) to their designed values, which is very common on the mask defined by electron beam lithography (EBL) process, whose results are obtained from 100 individual simulations for each level of dimension variation while the etch depth and base angle are fixed at their designed values, respectively. The effect of different etch depths, base angles, and random dimension variations on the peak coupling efficiency, and 1-dB bandwidth are illustrated in figure 3.7 (a) to (f), respectively.

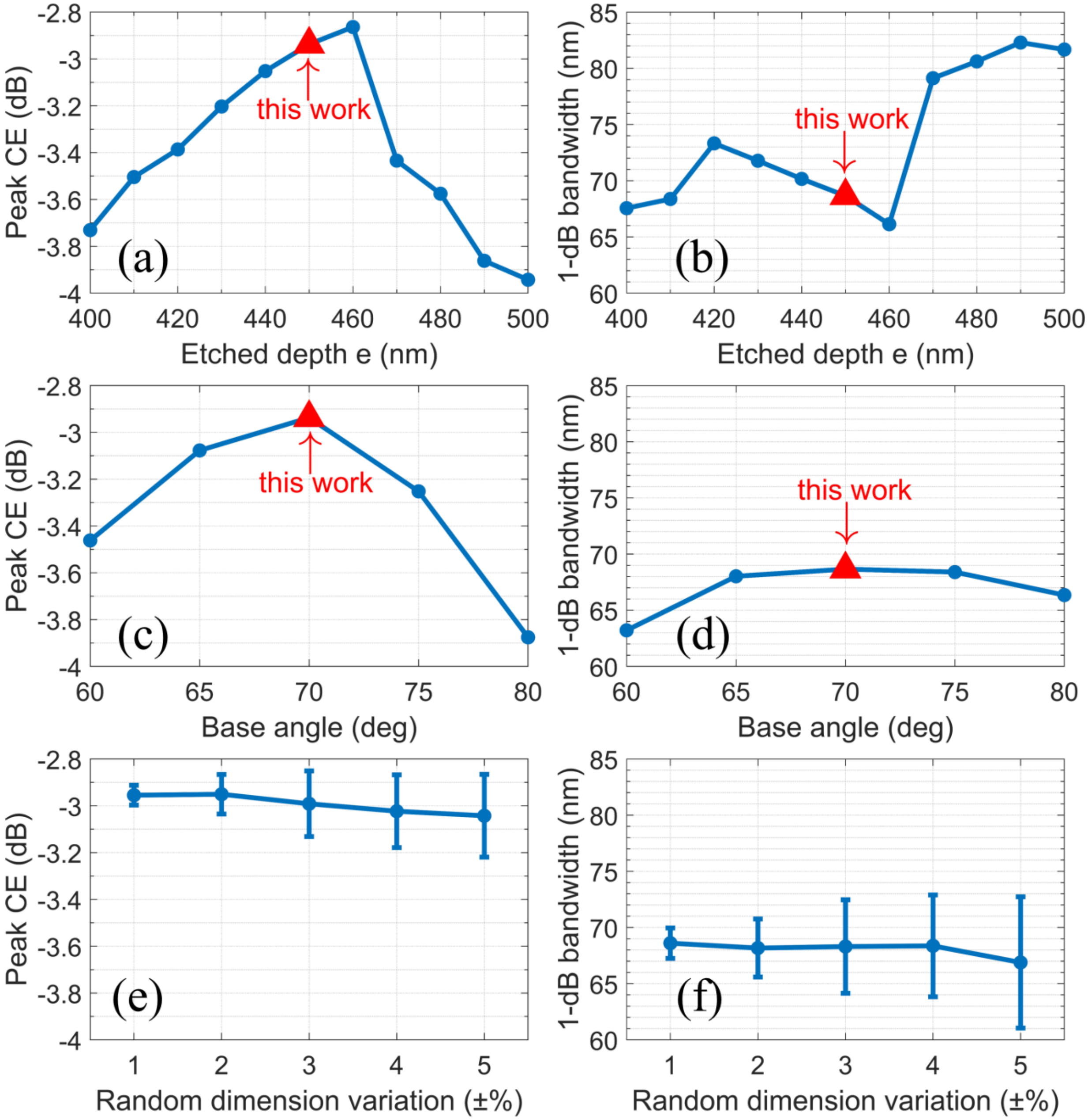

Figure 3.7: The effect of etch depth on (a) the peak coupling efficiency, (b) 1-dB bandwidth; the effect of base angle on (c) the peak coupling efficiency, (d) 1-dB bandwidth; the effect of random dimension variation on (e) the peak coupling efficiency, (f) 1-dB bandwidth.

As shown in figure 3.7 (a) and (b), the peak coupling efficiency varies from -3.9 dB to -2.85 dB, while the 1-dB bandwidth varies from 66 nm to 82 nm with the opposite trend when the etch depth changes from 400 nm to 500 nm and the base angle is fixed at 70 degrees. The performance remains almost unchanged when the base angle is between 65 degrees and 75 degrees when the etch depth is kept at 450 nm as shown in figure 3.7 (c) and (d). However, the performance starts to decay rapidly as the base angle deviates more from the designed value, and the peak coupling efficiency drops nearly by -1 dB when the base angle approaches 80 degrees while 1-dB bandwidth narrows by 6 nm when the base angle gets closer to 60 degrees.

On the other hand, the performance of the designed grating coupler is not affected by the random dimension variations too much as shown in figure 3.7 (a) and (b). There is only 0.3 dB of additional coupling loss, and 8 nm of 1-dB bandwidth reduction, respectively, for the most extreme cases where the random dimension variation reaches ±5%, indicating high fabrication tolerance of the design.

The designed grating coupler is then fabricated for characterization on a 700 nm-thick Z-cut LNOI chip purchase from NanoLN with the optimized fabrication process described in the previous chapter. Each device consists of a 100 μm-long waveguide in the middle with the top width of 1.8 μm, 300 μm-long tapers expanding the top width of the waveguide from 1.8 μm to 12 μm adiabatically on both sides of the waveguide, and two designed grating couplers.

To compare the performance of the grating coupler by inverse design method and the one with linear apodization and chirping, a few devices based on the design with linear apodization and chirping (the initial design for the optimization by inverse design method) are fabricated on the same chip with the exact same waveguide and tapers. The top view and the side view of the SEM images of the fabricated grating coupler are shown in figure 3.8 (a) and (b), respectively.

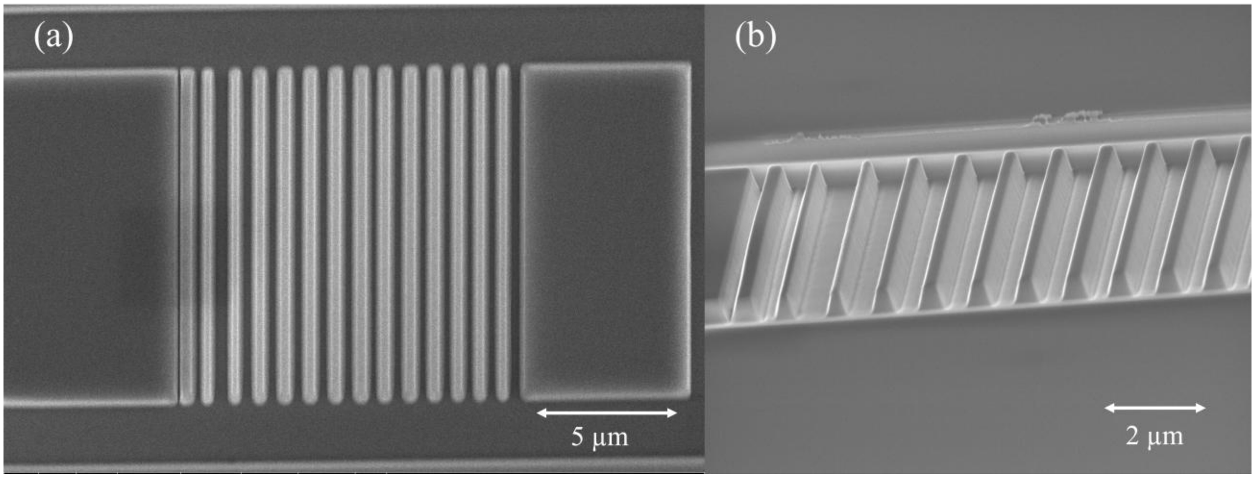

Figure 3.8: The SEM images of fabricated grating coupler by inverse design method (a) top view; (b) side view.

For the measurement of coupling efficiency of the fabricated grating couplers, two SMF-28s are cleaved and clamped onto two rotational stages so that the tilting angle can be adjusted to the designed value with respect to the normal direction of the grating coupler. These two rotational stages are mounted vertically to two three-axis translation stages, which are placed on the opposite side of the fabricated devices. A polarization controller connects between the input optical fiber from the tunable laser source Santec TSL-710 and the input SMF-28 on the translation stage to ensure the input optical mode is TE polarized, while the output SMF-28 is connected to an InGaAs photodetector whose output signal is subsequently collected by a digitizer (CSE1222 Razor Express, Gage) with 100 Ks/s sample rate for the data acquisition.

Santec is continuously scanned from 1500 nm to 1640 nm at the scan rate of 100 nm/s with 5 dBm nominal optical output power. Then the collected data from the digitizer is converted then converted back to optical power from the electrical-optical signal conversion. The coupling efficiency can be calculated by simply divide the total coupling loss in logarithm scale by 2 after the calibration from the calibrated output power from Santec and excluding the losses introduced by two SMF-28s (the propagation loss of the connecting waveguide and two tapers is neglected).

For comparison purpose, the simulated and the measured coupling efficiency before and after the moving average process of the grating coupler with linear apodization and chirping are shown in figure 3.9 (a).

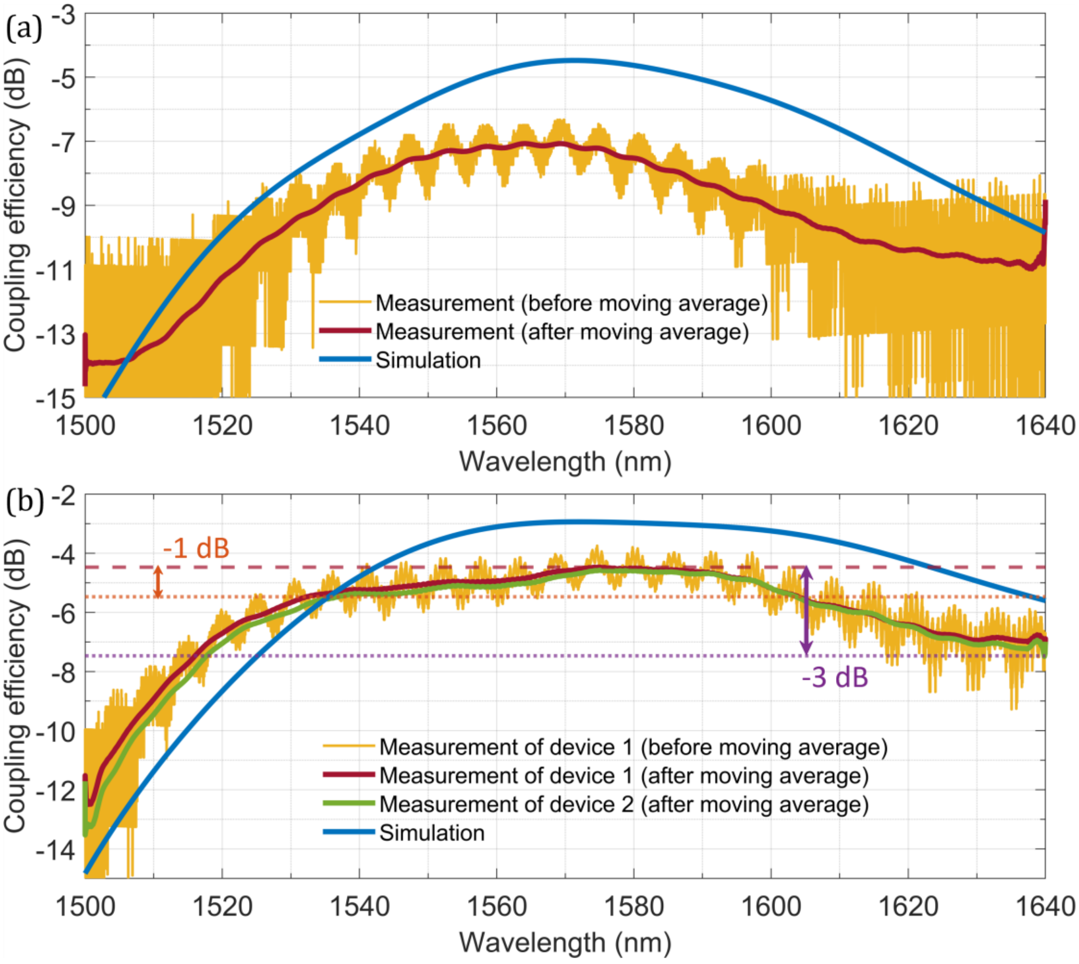

Figure 3.9: The comparison between simulated and measured coupling efficiency (a) grating coupler with linear apodization and chirping; (b) grating coupler optimized by inverse design method.

For the fabricated waveguide with linear apodization and chirping, the 1-dB and bandwidth of 45.7 nm is even better than the designed value 34 nm while the 3-dB bandwidth of 85.8 nm is slightly better than the designed value 84 nm. However, there is a large discrepancy on the peak coupling efficiency between the simulation and the measurement with the measured peak coupling efficiency being -6.33 dB (-7.1 dB ± 0.77 dB from the moving average process), which has around -2 dB additional loss compared to the simulation prediction. This discrepancy mainly comes from fabrication imperfection due to the placement of this device being close to the edge of the chip.

Compared to the results of grating coupler with linear apodization and chirping, the performance of the grating coupler optimized by inverse design, which is shown in the orange curve before the moving average process and red curve after the moving average process in figure 3.9 (b), has been improved comprehensively. The peak coupling efficiency increases from -6.33 dB to -3.8 dB (-4.5 ± 0.7 dB from the moving average process) with 1-dB and 3-dB bandwidth expanding from 45.7 nm to 71.7 nm and 85.8 nm to over 120 nm, respectively. Besides, the measured results are quite comparable to the measured results with less than 1 dB difference in the peak coupling efficiency and slightly wider 1-dB and 3-dB bandwidth, which can be explained by the fabrication error as well as the random dimension variation.

The performance of another grating coupler that is fabricated on a different chip with the exact same process flow is also characterized as shown in the green curve in figure 3.9 (b). It has similar performance compared to the red curve which proves good tolerance on the random dimension variations on the grating structures.

The interference fringes in the measurement results are coming from the back-reflection from the Fabry-Pérot (FP) cavity formed from the back-to-back grating couplers configuration at both ends of the device. This reflection is as weak as -18 dB in the wavelength range of 1520 nm to 1620 nm while it reaches almost -10 dB at 1500 nm, which is at the same level of the recently published work [31].

3.4 Single layer inverse taper

After the optimization of inverse design method, the proposed grating coupler provides decent coupling efficiency over a large bandwidth. However, -3.8 dB peak coupling loss might not be good enough for some quantum related applications that have little tolerance for the coupling loss. To achieve even higher coupling efficiency, better mode matching must be obtained between the mode output from either the lensed fiber or objective and the mode of the waveguide on chip.

In contrast to forward taper in the introduction of edge coupler in section 3.1, one can adiabatically reduce the top width from the center of the chip to the edge of the chip where the optical mode will be loosely confined in the waveguide region. With the help of top cladding with the material with higher refractive index such as SiO_2 and SiON to further reduce the mode confinement of the waveguide thus potentially achieving better mode matching [37,38].

There have been some successful demonstrations on 250 nm-thick Si platforms where a single-layer inverse taper is patterned with one set of EBL and etching process with top width around 40 nm achieving better than -1 dB coupling efficiency per facet for both transverse-electric (TE) and transverse-magnetic (TM) modes over 80 nm bandwidth [39].

However, this single-layer structure cannot work on 700 nm-thick LNOI platform. First, deep etch all the way through LN layer is extremely challenging for such thick LNOI platforms given that LN is hard to etch as discussed in the previous chapter. Second, even if the deep etching of 700 nm is feasible, the quality of the taper structure will be severely compromised, especially at the taper tip region rendering additional scattering loss from the poor quality. Furthermore, due to the inevitable base angle of the etched structures of LN, minimal base width will get wider as the etching goes deeper resulting in better mode confinement hence worse mode matching with the input/output coupling system. Figure 3.10 (a) depicts the normalized electric field of TE eigenmode of the taper tip made of LN with top width of 100 nm, etched depth of 700 nm, and base angle of 70 degrees surrounded completely by SiO_2. The mode profile indicates that most of power is trapped inside the LN tip region, which will have a large mode mismatch between the incoming optical mode from the coupling system.

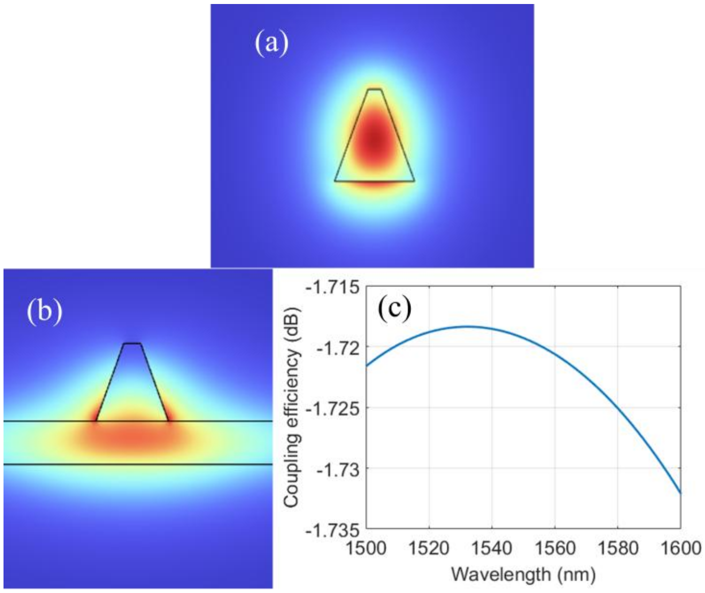

Figure 3.10: (a) Normalized electric field of TE eigenmode of LN taper tip with total thickness 700 nm, etch depth 700 nm, top width 100 nm, and base angle 70 degrees; (b) Normalized electric field of TE eigenmode of LN taper tip with total thickness 700 nm, etch depth 450 nm, top width 100 nm, and base angle 70 degrees; (c) The simulated coupling loss between the input Gaussian beam with beam radius 0.5 μm and the LN taper tip in (b).

The mode confinement can be slightly reduced by making the etch depth shallower to 450 nm while the top width and base angle of the taper tip remain the same as shown in figure 3.10 (b). However, the simulated coupling loss between such structure and the input Gaussian beam with the beam radius of 0.5 μm, which is already below the diffraction limit, can be still as high as -1.72 dB with the assumption that the taper tip facet is perfectly smooth as shown in figure 3.10 (c). To achieve better mode matching, the dimension of the taper tip at the facet needs to be reduced.

3.5 Double layer inverse taper

For the double layer inverse taper for the ridge waveguide with an unetched slab underneath the ridge, the idea is to convert the mode adiabatically from the waveguide of interest to what is shown as figure 3.10 (b) at the end of the top layer of the taper structure where the mode is mostly confined in the unetched slab region. Then the width of the bottom taper will be adiabatically narrowed to the point where the mode can no longer be tightly confined inside the taper with the assist of the top cladding or a waveguide made of a different material with lower refractive index, instead, the mode size is much larger than the physical dimension of the bottom taper tip to achieve better mode matching with the coupling system thus improving coupling efficiency.

3.5.1 Design with polymer waveguide

The simulation schematic of the double layer inverse taper is shown in figure 3.11. To capture the whole double layer taper structure in a single figure for the better understanding of the construction of it, the lengths of the top and bottom taper are both shortened to 10 µm while the actual lengths of the top and the second segment of the bottom taper are 150 µm and 250 µm, respectively, which are restored for the simulations.

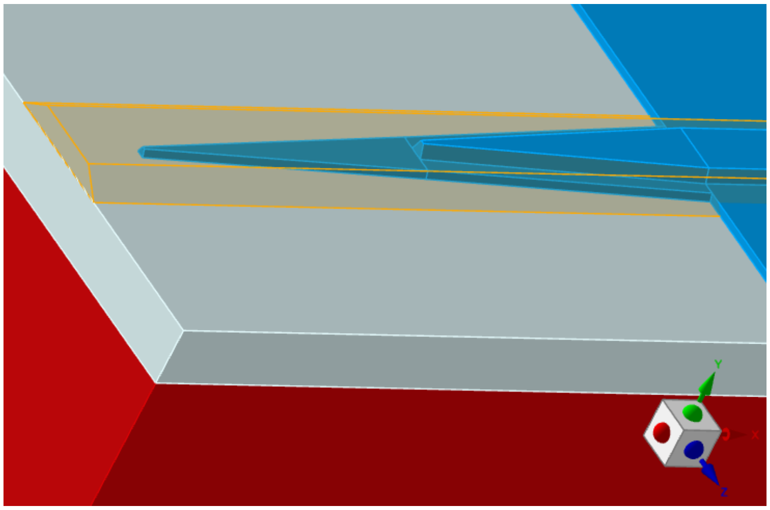

Figure 3.11: The simulation schematic of double layer inverse taper.

The blue structures in the schematic represents the taper structures and waveguide made of LN. Starting from the right-hand side of the schematic, the right end of the top taper is directly connected to the ridge waveguide with etch depth of 450 nm and top width of 1.8 µm. The top width of the top taper is adiabatically narrowed from 1.8 µm to 150 nm at the end of the top taper while the top width of the first segment of the bottom taper with the same length of 150 µm changes adiabatically from 3 µm to 1.5 µm. The second segment of the bottom taper following the first segment further narrows the top width from 1.5 µm to 100 nm over 250 µm.

The entire taper structure is covered by another polymer waveguide as shown in the orange structure in the schematic, which is made of photoresist AZ4330, with the top width of 3 µm, height of 3.5 µm, and the base angle of 75 degrees, which is characterized and calculated from the SEM image. The bottom taper layer gets cut off at the edge of the chip where there is only polymer waveguide that has good mode matching with the optical beam from the input/output coupling system.

With such structure, simulated coupling efficiency of better than –0.9 dB over 100 nm can be achieved with the input gaussian beam with beam radius of 1.4 µm as shown in figure 3.12 (a).

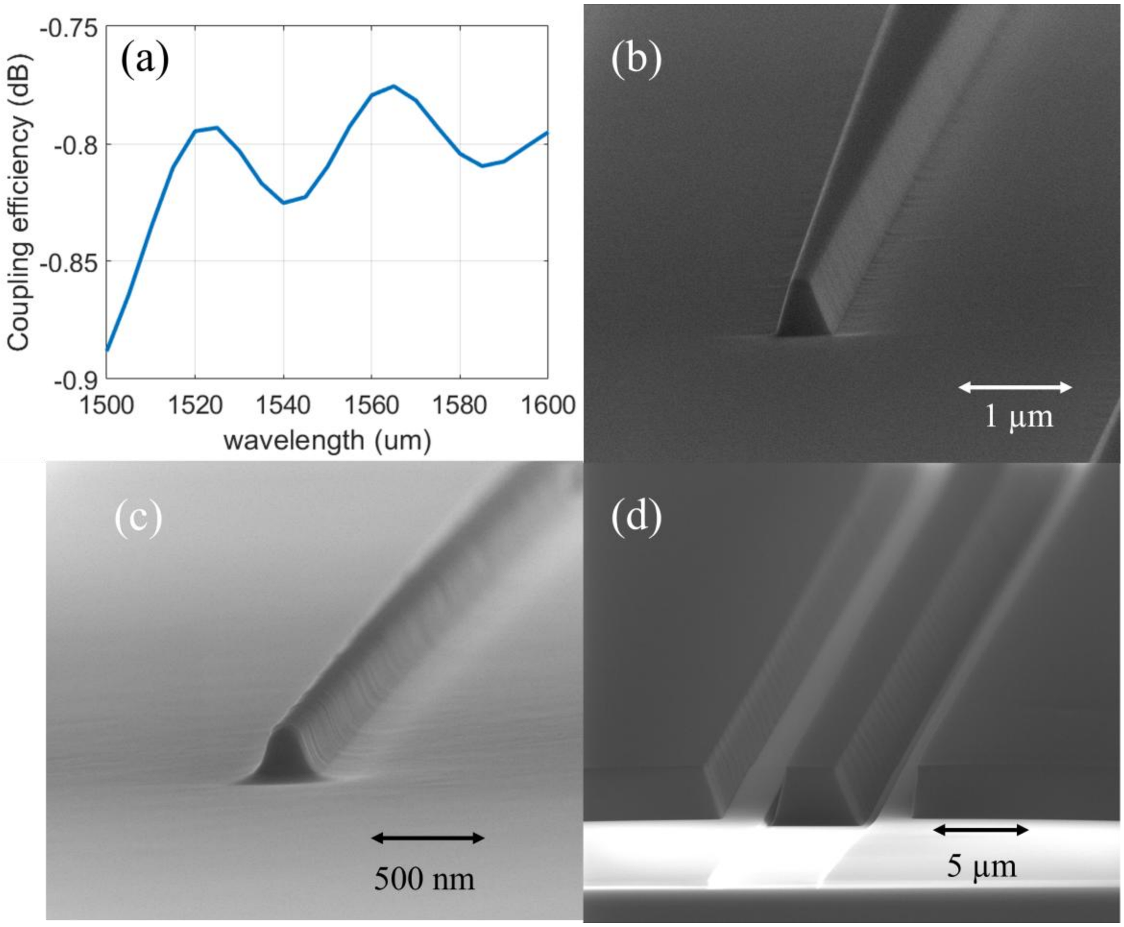

Figure 3.12: (a) Simulated coupling efficiency of double layer inverse taper with polymer waveguide AZ4330; (b) SEM image of the top taper region after the process of first layer; (c) SEM image of the bottom taper region after the process of second layer; (d) SEM image of the end of polymer waveguide region after dicing.

For the device fabrication, we first pattern the top taper layer and waveguide structures with the optimized fabrication process described in chapter 2 with the etch depth of 450 nm and the fabricated top taper region is shown in figure 3.12 (b). Then the E-beam resist mask of the second layer is patterned by an aligned EBL writing with the misalignment smaller than 100 nm with respect to the first layer with the top taper and waveguide structures protected and then the second etch is conducted with etch depth of 250 nm. Due to the narrow width of bottom taper tip, the sidewall roughness is not as good as the other structures as shown in figure 3.12 (c). However, the mode is majorly confined in the polymer waveguide region at the bottom tip region, so the sidewall roughness of the bottom tip should not introduce too much additional scattering loss. Afterwards, an aligned photolithography process is conducted with a maskless aligner (MLA) to define the polymer waveguide structure.

We cannot release the facet by dicing the polymer waveguide and polishing it like what we would do to the LN waveguide as the polymer waveguide will be destroyed by the polishing process. Therefore, the strategy we adopt is to extend the trench region where LN is completely etched and the photoresist is exposed and subsequently removed during the development process, and then we perform dicing as close to the end of the polymer waveguide as possible in the trench region so that the input beam will not be truncated by the SiO_2 layer underneath as shown in figure 3.12 (d).

The fabricated device consists of two identical double layer inverse taper structures at both ends of the chip connected by a 2 mm-long waveguide with the top width of 1.8 μm whose propagation loss is neglected. The best overall coupling efficiency with the free space setup is -7 dB, which corresponds to -3.5 dB per facet. We attribute nearly 3 dB discrepancy to imperfection of the coupling system and the separation between the actual edge of the chip and the end of the polymer waveguide due to the limited accuracy of our dicing machine as shown in figure 3.12 (d).

3.5.2 Design with SiO_2 cladding

To address the additional coupling loss induced by the imperfection of polymer waveguide and beam truncation, we replace the polymer waveguide with a 2 μm-thick SiO_2 cladding to reduce the mode confinement. To make the mode that is loosely confined in the bottom tip region by SiO_2 substrate and cladding, the top width of the bottom taper tip is increased from 100 nm to 300 nm while the other dimensions of the double layer inverse taper structure remain the same.

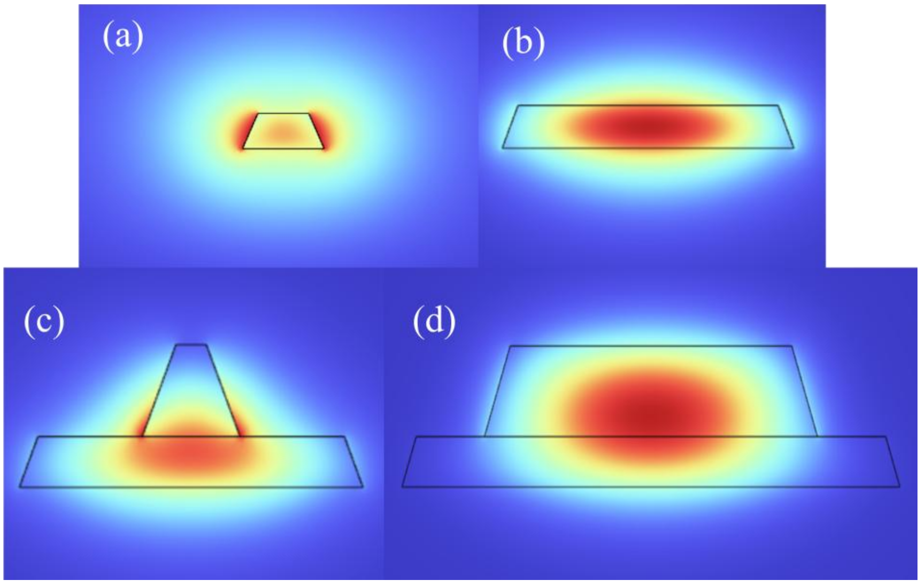

Figure 3.13: Normalized electric field distribution at (a) The bottom taper tip; (b) The end of the second segment of bottom taper; (c) The onset of the top taper; (d) The ridge waveguide.

Figure 3.13 (a), (b), (c), and (d) depict the normalized electric field distribution at the tip of the bottom taper, the end of the second segment of the bottom taper, the onset of the top taper, and the ridge waveguide region, respectively.

As shown in figure 3.13 (a), the mode confinement becomes stronger as the dimension of the bottom taper tip gets larger. Therefore, the optimal optical beam radius from the coupling system is much smaller than the polymer waveguide case. An overall coupling loss of better than -0.75 dB over 100 nm can be achieved with an incoming Gaussian beam with radius 0.7 μm as shown in figure 3.14 (a).

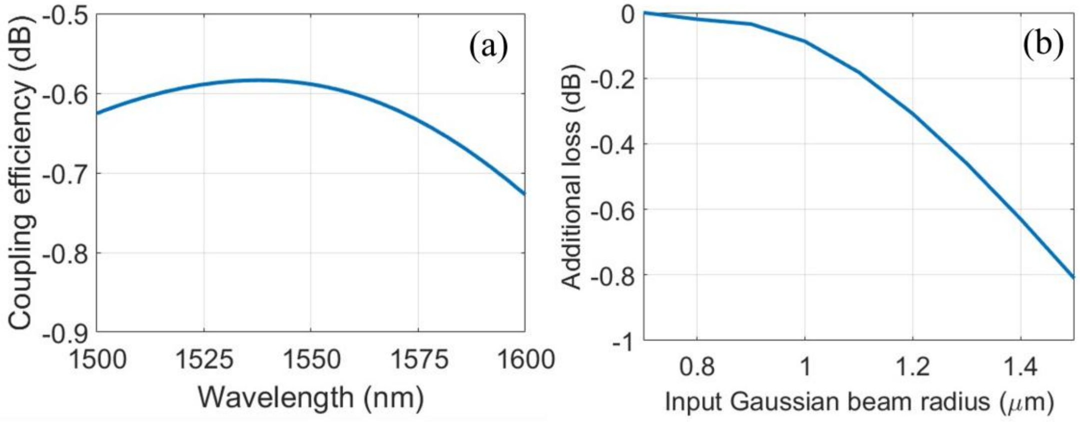

Figure 3.14: (a) The overall coupling efficiency between an input Gaussian beam with radius 0.7 μm and the ridge waveguide with top width 1.8 μm; (b) The addition coupling loss when the radius of the input gaussian beam varies from 0.7 μm to 1.4 μm.

Although Gaussian beam with radius 0.7 μm is typically hard to achieve, only additional -0.8 dB will be introduced when the radius of the input Gaussian beam is doubled as illustrated in figure 3.14 (b).

The fabrication process of this design is almost the same as the design with polymer waveguide except for the last few steps. Instead of patterning AZ4330 layer with a maskless aligner (MLA), a layer of 2 μm-thick SiO_2 is deposited by a Plasma

Enhanced Chemical Vapor Deposition tool (PEVCD). The sidewall roughness of the bottom taper is reduced compared to the one with polymer waveguide as shown in the SEM image in figure 3.15 (a).

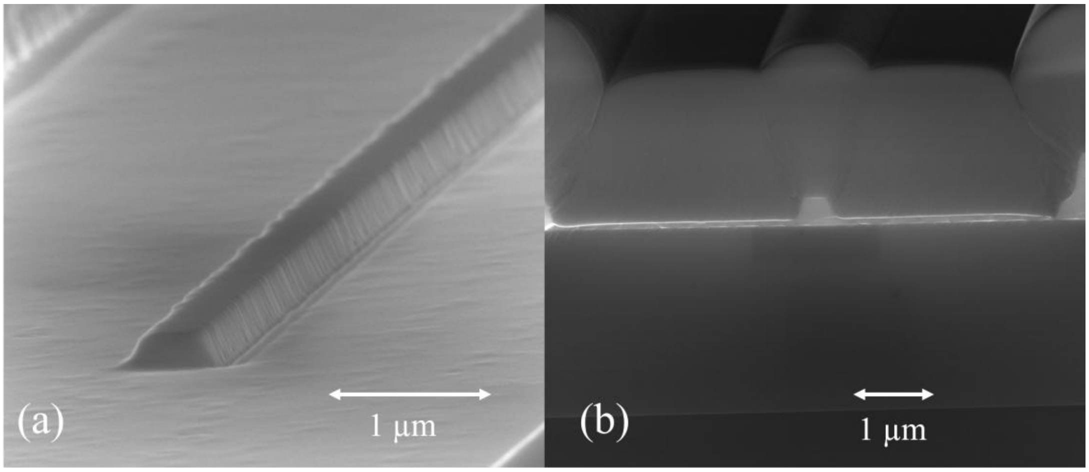

Figure 3.15: (a) SEM image of the bottom taper tip region with 300 nm top width at the tip; (b) SEM image of the facet after cleaving.

For this design, we use diamond scribing tool to create a scratch directly on the 1 mm-long bottom taper tip extension structure with the exact same top width as the bottom taper tip and cleave the chip to release the facet instead of using dicing and polishing techniques because the both processes are too aggressive and they will delaminate the top SiO_2 cladding region rendering poor mode matching at the edge.

The best performance we achieve is -5.5 dB coupling efficiency in total, which corresponds to -2.75 dB coupling efficiency per facet with the input Gaussian beam radius of 1 μm. Although the coverage of top SiO_2 remains in perfect condition as shown in SEM image in figure 3.15 (b), the facet is not smooth enough to get the coupling efficiency we are expecting. Besides, a thin layer of unetched LN underneath the bottom taper structure will also change the mode confinement compared to the design introducing additional loss from the mode mismatch.

Compared to the design with polymer waveguide, the design with SiO_2 cladding requires smaller beam to achieve better mode matching, which would impose challenges on the optical system, but it eases up the bottom taper tip width making the structure easier to fabricate with better quality. Besides, unlike the polymer waveguide design whose performance also depends on the dimension and the quality of the polymer waveguide, the expected coupling efficiency can be obtained without the strict requirement on the thickness of SiO_2 cladding.

3.6 Summary

In this chapter, we first introduce dicing and polishing method to release the facet of the waveguide on chip for end-facet coupling that can achieve limited coupling efficiency. Then we introduce the grating coupler with linear apodization and chirping that can provide higher coupling efficiency, based on which we propose and fabricate a grating coupler optimized by inverse design method on 700 nm-thick Z-cut LNOI platform featuring -3.8 dB peak coupling efficiency with 1-dB and 3-dB bandwidths of 85.8 nm and over 120 nm, respectively. After the discussion of the limitation of mode matching with single layer inverse taper of LN, we propose two designs with double layer inverse taper of LN on the same platform that can potentially provide sub -1 dB coupling efficiency over 100 nm bandwidth, and -2.75 dB coupling efficiency is experimentally demonstrated with the fabricated device with around -2 dB difference compared to the simulated results due to the fabrication imperfection.

Chapter IV

Dispersion engineered micro-ring resonators

Micro-ring resonators providing cavity enhancement are particularly important for efficient nonlinear interactions. Mirco-ring resonators on LNOI platform open up new lane for frequency combs/solitons generation utilizing its both second- and third-order nonlinearities [26,40,41,25,44,45]. Thanks to the continuous effort on improving the fabrication techniques of LN, which used to be very challenging, the quality of micro-ring resonators on LNOI platform has been improved dramatically drawing a lot of attention to have this platform ready for all kinds of applications such as dual-comb spectroscopy, atomic clock, frequency synthesizer, optical ranging, biomedical imaging, optical communications and quantum computation [25,46,47,48,50,51,52,53,54,55,56,57,58].

Apart from the requirement on the quality factor of the micro-ring resonators, being able to engineer the dispersion of the resonators to achieve group velocity matching or certain amount of group velocity mismatch (GVM), specific group velocity dispersion (GVD), and even higher-order dispersion is essential to the bandwidth of the nonlinear process such as second-order harmonic generation, optical parametric oscillations, optical parametric amplification and the formation of Kerr dissipative solitons and quadratic solitons.

In this chapter, we will first introduce pulley coupler, a 4-segment circular bending structure wrapping around the microresonator, can provide much stronger coupling ratio to the microresonator with the flexibility of shaping the wavelength dependency over a large bandwidth compared to the conventional single-point bus waveguide coupler. Then, we will discuss dispersion engineering and how important it is to nonlinear optical applications. Furthermore, we will introduce a MZI calibration system that helps tackle the non-uniformity of tunable laser sweeping to measure the dispersion of the microresonators more accurately. Finally, we will introduce the demonstration of the fabricated high-quality micro-ring resonator with loaded quality factor 2.2 million using the optimized fabrication method discussed in chapter 2 on 700 nm-thick LNOI platform paving the way for enhanced nonlinear optical interactions in micro cavities.

4.1 Single-point bus waveguide coupler

The quality of the micro-ring resonator can be quantified as the intrinsic quality factor Q_i defined by equation 4.1:

$$Q_i = n_{eff} \frac{2\pi}{2\lambda_{res}\alpha} \tag{4.1}$$

where n_{eff}, λ_{res}, and α stand for effective index of the optical mode of the micro-ring resonator, the center resonant frequency and the total loss including propagation, scattering loss, and absorption per unit length, respectively.

To characterize the intrinsic quality factor of the micro-ring resonator, we usually place a bus waveguide tangential to the micro-ring resonator called single-point coupler to have power exchange through evanescent wave. With the light coupled into the waveguide from one end, there will be dips at the resonant frequencies in the spectrum we measure at the other end of the bus waveguide, and we can calculate the loaded quality factor Q_L of the resonances by equation 4.2:

$$Q_L = \frac{\lambda_{res}}{\Delta\lambda} \tag{4.2}$$

where $\Delta\lambda$ is the full width half maximum (FWHM) of the resonance with a Lorentzian fit from the measurement.

The coupling ratio between the bus waveguide and the micro-ring resonator R can be converted into coupling quality factor Q_c given by equation 4.3:

$$Q_C = n_{eff}\frac{2\pi L}{\lambda_{res}R} \tag{4.3}$$

where L stands for total cavity length. We can link Q_i, Q_C, and Q_L through equation 4.4 and 4.5 [59,60]:

$$\frac{1}{Q_L} = \frac{1}{Q_i} + \frac{1}{Q_c} \tag{4.4}$$

$$T_{res} = \frac{\alpha^2 - 2\alpha\sqrt{R} + R}{1 - \alpha\sqrt{R} + R\alpha^2} \tag{4.5}$$

where T_{res} the transmission at the resonances, which can be acquired from the transmitted spectrum from the output end of the bus waveguide.

Typically, we want the micro-ring resonator to operate at critically coupled regime ($Q_i = Q_c$) where the transmission T_{res} reaches 0 or at over-coupled regime ($Q_i > Q_c$) for higher intracavity power depending on the application scenarios. The separation between the bus waveguide and the micro-ring resonator needs to be adjusted to provide different coupling ratios for specific applications.

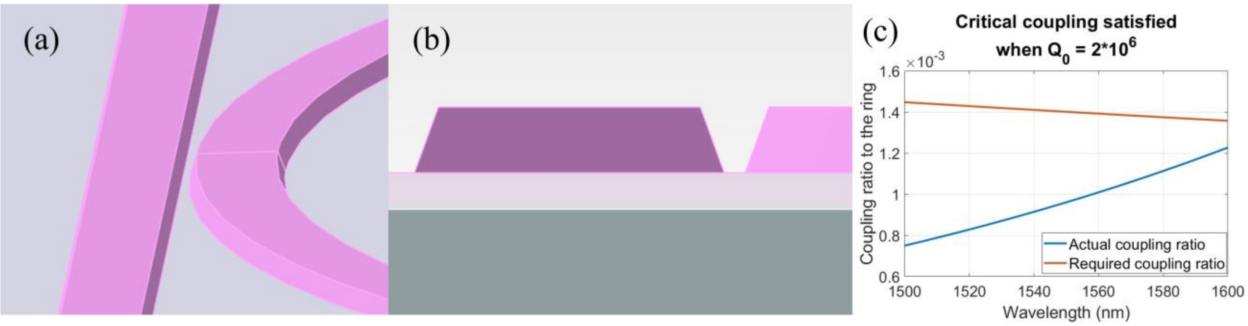

Figure 4.1: (a) 3D schematic of the coupling region between the single-point coupler and the micro-ring resonator; (b) Cross-section of the coupling region; (c) The simulated coupling ratio provided by the bus waveguide verses the required coupling ratio for the micro-ring resonator to operate at critically coupled regime when the intrinsic quality factor of the micro-ring resonator is estimated to be 2 million.

We use 3D FDTD in Lumerical (Ansys) to simulate the coupling ratio between two structures, and the simulation schematic is shown in figure 4.1 (a).

Due to the re-deposition, both bus waveguide and the micro-ring resonator will have an inevitable base angle, which will impose the limit of how close we can put two structures together as shown in the cross section in figure 4.1 (b) to obtain decent coupling ratio for the micro-ring resonator operating in the regime of interest.

Figure 4.1 (b) depicts the simulated coupling ratio between a single-point coupler and micro-ring resonator with similar top widths to achieve better effective index matching between two structures to enhance the coupling strength and the minimal gap at the bottom to be only 200 nm. However, the micro-ring resonator can hardly operate at the critically coupled regime as the coupling ratio is lower than the required value when the intrinsic quality factor of the micro-ring resonator is estimated to be two million, which can be hard to fabricate with high fidelity.

Once the actual quality factor of the fabricated micro-ring resonator is lower than the expectation, the curve for required coupling ratio will further shift upwards meaning that the micro-ring resonator will operate at under coupled regime ($Q_i < Q_c$) even more, which is usually undesirable.

4.2 Pulley-type coupler

The results from the previous section clearly show that single-point coupler cannot provide sufficient coupling ratio despite good effective index matching due to the limitation of inevitable base angle on both structures from re-deposition. To further enhance the coupling ratio between the two structures, we introduce pulley-type coupler. Instead of having a straight bus waveguide providing limited interaction length, we put 4 segments of circular curve wrapping around the micro-ring resonator as shown in the simulation schematic in figure 4.2 (a).

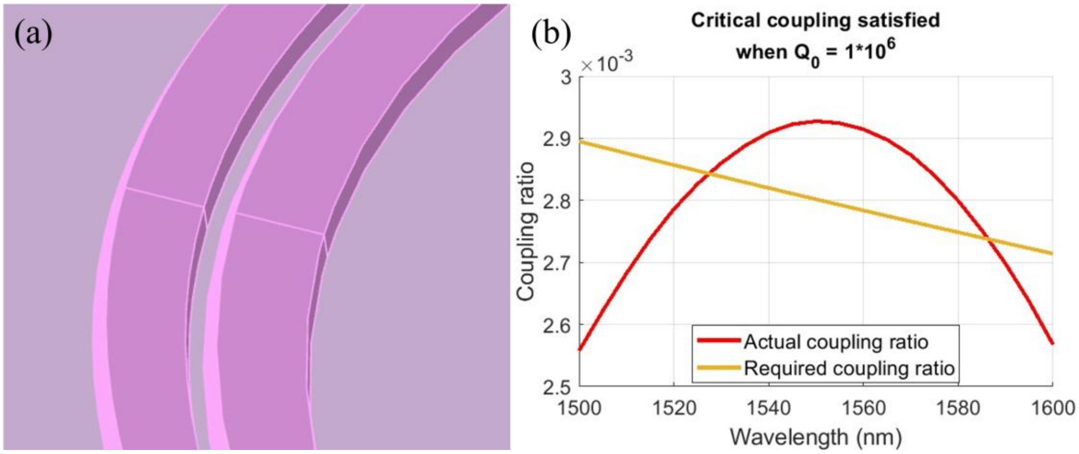

Figure 4.2: (a) 3D schematic of the coupling region between the pulley-type coupler and the micro-ring resonator; (b) comparison between actual coupling ratio provided by the pulley-type coupler and the required coupling ratio when the intrinsic quality factor is estimated to be one million.

The coupling ratio between the pulley-type coupler and the exact same micro-ring resonator as the previous section is shown in figure 4.2 (b). The design with pulley-type coupler can provide sufficient coupling ratio at the wavelength close to the center wavelength at 1550 nm to let micro-ring resonator operate at over-coupled regime when the intrinsic quality factor is estimated to be one million with critical coupled operation at two wavelengths requiring twice of the coupling ratio than the case in figure 4.1 with the minimal gap between the top edge of the pulley-type coupler and the micro-ring resonator being 600 nm.

Similar to the single-point bus waveguide coupler, the coupling ratio between the pulley-type coupler and the micro-ring resonator can be tuned by changing the gap between two structures and the width of the pulley-type coupler as shown in figure 4.3 (a) and 4.3 (b). The red curve and yellow curves in each sub plot represent the design mentioned above and the required coupling ratio to achieve critical coupling when the intrinsic quality factor is estimated to be one million, respectively.

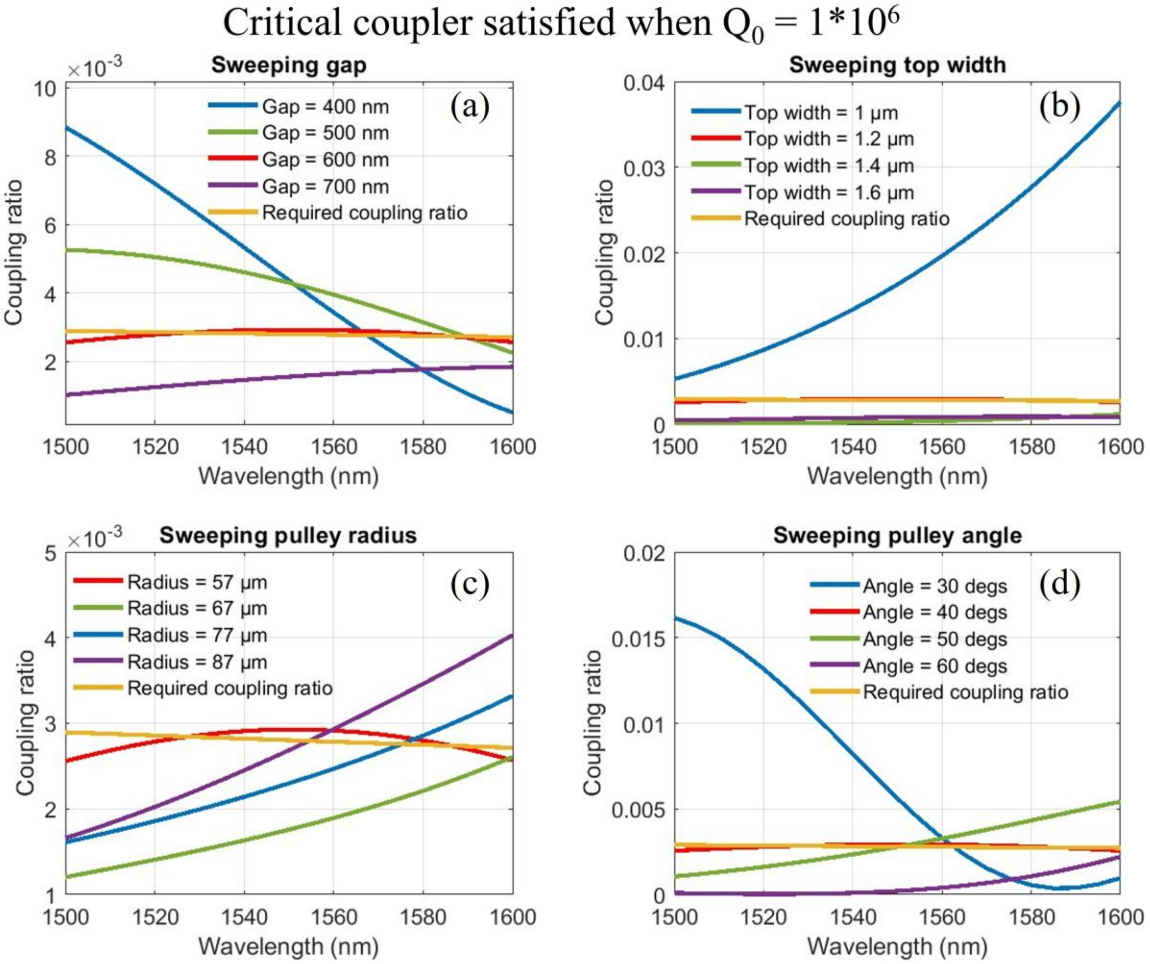

Figure 4.3: Coupling ratio with different parameter sweep: (a) sweeping the minimal gap between the pulley-type coupler and the micro-ring resonator; (b) sweeping the top width of the pulley-type coupler; (c) sweeping the bending radius of the pulley-type coupler; (d) sweeping the wrapping angle of the pulley-type coupler.

On the top of those two parameters, the coupling ratio can also be changed by adjusting the radius and the wrapping angle of the pulley-type coupler as shown in figure 4.3 (c) and 4.3 (d), which are not the degrees of freedom that single-point coupler has.

There are also other ways to manipulate the structure to realize different requirement on the coupling ratio to the micro-ring resonator as well as suppressing the coupling ratio for high-order spatial modes to achieve single mode operation [61,62,63].

4.3 Dispersion engineering

For the study of the generation and the evolution of frequency combs and solitons with numerical methods, it is not realistic to analytically express wavevector k (propagation constant β) as a function of frequency, and what we usually do is to use Taylor expansion to expand it as defined in equation 4.5:

$$k(\omega) = k_0 + \frac{\partial k}{\partial \omega}(\omega - \omega_0) + \frac{1}{2!}\frac{\partial^2 k}{\partial \omega^2}(\omega - \omega_0)^2 + \frac{1}{3!}\frac{\partial^3 k}{\partial \omega^3}(\omega - \omega_0)^3 + \cdots \qquad (4.5)$$

where k_0 is the wavevector of the center frequency, $\frac{\partial k}{\partial \omega}$ is the first-order derivative of wavevector called inverse group velocity (GV), $\frac{\partial^2 k}{\partial \omega^2}$ is the second-order derivative of the wavevector or the derivative of GV called group velocity dispersion, and the cubic term $\frac{\partial^3 k}{\partial \omega^3}$ is the third-order derivative of wavevector called third-order dispersion (TOD). Although there are dispersions with higher orders, the contribution of those higher order terms on the dispersion can be negligible for most of the cases for simplicity.

Minimizing group velocity mismatch (GVM) is particularly important when the interaction between frequency components spans a large spectral range, as this significantly impacts the phase matching bandwidth. A broad phase matching bandwidth is essential for nonlinear processes like second-harmonic generation and quadratic soliton generation [26]. However, as illustrated by the red curve in Figure 4.4, lithium niobate exhibits a very high GVM between the fundamental wave (FF) at telecom band and its second harmonic (SH) counterpart.

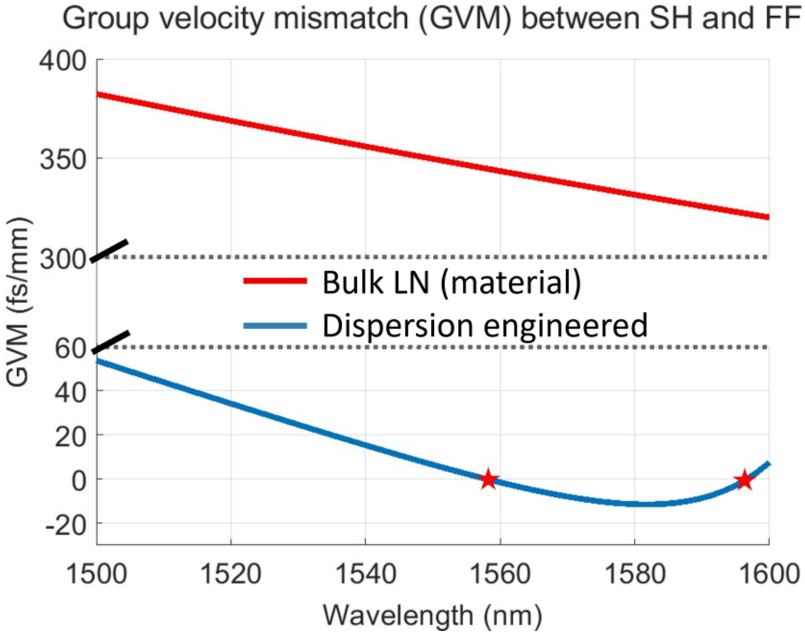

Figure 4.4: Group velocity mismatch of LN verses group velocity mismatch of a dispersion engineered waveguide on LNOI platform between the fundamental waves from 1500 nm to 1600 nm and their second harmonic counterparts.

By changing the waveguide width, total thickness of the thin film, etched depth, and the bending radius of the micro-ring resonator, the GVM can be reduced to 0 at the frequency of interest as shown in the blue curve in figure 4.3.

Typically, the formation of dissipative Kerr solitons relies on the balance between the nonlinearity and the dispersion, which means that GVD needs to be negative. The material GVD LN possesses is positive as shown in the red curve in figure 4.5 while the GVD can be changed to a negative value in the micro-ring resonator as shown in the blue curve in figure 4.5 providing suitable environment for dissipative Kerr solitons generation.

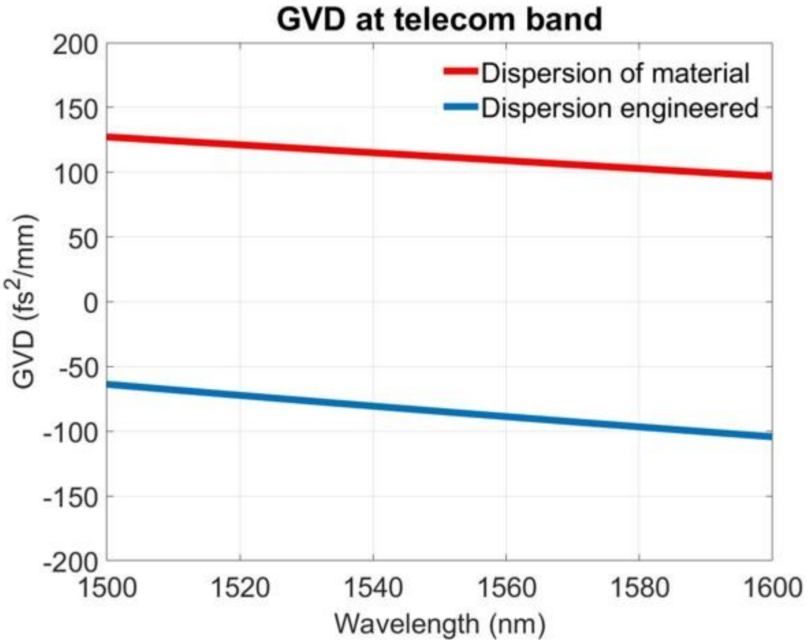

Figure 4.5: Group velocity dispersion of LN verses group velocity dispersion of a dispersion engineered micro-ring resonator on LNOI platform between the fundamental waves from 1500 nm to 1600 nm and their second harmonic counterparts.

TOD and higher-order dispersion can be usually negligible. However, the effect of TOD can be evident enough to perturb or even destroy the formation of solitons when GVD is extremely small. In some specific cases, TOD can help with the formation of solitons, or it can be utilized to modify the stability, dynamics, and bifurcation structure of solitons [64].

4.4 Characterization of micro-ring resonators

The micro-ring resonators with bending radius of 55 μm, etch depth of 450 nm, and the top width of 1.8 μm with the pulley-type coupler are fabricated on a 700 nm-thick Z-cut LNOI platform with the optimized fabrication process elaborated in chapter 2. The SEM images of the overview of the micro-ring resonator, the sideview of the coupling region between the pulley-type coupler and the micro-ring resonator, and only micro-ring resonator regions are shown in figure 4.6 (a), (b) and (c), respectively.

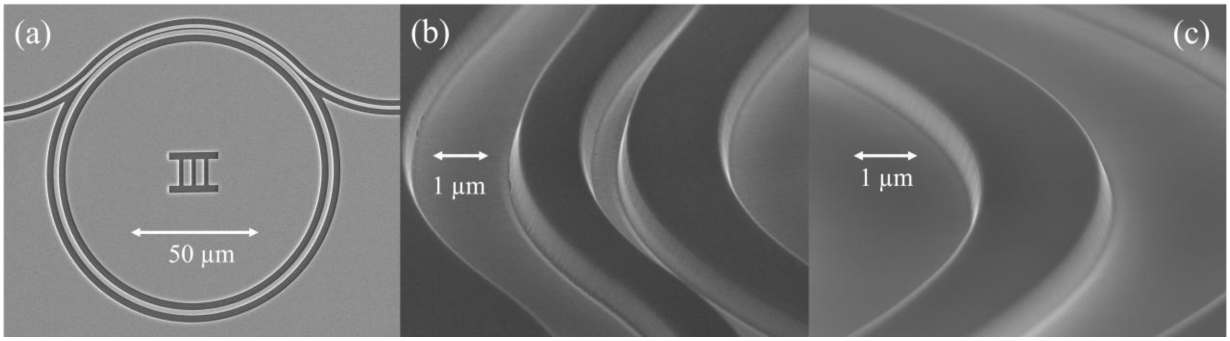

Figure 4.6: The SEM images of (a) The overview of the micro-ring resonator; (b) The sideview of the coupling region between the pulley-type coupler and the micro-ring resonator; (c) The sideview of only micro-ring resonator.

For the quality factor measurement and the GVD calculation of the fabricated micro-ring resonator, we use lensed fibers on both side of the edge couplers to coupled light into the pulley-type waveguide from Santec TSL-710 that is scanned continuously from 1500 nm to 1600 nm at the scan rate of 100 nm/s and the output lensed fiber is connected to a InGaAs photodetector whose output is subsequently collected by a digitizer (CSE1222 Razor Express, Gage). To get the GVD with better accuracy, we introduce a Mach-Zehnder Interferometer (MZI) to calibrate the inconsistent scan rate of our Santec [65]. The schematic of the measurement setup is illustrated in figure 4.7.

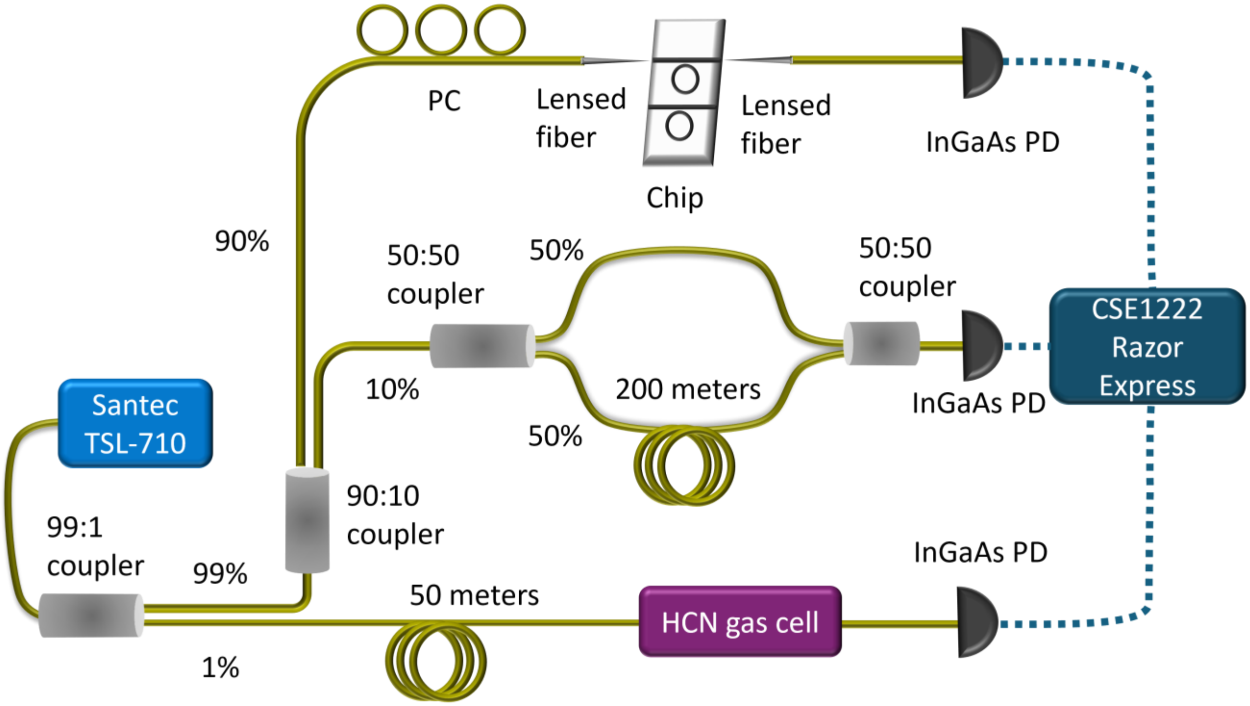

Figure 4.7: Experimental setup for the quality factor and the dispersion measurement of micro-ring resonators.

As shown in the schematic, 1/99 coupler at 1550 nm following Santec split power into two paths. 1 percent of power is sent to a 50-meter-long SMF-28 delay line, which is connected to a HCN gas cell providing absolute frequency reference at absorption peaks from 1527 nm to 1564 nm. The transmission is collected by a photodetector (PD) whose output voltage signal is collected by the digitizer. The other 99% of power is then split into two paths by a 90:10 coupler at 1550 nm, in which 90% of the power is coupled into the chip under test by a lensed fiber with a polarization controller in front of the lensed fiber to control the polarization of the input and the transmitted power is then collected by another lensed fiber and the electrical signal converted by a PD is collected simultaneously by the digitizer. Another 10% of the power from the 90:10 coupler is sent to the MZI system as shown in the middle of the schematic.

The delay line at the bottom arm of the MZI consists of 135-meter-long SMF-28 and 65-meter-long dispersion compensation fiber so that the accumulated group delay dispersion is the same as the top arm of the MZI. Two optical signals interfere with each at the PD connected to the 50:50 coupler at the right-hand side of the schematic creating a sinusoidal signal whose periodicity varies with the scan rate of Santec, which is sent to the digitizer as the external clock signal. With this configuration, the transmitted data from the gas cell as well as the output of the chip can be synchronistically collected by the digitizer every 5 MHz, which is typically good enough to resolve the resonances with linewidth wider than 100 MHz.

The transmitted data of a fabricated micro-ring resonator and a zoom-in resonance with the Lorentzian fit are shown in figure 4.8 (a) and (b), respectively.

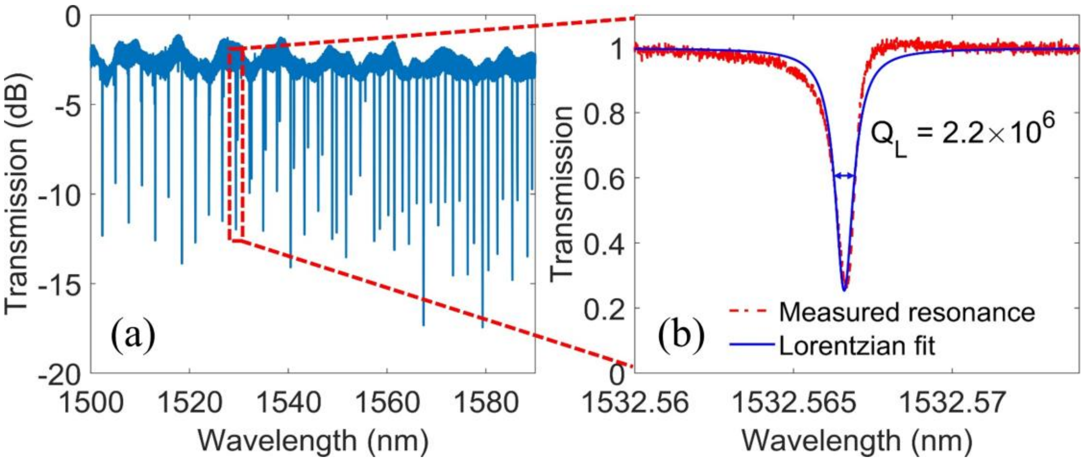

Figure 4.8: (a) Transmitted data of a fabricated micro-ring resonator; (b) the profile of a resonance at 1543.567 nm with Lorentzian fit.

Thanks to the optimized fabrication process, one of the resonances as shown in figure 4.8 (b) has the loaded quality factor of 2.2 million, which corresponds to the finesse of over 3000 and the loaded quality factors of all the resonances between 1500 nm and 1600 nm are above 1 million with deep resonance depth as illustrated in figure 4.9 (a).

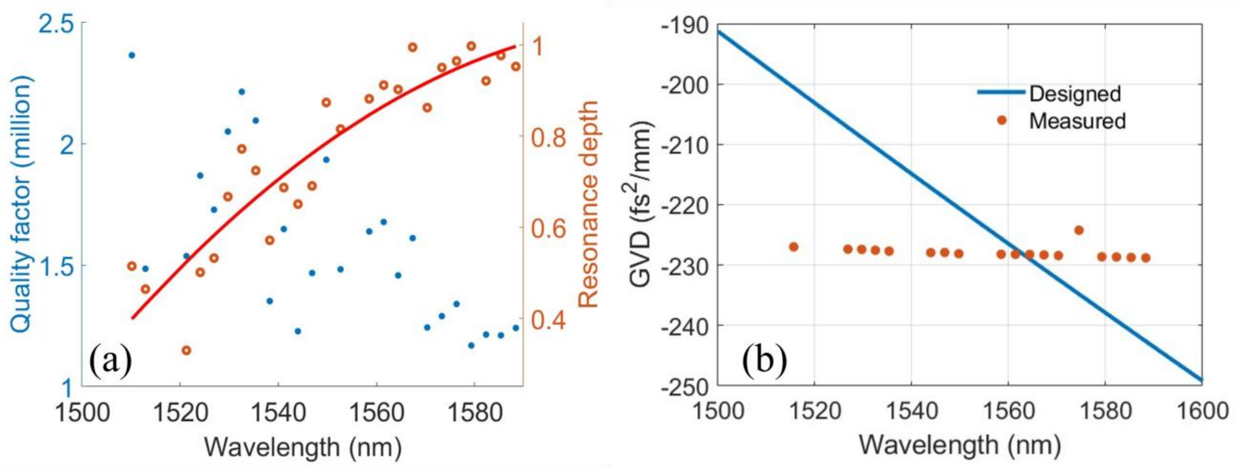

Figure 4.9: (a) Transmitted data of a fabricated micro-ring resonator; (b) The profile of a resonance at 1543.567 nm with Lorentzian fit.

The effective indices n_{eff} of the micro-ring resonator can be calculated in 2D asymmetric eigenmode solver in COMSOL with swept frequency, and the GVD can be numerically calculated from the second-order derivative of the propagation constants β given by $n_{eff}\frac{2\pi}{\lambda}$ as shown in the blue curve in figure 4.8 (b), and after the linear fitting on the free spectral range (FSR) of the resonances from the same spatial mode family with the calibrated wavelength axis by the MZI and the transmitted data from the HCN gas cell, the GVD is calculated as shown in discrete red dots in figure 4.9 (b), which matches with the simulated GVD. However, due to the dispersion parameter being a constant, which is calculated from the linear fitting of the limited data points of FSR, how GVD changes at different resonances namely TOD cannot be calculated accurately. Therefore, the GVD at different resonances only differs by FSR.

4.5 Summary

In this chapter, we first talk about the limitation of the conventional single-point coupler. Then we introduce the design of pulley-type coupler and its potential to provide much higher coupling ratio over a large bandwidth compared to the conventional single-point coupler. Furthermore, we discuss the importance of dispersion engineering to different nonlinear applications and dispersion engineering can be easily achieved on LNOI devices. Last but not least, we introduce an optical characterization system that can measure the loaded quality factor, resonance depth, and the dispersion of the micro-ring resonator in an accurate fashion with an out-of-loop MZI calibration system, and we fabricate and characterize a micro-ring resonator on 700 nm-thick Z-cut LNOI platform with loaded quality factor of 2.2 million corresponding to the cavity finesse of over 3000.

Chapter V

Second harmonic generation on Z-cut LNOI waveguide

Among LN's other exceptionally excellent properties, breaking inverse symmetry making it possess high second-order nonlinearity ($\chi^{(2)}$) is one of the reasons that LN is more attractive than other material that does not have $\chi^{(2)}$ such as silicon nitride. Second harmonic generation (SHG) as one of the most fundamental nonlinear processes enabled by high $\chi^{(2)}$ is not just the very basis of parametrically driven dissipative Kerr solitons and quadratic solitons generation [26,41], but also important to the applications such as nonlinear optical microscopy [68], optical clock [69], and quantum information processing [70].

Apart from miniaturization of the on-chip devices compared to the bulk material [71], SHG process can be more power efficient due to strong mode confinement and small mode sizes of both FF and SH components inside the waveguide. With the flexibility of dispersion engineering, the group velocity mismatch between the pump and SHG can be minimized without going with type-1 or type-2 phase matching schematics that would significantly reduce $\chi^{(2)}$ to achieve broadband SHG [72].

In this chapter, we will first analytically derive the conversion efficiency of SHG in a straight waveguide to better understand how different parameters affect the conversion efficiency. We will then discuss the significance of phase matching in

SHG and how to achieve quasi phase matching via periodic poling on Z-cut LNOI platform. Furthermore, we will talk about the design for SHG and the importance of using ellipsometer for refractive index measurement for the more accurate estimation of phase mismatch. Finally, we will discuss the demonstration of SHG on Z-cut LNOI with high normalized conversion efficiency of 5200%/W/cm^2 and its thermal tunability.

5.1 Analytical solution of SHG conversion efficiency

To design waveguides for SHG with high conversion efficiency, it is important to come up with a simplified mathematical model that represents the relationship between the conversion efficiency and parameters of the waveguide. Thanks to the optimized fabrication process, the propagation loss is almost negligible for waveguides shorter than 1 cm.

Inside the waveguide on Z-cut LNOI, light travels along the propagation direction, which is the x axis of LN crystal, in the form of spatial eigenmodes and the electric field $\widetilde{E_n}$ of the spatial eigenmodes can be expressed in equation 5.1 as [73,74]:

$$\widetilde{E_n} = A_n(x)E_n(y,z)e^{i(\beta_n y-\omega_n t)} \tag{5.1}$$

Where $A(x)$ is field amplitude varying along the propagation direction, $E_n(y,z)$ is the electric field distribution of the spatial eigenmode along the transverse plane, β_n and ω_n is the propagation constant and the angular frequency of the spatial eigenmode, respectively. After applying the slowly varying amplitude approximation, the wave equation can be simplified as equation 5.2 [75]:

$$\frac{d\widetilde{E_n}}{dx} = \frac{i\omega_n}{2\epsilon_{0n_{eff,n}}c} P_n^{NL} \tag{5.2}$$

Where ϵ_0 and c is the permittivity and speed of light in vacuum, n_{eff}, n is the effective index of the spatial eigenmode, P^{NL} is the nonlinear polarization term whose expression is given in equation 5.3 and 5.4 for FF and SH component, respectively:

$$P_{FF}^{NL} = 2\epsilon_0\chi^{(2)}\widetilde{E_{FF}}^{*}\widetilde{E_{SH}} \tag{5.3}$$

$$P_{\mathrm{SH}}^{NL} = \epsilon_0\chi^{(2)}\widetilde{E_{\mathrm{FF}}}\widetilde{E_{\mathrm{FF}}} \tag{5.4}$$

Where $\chi^{(2)}$ is the second-order nonlinearity. After plugging equations 5.1, 5.3, and 5.4 into equation 5.2, we can express the first-order derivative of the field amplitude for FF and SH as equation 5.5 and 5.6, respectively:

$$\frac{dA_{FF}}{dx}E_{FF}(y,z) = E_{FF}^{*}(y,z)E_{SH}(y,z)\frac{i\omega_{FF}\chi^{(2)}}{n_{eff,FF}c}A_{FF}^{*}A_{SH}e^{-i\Delta\beta x} \tag{5.5}$$

$$\frac{dA_{SH}}{dx}E_{SH}(y,z) = E_{FF}(y,z)E_{FF}(y,z)\frac{i\omega_{SH}\chi^{(2)}}{2n_{eff,SH}c}A_{FF}A_{FF}e^{i\Delta\beta x} \tag{5.6}$$

Where $\Delta\beta = \Delta n_{eff}\frac{2\omega_1}{c}$ is the propagation constant mismatch between FF and SH components. After organizing both equations and integrating both equations along the transverse YZ plane, we can get:

$$\frac{dA_{FF}}{dx} = \frac{i\omega_{FF}\chi^{(2)}}{n_{eff,FF}c}A_1^{*}A_2e^{-i\Delta\beta x}\frac{\int E_{FF}^{*}(y,z)^2E_{SH}(y,z)dydz}{\int|E_{FF}(y,z)|^2dydz} \tag{5.7}$$

$$\frac{dA_{SH}}{dx} = \frac{i\omega_{SH}\chi^{(2)}}{2n_{eff,SH}c}A_1A_1e^{i\Delta\beta x}\frac{\int E_{FF}(y,z)^2E_{SH}^{*}(y,z)dydz}{\int|E_{SH}(y,z)|^2dydz} \tag{5.8}$$

By using the electric field a_n that is associated with optical power P_n in the waveguide expressed in equation 5.9:

$$P_n = |a_n|^2 = |A_n|^2 2n_{eff,n}\epsilon_0 c \int |E_n(y,z)|^2 dydz \tag{5.9}$$

Equations 5.7 and 5.8 can be rewritten as:

$$\frac{da_{FF}}{dx} = ig^* a_{FF}^* a_{SH} e^{-i\Delta\beta x} \tag{5.10}$$

$$\frac{da_{SH}}{dx} = iga_{FF}^2 e^{i\Delta\beta x} \tag{5.11}$$

Where g represents the nonlinear coupling coefficient, which can be expressed as equation 5.12 after replacing $\chi^{(2)}$ with $2d_{eff}$:

$$g = \frac{\sqrt{2}\omega_{FF} d_{eff}}{n_{eff,FF}\sqrt{n_{eff,SH}\epsilon_0 c^3}} \frac{\int E_{FF}(y,z)^2 E_{SH}^*(y,z) dydz}{\int |E_{FF}|^2 dydz \sqrt{\int |E_{SH}|^2 dydz}} \tag{5.12}$$

Considering a waveguide with total length L: while no seed for SH component is present and FF is not depleted, $a_{SH}(0) = 0$ and $|a_{FF}(0)| = |a_{FF}(x)| \gg |a_{SH}(x)|$ stand, and equation 5.11 can be solved as:

$$a_{SH}(L) = iga_{FF}^2(0) \int_0^L e^{i\Delta\beta x}\, dx = iga_{FF}^2(0) L sinc(\frac{\Delta\beta L}{2}) e^{\frac{i\Delta\beta L}{2}} \tag{5.13}$$

And the SH pump at the end of the waveguide can be expressed as equation 5.14:

$$P_{SH}(L) = |a_{SH}(L)|^2 = |g|^2 P_{FF}^2(0) L^2 sinc^2(\frac{\Delta\beta L}{2}) \tag{5.14}$$

Thus, the absolute conversion efficiency of SHG process η_{abs} can be expressed in equation 5.15 as:

$$\eta_{abs} = \frac{P_{SH}(L)}{P_{FF}(0)} = P_{FF}(0)L^2|g|^2 sinc^2(\frac{\Delta\beta L}{2}) \tag{5.15}$$

Where $|g|^2$ can be calculated from equation 5.12 and it can be expressed after some organization in equation 5.16 as:

$$|g|^2 = \frac{2\omega_{FF}{}^2 d_{eff}{}^2}{n_{eff,FF}{}^2 n_{eff,SH}\epsilon_0 c^3} \frac{\int E_{FF}(y,z)^2 E_{SH}^*(y,z)dydz \int E_{FF}{}^*(y,z)^2 E_{SH}(y,z)dydz}{(\int |E_{FF}|^2 dydz)^2 \int |E_{SH}|^2 dydz} \tag{5.16}$$

The effective mode area A_{eff} for SHG process is defined as $A_{eff} = \sqrt[3]{A_{FF}{}^2 A_{SH}}$ where A_{FF} and A_{SH} represents the effective mode area for FF and SH, respectively, which can be expressed in equation 5.17 as [76]:

$$A_n = \frac{(\int |E_n(y,z)|^2 dydz)^3}{|\int |E_n(y,z)|^2 E_n(y,z)|^2} \tag{5.17}$$

In the nominator, the integral includes the entire cross-section of the waveguide while the integral includes only $\chi^{(2)}$ media in the denominator. included After applying the expression of A_{eff} in equation 5.16, $|g|^2$ can be further simplified as equation 5.18:

$$|g|^2 = \frac{2\omega_{FF}{}^2 d_{eff}{}^2}{n_{eff,FF}{}^2 n_{eff,SH}\epsilon_0 c^3 A_{eff}} |\zeta|^2 \tag{5.18}$$

Where ζ spatial mode overlap coefficient represents the modal overlap between FF and SH eigenmodes, which can be expressed in equation 5.19 as:

$$\zeta = \frac{\int E_{FF}(y,z)^2 E_{SH}^*(y,z)dydz}{|\int |E_{FF}(y,z)|^2 E_{FF}(y,z)|^{\frac{2}{3}} |\int |E_{SH}(y,z)|^2 E_{SH}(y,z)|^{\frac{1}{3}}} \tag{5.19}$$

It is important to notice in equation 5.15 the absolute conversion efficiency is linearly proportional to the on-chip power of FF, i.e., the pump power $P_{FF}(0)$ and the quadrature of the total length of the waveguide L. To decouple these two "external" factors from the conversion efficiency, the normalized conversion efficiency η_{norm}, obtained by normalizing η_{abs} with $P_{FF}(0)$ and L^2 is a better figure of merit representing the efficiency of SHG process, which can be expressed in equation 5.20 as:

$$\eta_{norm} = \frac{\eta_{abs}}{P_{FF}(0)L^2} = |g|^2 sinc^2\left(\frac{\Delta\beta L}{2}\right) = \frac{2{\omega_{FF}}^2{d_{eff}}^2}{{n_{eff,FF}}^2 n_{eff,SH}\epsilon_0 c^3 A_{eff}} sinc^2\left(\frac{\Delta\beta L}{2}\right)|\zeta|^2 \tag{5.20}$$

$\Delta\beta L$ representing the accumulated phase mismatch between FF and SH along the total length of the waveguide impacts the conversion efficiency of the SHG process.

5.2 Phase matching

As expressed in equation 5.20, the relationship between the normalized conversion efficiency and the accumulated phase mismatch is plotted in figure 5.1 with the normalized conversion efficiency further normalized when $\Delta\beta L$ equals zero i.e., phase matching condition is satisfied.

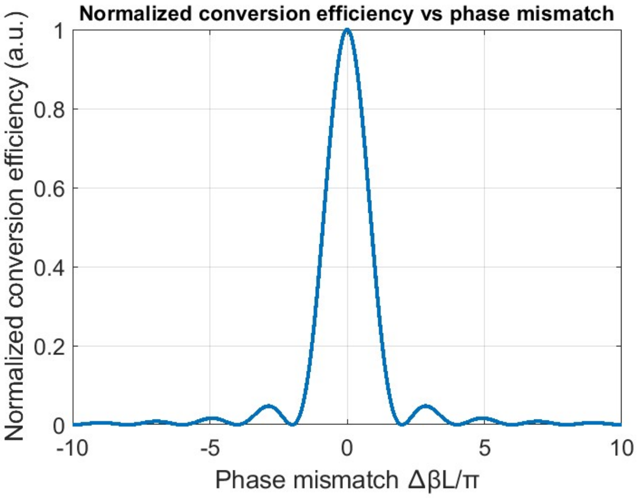

Figure 5.1: Normalized conversion efficiency of SHG process with the presence of phase mismatch.

As shown in the figure, the conversion efficiency drops to 5% of the value with phase matching when there is only 3π of accumulated phase mismatch between FF and SH components at the end of the waveguide.

5.2.1 Phase mismatch

Phase matching is the prerequisite to achieve high-efficiency SHG as shown in figure 5.1. However, due to the large spectral span between FF and SH components, the phase matching cannot be naturally satisfied due to the material dispersion as shown in figure 5.2.

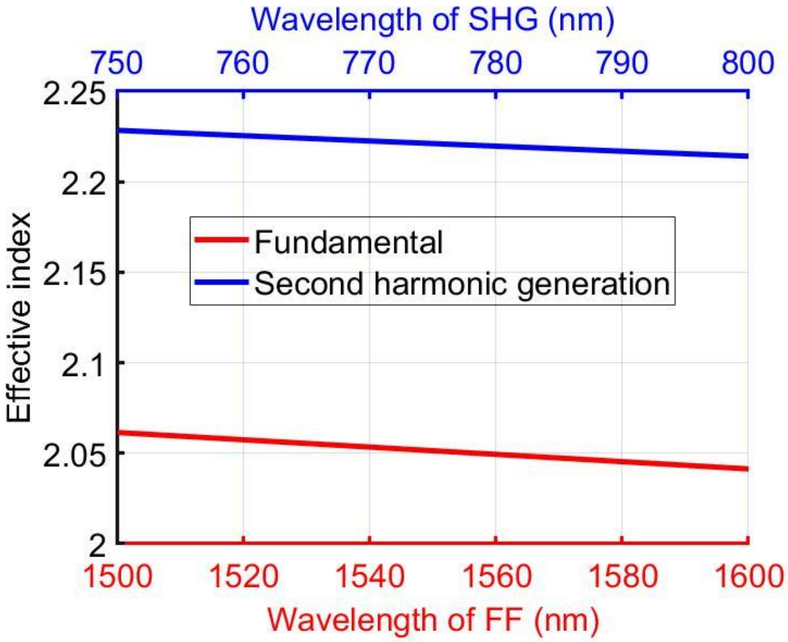

Figure 5.2: Effective indices comparison between FF component at 1550 nm and its SH counterpart at 775 nm.

5.2.2 Modal phase matching

Perfect phase matching can be achieved between the higher order spatial eigenmode of the SH component, which can be supported by waveguides with large dimensions, and the fundamental spatial eigenmode of FF component. An example is given in figure 5.3 (a) where the effective index of fundamental TE mode of the FF component coincides with the effective index of TE_{05} mode of the SH component.

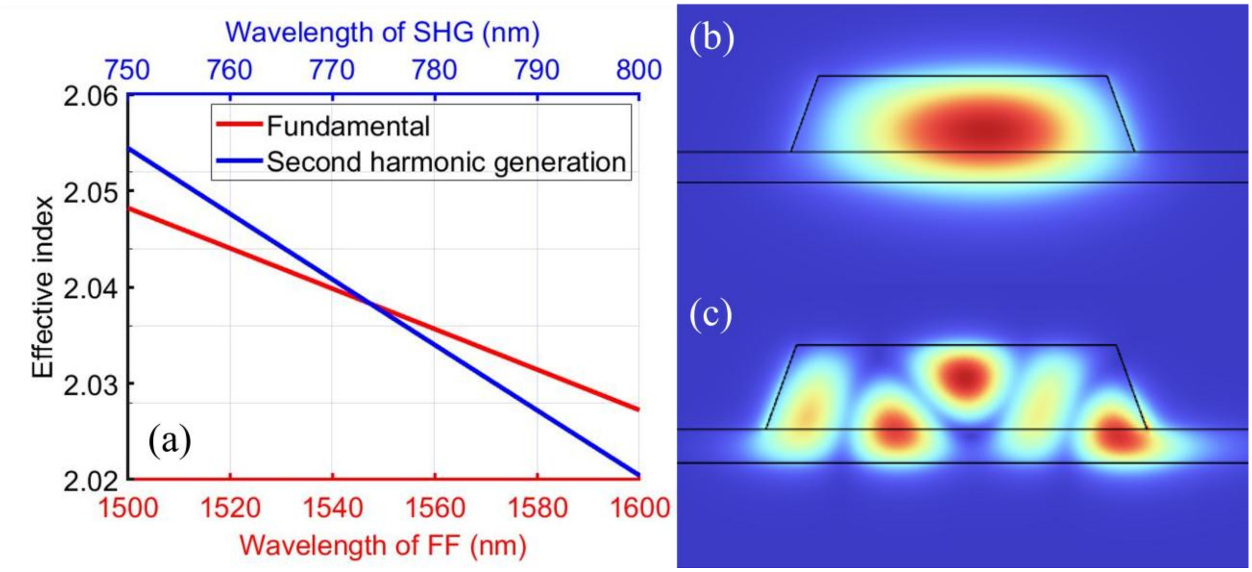

Figure 5.3: (a) Effective index of fundamental TE mode of FF component at 1550 nm and TE$_{05}$ of SH component at 775 nm; (b) Eigenmode profile of the fundamental TE mode of FF component at 1550 nm; (c) Eigenmode profile of TE$_{05}$ mode of SH component at 775 nm.

The eigenmode profiles of fundamental TE mode of FF component and TE$_{05}$ mode of the SH component are illustrated in figure 5.3 (b) and (c), respectively. Despite the absence of phase mismatch between FF and SH components, poor spatial modal overlapping $|\zeta|^2$ of below 0.1 as shown in the eigenmode profiles will totally erase the improvement on the conversion efficiency introduced by phase matching, making it not the ideal for SHG process [76].

5.2.3 Quasi phase matching and periodic poling

Instead of sacrificing the spatial overlapping between FF and SH components, fundamental TM modes for both components on Z-cut LNOI are chosen to maintain high ζ, meanwhile the highest effective second-order nonlinearity d_{33} can be used as both components are polarized along the crystal axis. A periodic grating is introduced by reversing the ferroelectric domain of LN periodically along the propagation direction of waveguides or micro-ring resonators with periodicity Λ, which compensates the propagation constant mismatch $\Delta\beta$ thus phase mismatch as defined in equation 5.21:

$$\Delta\beta = 2n_{eff,FF}\frac{2\pi}{\lambda_{FF}} - n_{eff,SH}\frac{2\pi}{\lambda_{SH}} = \frac{2\pi}{\Lambda} \tag{5.21}$$

The most effective way to realize this periodic domain inversion is through electric field periodic poling that a few cycles of pulsed signal with high voltage are applied to the electrodes on the top of Z-cut LNOI waveguides or micro-ring resonators as shown in the periodic poling schematic in figure 5.4. Pulsed voltage signal is generated by an arbitrary waveform generator (AWG), and the signal is sent to high voltage amplifier where the amplified pulsed voltage signal is directly applied on the electrodes through the high voltage probe, for the case of Z-cut LNOI, on the top of waveguides or micro-ring resonators while the Si substrate is placed on an aluminum plate, which is heated up by a hotplate to 200 °C to effectively reduce the high voltage requirement [19], is connected to the ground port of the high voltage amplifier. The chip is immersed in dielectric oil to prevent arcing during the poling process.

Due to the potential difference between the electrodes and the Si substrate, an electric field with the opposed direction of the coercive field of LN is built, and once the amplitude of this electric field exceeds the latter one, the ferroelectric domain will be inverted. During a single poling process, 10 pulses in total are applied through the high voltage probe with peak voltage of 800 V, duration of 1 ms, rise time of 1 ms, fall time of 5 ms and wait time of 7 ms.

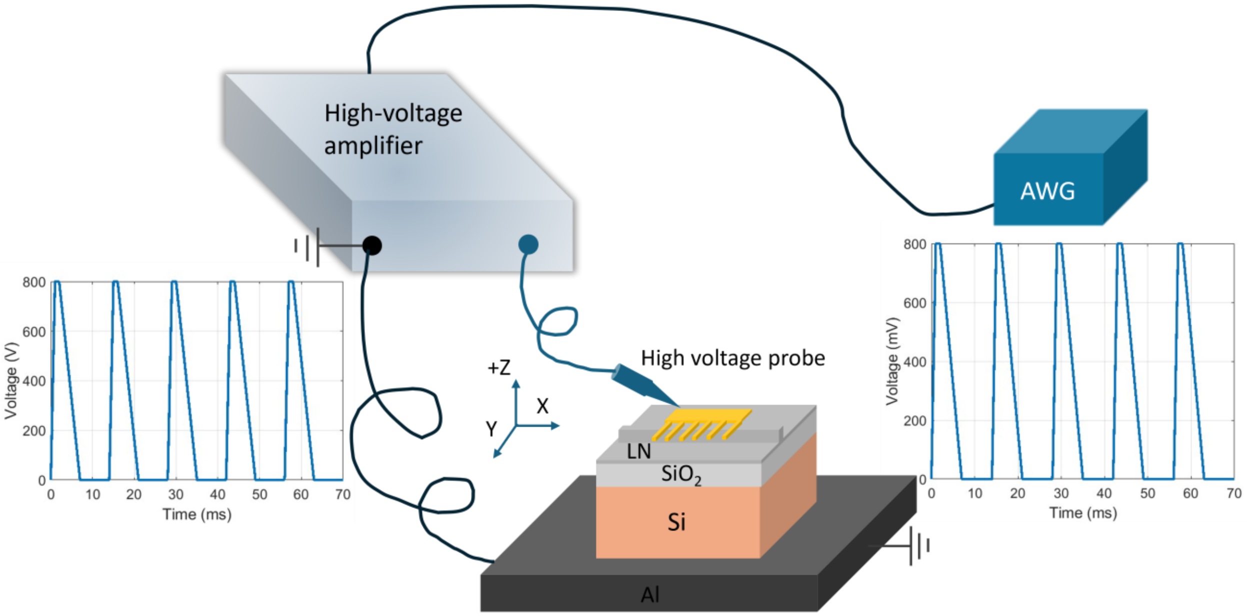

Figure 5.4: Schematic of electric field periodic poling setup.

5.3 Refractive indices measurement of LN and design for SHG

It has been recently studied that refractive indices of the LN thin film from vendors can be different from the ones reported in the literature [66,67] causing huge discrepancy between the poling period predicted by the simulation and the one that is actually needed to compensate the phase mismatch [77]. To come up with a more reliable design, we use a JA Woollam ellipsometer to measure the refractive indices of Z-cut LNOI chip we purchase from NanoLN, and the comparison of refractive indices of LN along ordinary and extraordinary axes are shown in figure 5.5 (a) and (b), respectively.

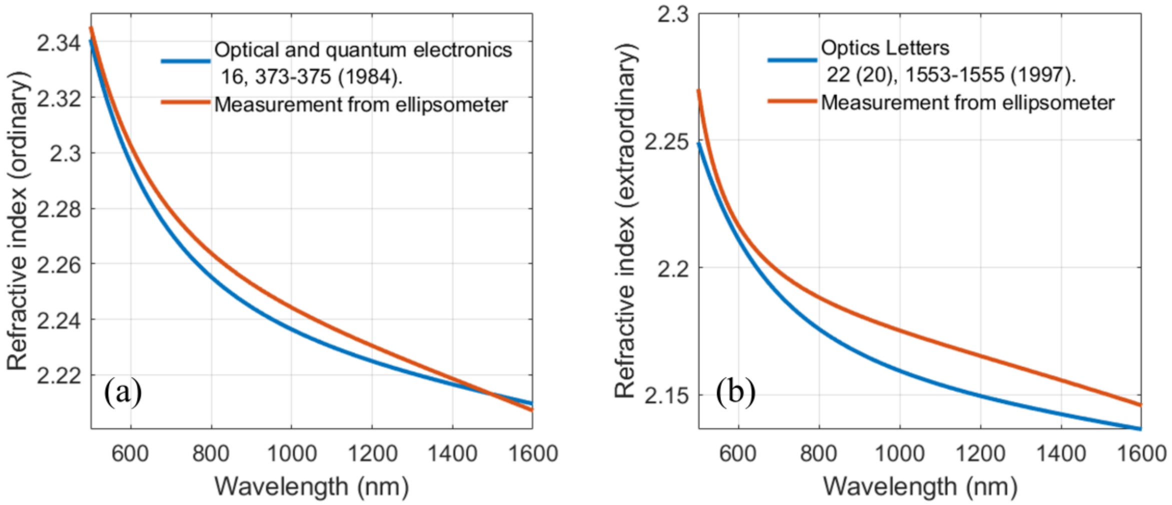

Figure 5.5: Refractive indices comparison along (a) ordinary axis; (b) extraordinary axis.

Although the difference is negligible at shorter wavelengths and the difference at around 1550 nm is only 1% at most, the discrepancy combined could change the required poling period to compensate phase mismatch a lot.

To ensure the propagation loss is negligible, we select the air cladded waveguide with the top width of 2 μm and the etch depth of 450 nm on a 700 nm-thick Z-cut LNOI platform. Both fundamental TM modes of FF and SH components are selected so that the largest effective second-order nonlinearity d_{33} can be used. The eigenmode profiles of fundamental TM modes of FF and SH components are shown in figure 5.6 (a) and (b), respectively. The mode confinement for both components is good, and the mode overlapping integral is close to 1 for this combination, which further guarantees high conversion efficiency of the SHG process.

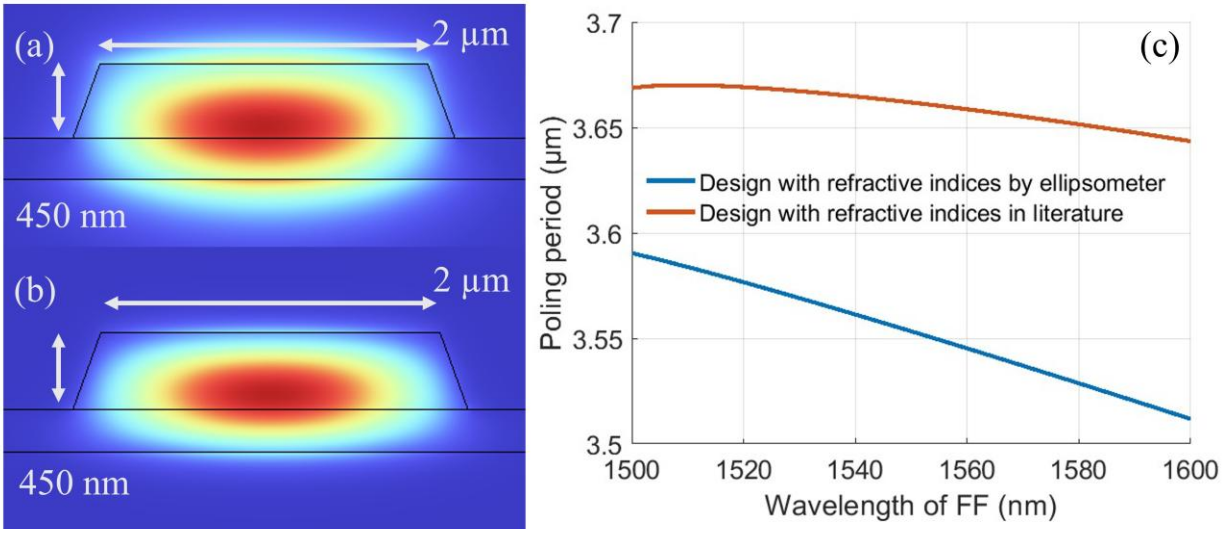

Figure 5.6: (a) Mode profile of fundamental TM mode of FF component; (b) Mode profile of fundamental TM mode of SH component; (c) Comparison of required poling period between the design with measured refractive indices and the ones provided in reference [66,67].

Figure 5.6 (c) depicts the comparison of the required poling period using different refractive indices for the same geometry of the waveguide mentioned above. The required poling period predicted by the refractive indices from [66,67] is 100 nm longer, which is 3% deviated from the value given by the measured refractive indices.

5.4 Fabrication of waveguides for SHG

The waveguides with designed geometry are fabricated using the optimized technique described in the fabrication chapter. Then the electrodes for periodic poling with the periodicity of the designed value 3.553 µm by the measured refractive indices and ± 70 nm from the designed value to compensate for the unpredictable fabrication error are defined by a lift-off process: First, a layer of ZEP 520A with the thickness of around 530 nm is spin coated on the top of Z-cut LNOI with the waveguides. Second, an aligned EBL process is conducted to pattern the mask where the area for the electrodes is exposed and removed by the following development process. Then 10 nm of chromium as an adhesion layer followed by 60 nm of gold is deposited by physical vapor evaporator with the deposition rate of 0.5 Å/s and 1 Å/s, respectively. Finally, the sample is dipped into remover PG at 80 °C for 2 hours to remove ZEP 520A and the electrodes on the top of it, and only the electrodes will be left over. The microscope images of the mask for electrodes after development and the electrodes after the lift-off process on one of the ends of the waveguides are shown in figure 5.7 (a) and (b), respectively.

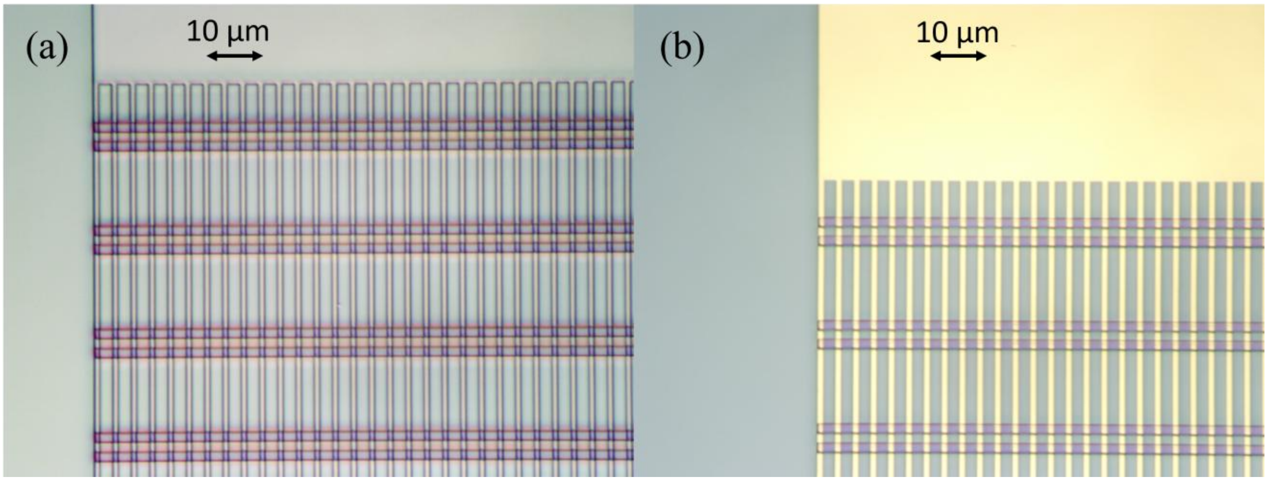

Figure 5.7: Microscope image of (a) EBL mask for electrodes after development; (b) electrodes after lift-off process.

The duty cycle, which is defined by the width of the electrode divided by the periodicity, is set to be 30% so that the width of the poled region is almost the same as the unpoled region within one period to reach the actual duty cycle of 50% after periodic poling, which results in a correction factor of $2/\pi$ applied to the effective second-order nonlinearity d_{33}.

After the poling process described in the previous section, the gold layer of the electrodes is removed by the mixture of 2 grams of potassium iodine (KI), 1 gram of iodine (I_2), and 50 milliliters of deionized water. And the chromium layer is subsequently removed by chromium etchant. The top view and the side view of the waveguide after the poling and electrodes removal process are shown in the SEM images in figure 5.8 (a) and (b), respectively. The poled region has lower secondary electron emission thus being darker than the rest of the region. Several periods are not successfully poled due to poor contact between LN waveguide and the electrodes. Although the duty cycle exceeds 50% for some periods, the poling uniformity is the best under this poling configuration.

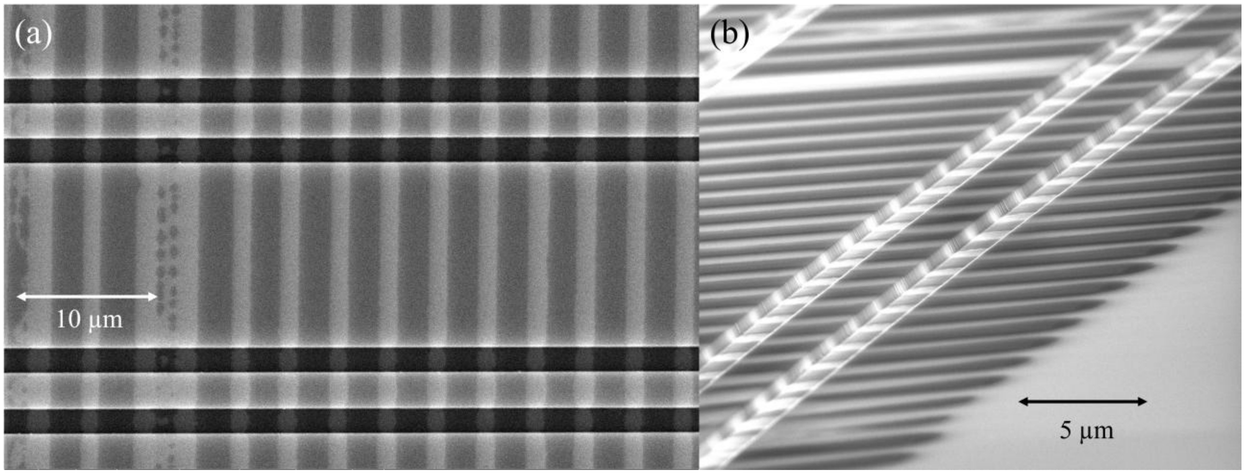

Figure 5.8: SEM image of (a) Top view of the waveguides after poling; (b) Side view of the waveguides after poling.

5.5 SHG characterization

The facets of those periodically poled waveguides are cleaved, and the chip is cleaned in the sonicator with remover PG bath before the SHG characterization. The optical characterization setup for SHG is illustrated in figure 5.9.

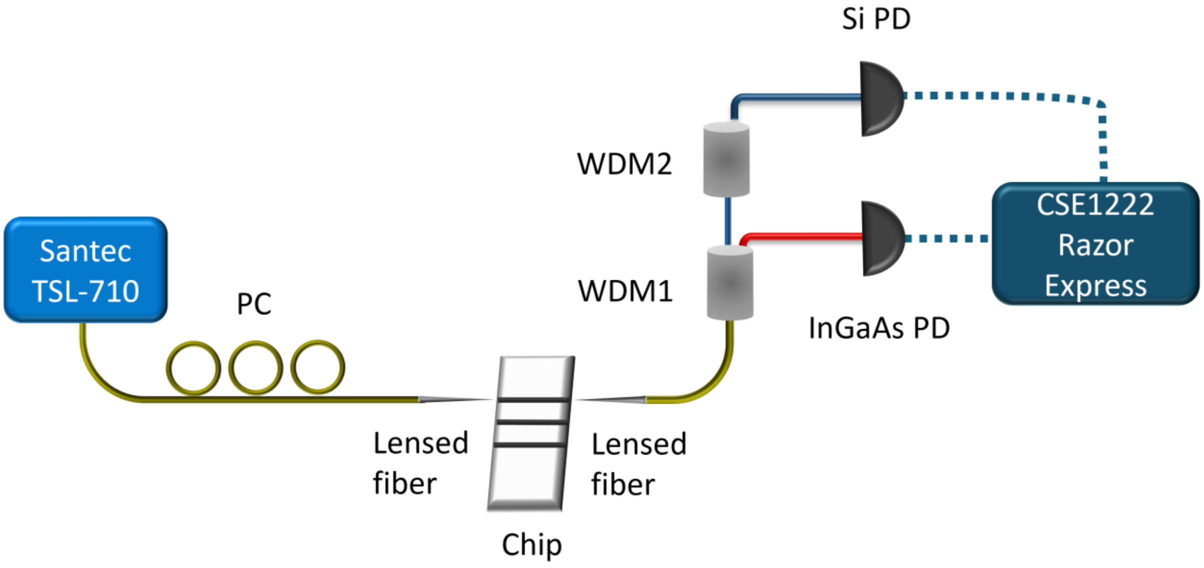

Figure 5.9: Optical characterization setup for SHG. PC: polarization controller; WDM: wavelength division multiplexer; PD: photodetector.

The tunable laser Santec TSL-710 is directly connected with a polarization controller to ensure the TM polarization for the input FF component, which is coupled to the waveguide on chip through a lensed fiber. The optical signal is then coupled out from the chip through a second lensed fiber, and the signal is sent to two cascaded wavelength division multiplexers (WDMs) to achieve higher isolation between the outcoupled FF and SH components. The generated SH component is outcoupled from the lensed fiber on the right-hand side of the schematic and goes completely into the blue port of the second WDM which is connected to a Si photodetector while outcoupled power of FF component is collected by an InGaAs photodetector from the red port of the first WDM. Both photodetectors are connected to the digitizer CSE1222 Razor express so that the data acquisition for both components are synchronized during the wavelength sweep of Santec.

The measured absolute conversion efficiency and the normalized conversion efficiency are plotted in figure 5.10 (a) and (b), respectively.

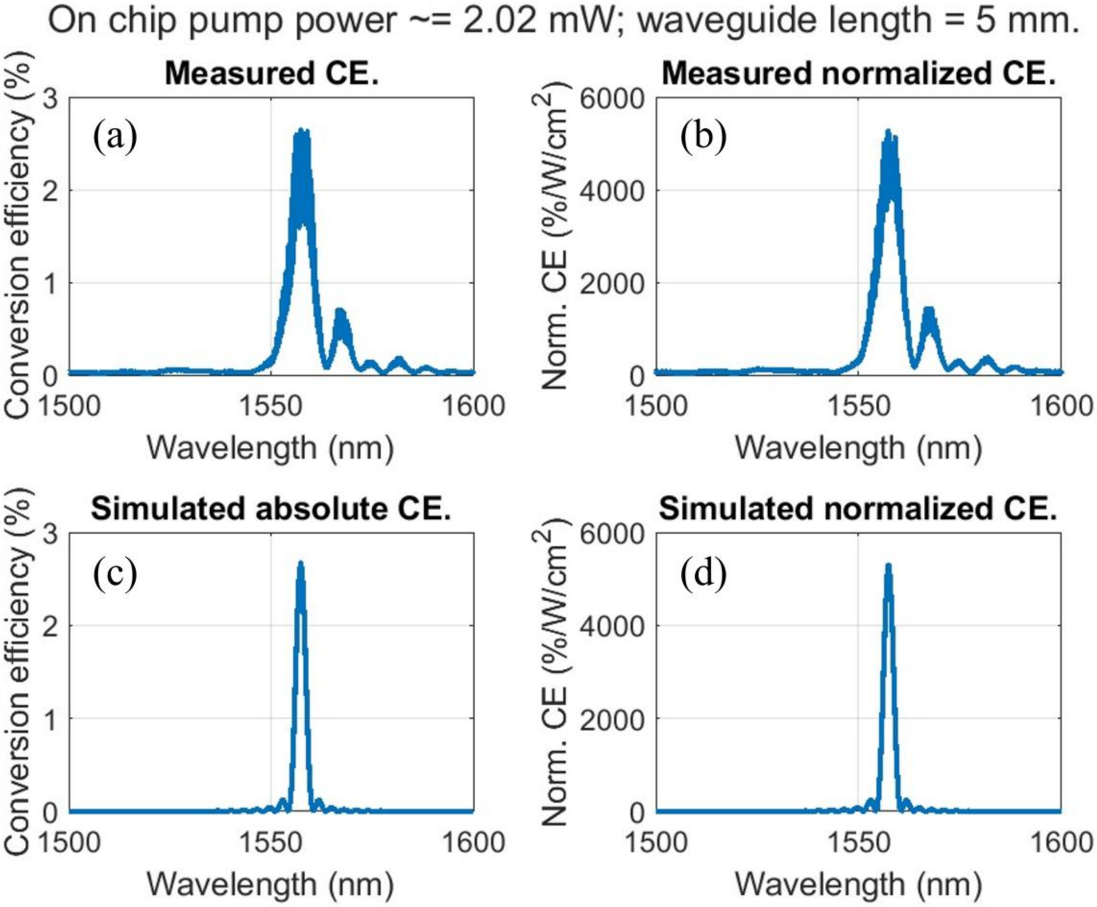

Figure 5.10: (a) Measured absolute conversion efficiency; (b) measured normalized conversion efficiency; (c) simulated absolute conversion efficiency; (d) simulated normalized conversion efficiency when the on-chip FF power is around 2.02 mW at center wavelength and the waveguide length is 5 mm.

Without the specific design on the GVM, phase matching bandwidth is limited to be around 10 nm, the absolute conversion efficiency is 2.63% when the on-chip power of the FF component is only 2.02 mW and the waveguide length is 5 mm that corresponds to a normalized conversion efficiency of 5200% /W/cm^2, which is one of the highest normalized conversion efficiencies ever experimentally demonstrated on LNOI platforms [78,79].

Although the peaks of both measured absolute conversion efficiency and normalized conversion efficiency match with the simulated results, the bandwidth and the asymmetry with respect to the peak of the conversion efficiency, which is most likely caused by combination of group velocity (GV), group velocity dispersion (GVD), and third-order dispersion (TOD). Besides, the experimental results are acquired from the waveguide with poling period 3.483 μm that is around 60 nm off from the design value at the center wavelength 1557.3 nm at 25 °C with the measured refractive indices. To further investigate this discrepancy, the normalized conversion efficiency and the required poling period at center wavelength 1557.3 nm are calculated with ± 5 nm of the total thickness of LN thin film with respect to the nominal thin film thickness, ± 50 nm of the top width of the waveguide with respect to the design top width 2 μm, and the ± 20 nm of the etch depth with respect to the design etch depth 450 nm are illustrated in figure 5.11 (a), (b), and (c) and (d), and (e), and (f), respectively.

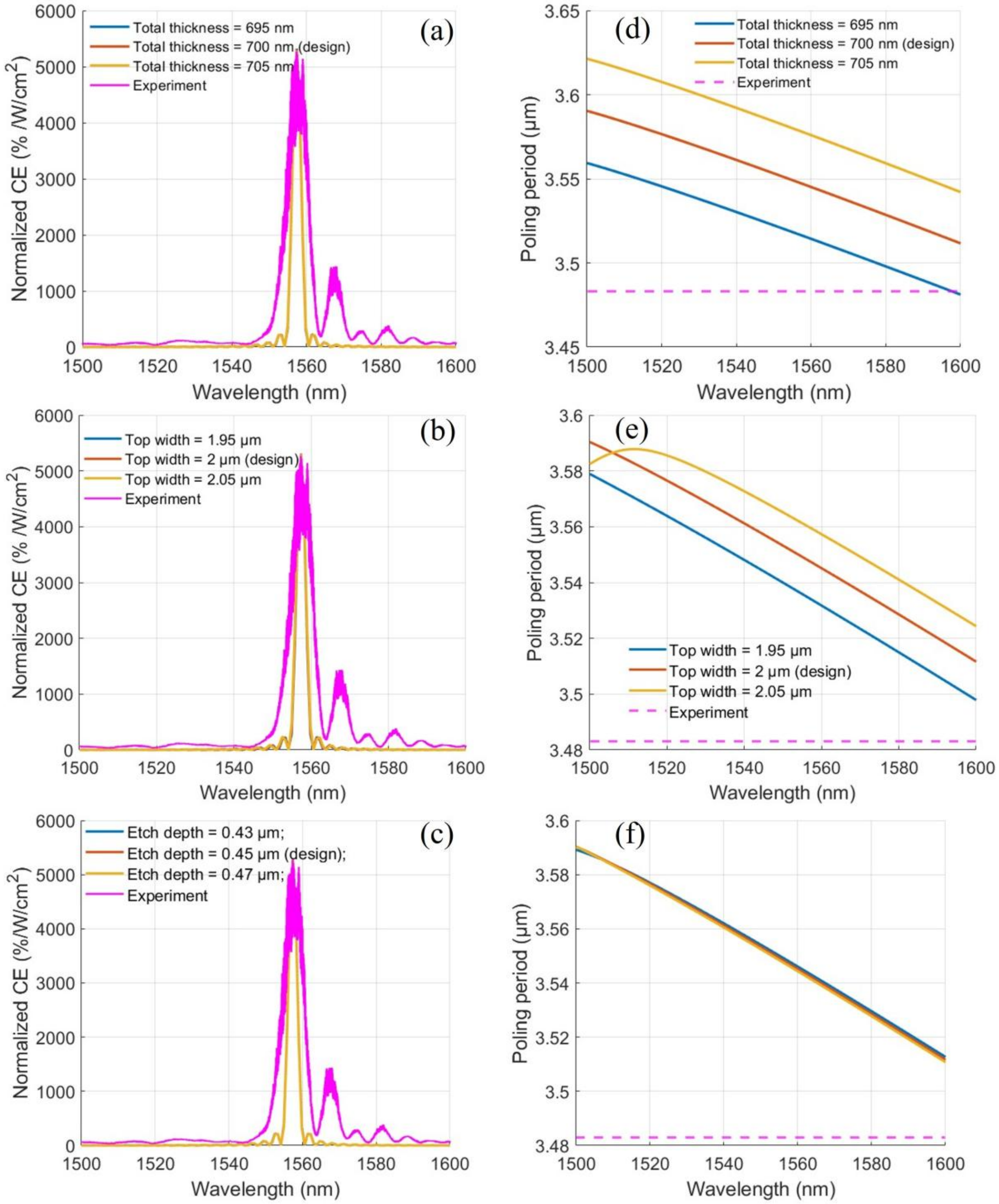

Figure 5.11: Normalized conversion efficiency variation with different dimensions (a) ± 5 nm on total thin film thickness; (b) ± 50 nm on waveguide top width; (c) ± 20 nm on etch depth; required poling period variation with different dimensions (d) ± 5 nm on total thin film thickness; (e) ± 50 nm on waveguide top width; (f) ± 20 nm on etch depth.

As shown in the figure, the poling period is extremely sensitive to the total thickness of LN thin film and the top width of the waveguide while it is not sensitive to the etch depth. 5 nm of total thickness difference, which is common in the purchased thin film would introduce 30 nm of poling period difference, and 2.5 % of top width difference would result in 10 nm of poling period difference. Along with the uncertainty of 0.7 % of the ellipsometer measurement, the 60 nm of poling period discrepancy can be explained.

It is important to note that there is a 180 nm difference on the poling period between the design value with the refractive indices from the literature and the actual poling period needed to achieve phase matching according to figure 5.6, which confirms that using the measured refractive indices from the ellipsometer helps better estimate the phase mismatch and get more accurate design for periodic poling.

However, those dimension variations do not change the phase matching bandwidth nor the symmetry of the normalized conversion efficiency plot. To get a better estimation of how the dispersion parameters are off from the actual case, correction terms of GV, GVD and TOD of -150 fs/mm, 25000 fs^2/mm, -1.5e6 fs^3/mm are introduced to the fundamental frequency (FF) component, and the required poling period is plotted in figure 5.12.

With those correction terms applied, the simulated normalized conversion efficiency plot starts to show the same asymmetry and similar bandwidth although the sub ripples on the longer wavelength side cannot be matched perfectly. According to the results, the dispersion parameters cannot be calculated accurately by the index data from the ellipsometer, and we attribute it to the sparse data points of 2 nm/point during the spectral scan of the ellipsometer measurements that high order information is lost while the zero-order information the phase indices are still accurate.

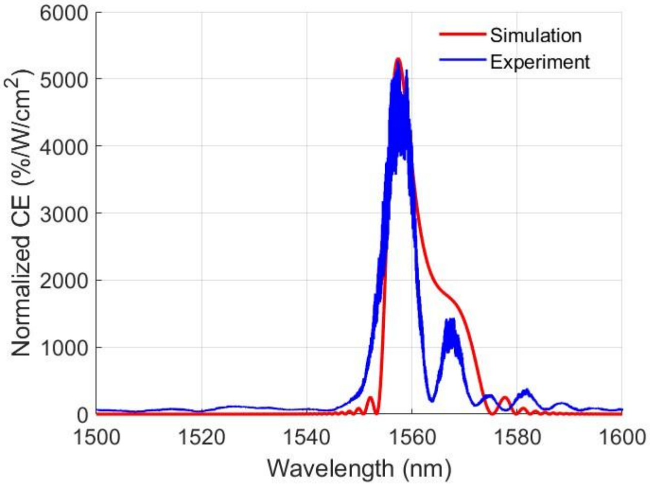

Figure 5.12: (a) Normalized conversion efficiency when correction terms of GV, GVD and TOD of -260 fs/mm, 75000 fs^2/mm, 1e7 fs^3/mm, respectively, are introduced to FF component.

SHG spectra at different temperatures are also taken as shown in figure 5.13 (a). By doing a linear fitting of the center wavelength of SHG and the temperature of the sample, the temperature dependence of the phase-matching wavelength can be found as -0.545 nm/K as shown in figure 5.13 (b).

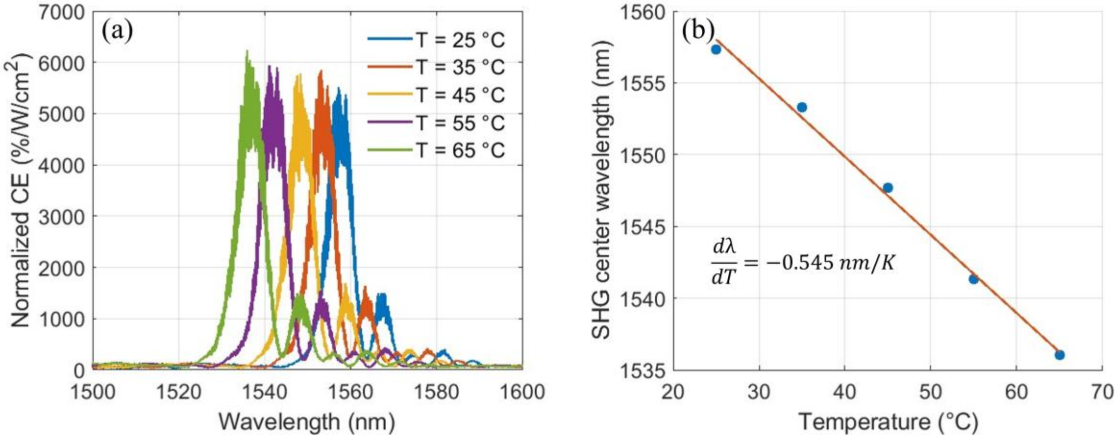

Figure 5.13: (a) Measured normalized conversion efficiency of SHG at different temperatures; (b) Linear fitting of center wavelength of SHG and the temperature of the sample.

5.6 Summary

In this chapter, we first derive the absolute and the normalized conversion efficiency of SHG of a waveguide. Then we compare different methods to achieve phase matching between FF and SH components, and experimental setup to realize periodic poling – the best way to achieve phase matching for high-efficiency SHG. Furthermore, we talk about the designs of the geometry of the waveguide with the refractive indices in the literature and the ones we measure using ellipsometry. Finally, we fabricate the waveguides based on the design, define the electrodes for periodic poling, and conduct it to achieve quasi phase matching between FF and SH components. We then observe high-efficiency SHG, and measure the conversion efficiency, which is in good agreement with the simulation in terms of the conversion efficiency. However, the spectral bandwidth and asymmetry of SHG cannot be accurately predicted by the simulation due to the sparse sample points during refractive indices measurement using ellipsometer. The realization of high-efficiency SHG paves the way for the realization of parametrically driven dissipative Kerr soliton, quadratic soliton, and other nonlinear processes based on second-order nonlinearity such as optical parametric amplification (OPA) and optical parametric oscillation (OPO).

Chapter VI

Stimulated Brillouin Scattering on Z-cut LNOI

6.1 Introduction and motivation

Stimulated Brillouin Scattering (SBS) is a third-order nonlinear effect generated from the interaction between optical waves and acoustic waves: when high power optical wave propagates inside a media, it induces local mechanical displacements in the medium starting to generate acoustic wave in the medium. The generated acoustic wave interacts with the optical wave facilitating the energy transferring between the optical and acoustic wave, which causes frequency shift in the scatter optical wave. SBS has been intensively studied and demonstrated in various platforms such as chalcogenide [80], silicon [81,82], and silicon nitride [83,84]. Empowered by the nature of the narrow gain bandwidth of SBS, the performance of applications has been enhanced such as optical atomic clock [85], optical gyroscope [86,87], optical signal processing [88], SBS microscopy [89,90,91], and quantum sensing [92].

Besides LN’s exceptional optical properties, it is well known that LN also possesses high piezoelectric and photo-elastic coefficients enabling strong interaction between optical waves and mechanical waves, making it suitable for various acousto-optic devices including acousto-optic modulator based on interdigital transducers

(IDTs) [93,94,95,96] frequency shifter [97,98], and tunable filter [99]. After SBS in LNOI started being studied theoretically and it has been found that strong SBS gain can exist in both X-cut and Z-cut LNOI [100,101], efforts have been put on the experimental demonstration [102,103]. The SBS gain in LNOI is generally lower compared to chalcogenide due to the poor mode overlapping between well confined optical modes in the waveguide and weakly confined surface acoustic modes (SAWs), which is propagating along the surface of LN. Making the waveguide suspended can address this issue to significantly improve SBS gain while ultra-high quality of the fabricated device is required otherwise rendered poor quality factor of the acoustic mode can be devastating to both gain and its bandwidth [104].

While most of the demonstrations are focused on co-polarized SBS when the pump and probe have the same polarization since it provides much higher gain than the cross-polarized SBS when the pump and probe have orthogonal polarizations, cross-polarized SBS offering another degree of freedom has been utilized in Brillouin Dissipative Kerr Soliton (Brillouin DKS) to narrow the comb linewidth, lower the timing jitter, and demonstrate the coveted turnkey microcomb [105]. The recent demonstrated applications of reconfigurable stimulated Brillouin laser (SBL) generator, mode converter, and efficient visible laser and comb generator on a bulk periodically poling LN crystal shows the merging potential of cross-polarized SBS generation of Brillouin quadratic soliton with excellent performance [106].

In this chapter, we will first discuss the design of waveguide geometry to obtain appreciable amount of SBS gain. Then, we will discuss in detail how we measure SBS gain in fabricated 14-cm long waveguide on Z-cut LNOI chips using pump-probe schematic with lock-in amplifier. Despite the discrepancy in the magnitude of SBS gain between the simulation expectation and experiments, simulation successfully predicted the frequency of some acoustic modes in a fairly accurate fashion where we experimentally observe SBS gain.

6.2 Design of waveguides on Z-cut LNOI

In SBS, an optical wave (pump) propagating inside the waveguide with angular frequency ω_p and propagation constant β_p will interact with phonon with angular frequency Ω_m and generate a scattered optical wave with either higher angular frequency $\omega_p + \Omega_m$ (anti-Stokes wave) or lower angular frequency $\omega_p - \Omega_m$ (Stokes wave). The beating between the pump and the scattered optical wave (SBS) serves as the source of acoustic wave whose propagation constant is given by $\beta_m = \beta_p - \beta_s$ dictated by the phase matching condition.

Here we only talk about the backward SBS (BSBS) that the propagation constant of SBS has the opposite sign but the same magnitude of the pump as the frequency of the pump is approximately the same as SBS. Thus, the propagation constant of the acoustic wave can be expressed as $\beta_m = 2\beta_p$. The normalized SBS gain per unit quality factor of the surface acoustic modes, and it can be expressed as equation 6.1 [107,108]:

$$\frac{G_B}{Q_m} = \frac{2\omega_p}{m_{eff}\Omega_m^2} |\int (f_{PE} + f_{RO})\, dA + \int f_{MB} dl|^2 \tag{6.1}$$

where m_{eff} stands for the linear mass density, and the f_{PE}, f_{RO}, and f_{MB} represent the contribution from photo-elastic, roto-optic, and the moving boundary, respectively to the SBS gain, and the contribution of photo-elastic term generally dominates among those three. By using the COMSOL model in [109], we can simulate the contribution from those three components separately and estimate the normalized SBS gain accurately: First, fundamental transverse-electric (TE_{01}) mode and fundamental transverse-magnetic (TM_{01}) mode are selected for pump and scattered optical waves, respectively, and the effective indices of them are calculated. Second, the mechanical displacement of the phase-matched acoustic modes with different acoustic frequencies Ω_m are calculated. Then, the spatial overlap integral is conducted to calculate the contribution of photo-elastic, roto-optic, and the moving boundary separately, which are finally added together to calculate the SBS gain coefficient per unit mechanical quality factor G_B/Q_m for different acoustic modes from the previous step.

For Z-cut LNOI, waveguides can be oriented along the entire XY plane of the thin film. We first consider two extreme cases when the waveguide is oriented along the X axis and the Y axis of the crystal, and the pump has fundamental TE mode while SBS has fundamental TM mode. The normalized SBS gain provided by different acoustic modes with their normalized displacement as the inserts for these two cases are plotted in figure 6.1 (a) and (b), respectively. The geometry of the waveguide is chosen to be top width of 2 μm, etch depth of 450 nm and the base angle of 70 degrees on a Z-cut LN with the total thickness of 450 nm.

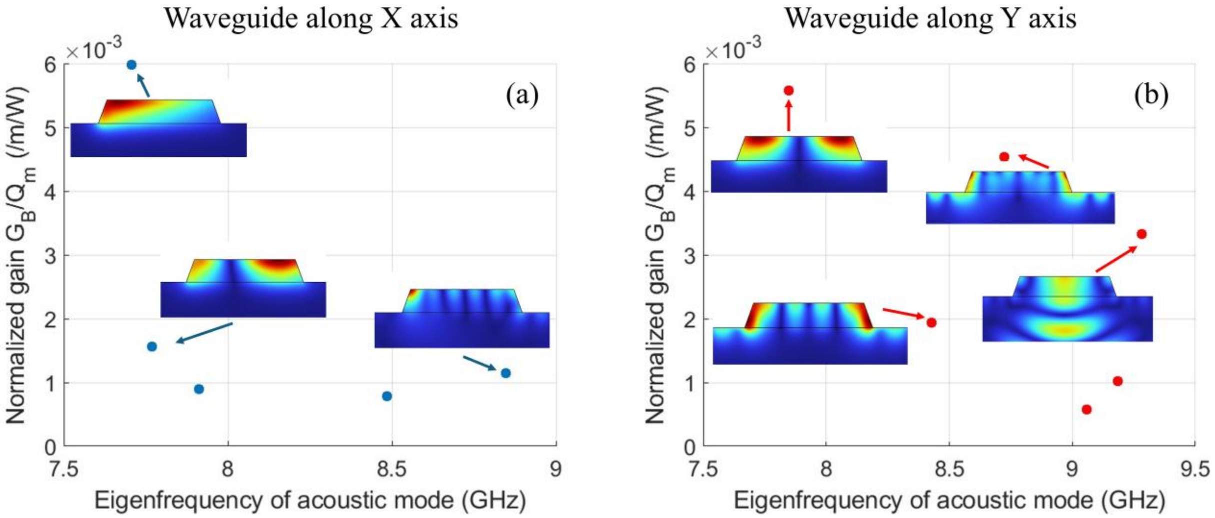

Figure 6.1: SBS gain provided by different acoustic modes (a) waveguide is oriented along X axis of the crystal; (b) waveguide is oriented along Y axis of the crystal; insets illustrate the normalized displacement of the corresponding acoustic mode.

Although the highest gain provided by X oriented waveguide is slightly higher, Y oriented waveguide has more acoustic modes that provide SBS gain. For the design of the waveguide geometry, we first simulate SBS gain with different etch depths while the total thickness of LN is kept at 450 nm the top width is fixed at 2 µm. The comparison of highest SBS gain and the corresponding mechanical quality factor in logarithm scale of the eigen acoustic mode, which is theoretically the highest mechanical quality factor that can be achieved, supported by the waveguides with different etch depths is shown in figure 6.2 (a).

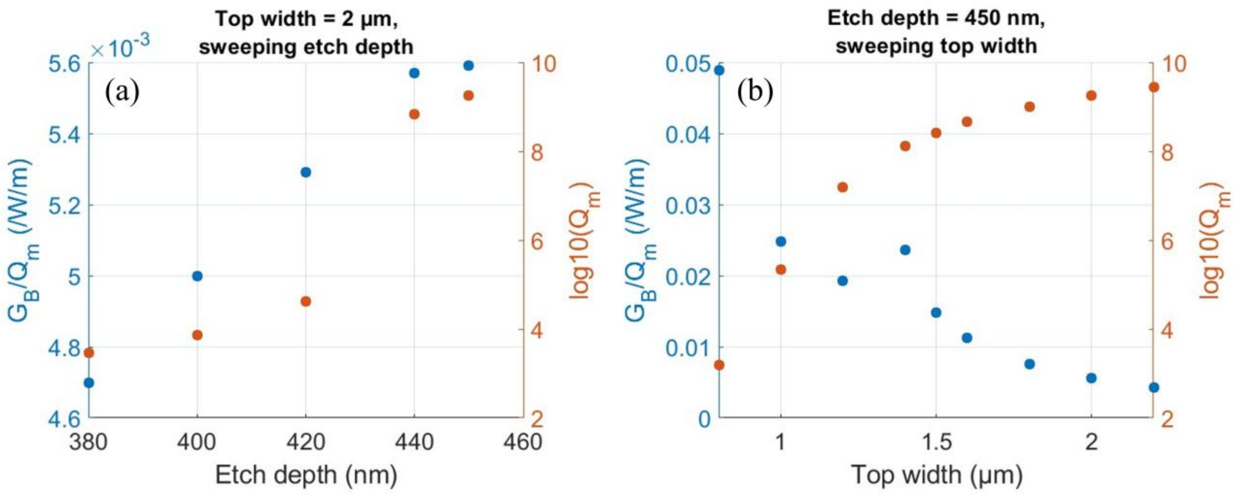

Figure 6.2: Simulated highest SBS gain provided by the acoustic mode with the corresponding mechanical quality factor for cross-polarized case when waveguide is oriented along Y axis on 450 nm-thick Z-cut LNOI with (a) different etch depths when top width is 2 μm; (b) different top width when the etch depth is 450 nm.

The results clearly show that both the normalized SBS gain, and the mechanical quality factor drop monotonically as the etch depth goes shallower. Besides, waveguides with etch depth of 450 nm can be fabricated with high quality by the optimized fabrication process described in chapter 2. Therefore, we go with the structure etched all the way to the bottom on 450 nm-thick LNOI. We then conduct the top width sweep with fixed 450 nm etch depth as shown in figure 6.2 (b). Despite the normalized SBS gain with 1.4 μm top width being abnormally high due to the contribution from the TE polarized component from the scattered optical eigenmode, the normalized SBS gain gets higher while the achievable mechanical quality factor gets lower as the waveguide narrows down in general. Although the normalized SBS gain is higher with narrower top width, the quality factor of a narrower waveguide could be lower resulting in even lower overall SBS gain.

6.3 Fabrication of spiral waveguides on Z-cut LNOI

According to the simulations, the highest gain that can be provided for cross-polarized case is right below 0.5 /m/W, which could make it difficult to observe experimentally, spiral waveguides with the total length of around 14 cm, etch depth of 450 nm, and top width of 1 μm, 1.5 μm, and 2 μm are fabricated on the same chip so that the total SBS gain that is linearly proportional to the length of the waveguide can be detected with decent signal-to-noise ratio and the total SBS can be compared between the waveguides with different top width.

The overview of spiral waveguides with three different top widths is shown in the microscope image in figure 6.3 (a), and the SEM image in figure 6.3 (b) illustrates the side view of two reversed 90-degree Euler bends [110,111] connected by a short straight waveguide at the center of the device in the encircled area of figure 6.3 (a) verifying the good etch quality of the waveguide.

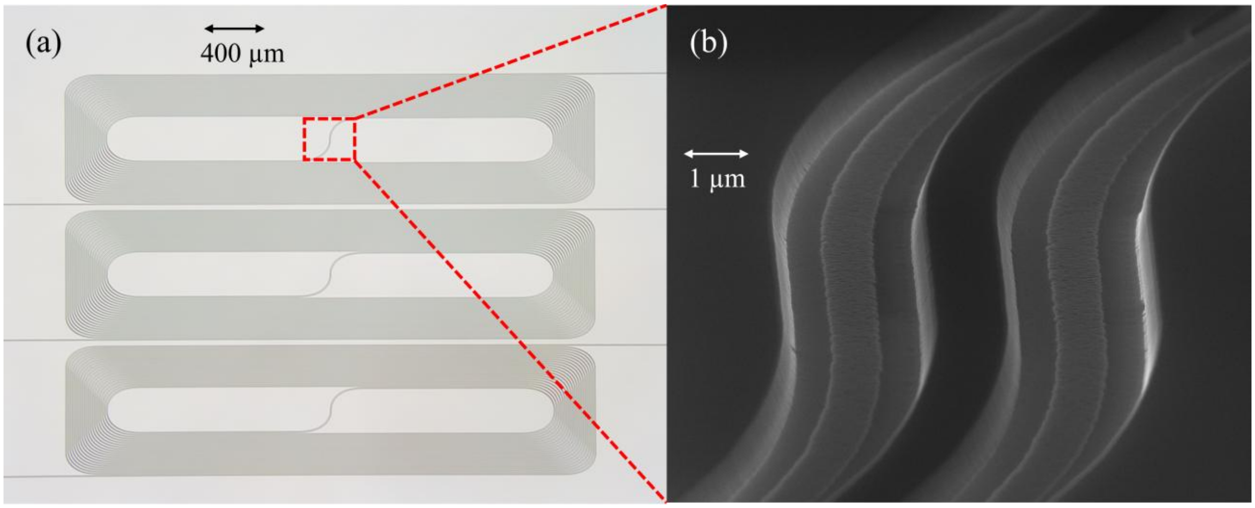

Figure 6.3: (a) microscope image of the spiral waveguide with top width 1 μm, 1.5 μm, and 2 μm (from top to the bottom); (b) SEM image of the side view of the encircled area in figure 5.3 (a).

6.4 Cross-polarized SBS gain characterization

The optical setup for SBS gain characterization is illustrated in figure 6.4. Toptica, with more frequency stability, is chosen to be the optical source with frequency f_p is split into two by a 90:10 fiber coupler. 10% of the optical power is sent into a C-band amplifier, which is sent to a free space coupling system and modulated by a chopper at 1 kHz after amplification. The amplified optical signal with modulation as the pump signal is then sent to circulator1 with PC1 before being coupled to the waveguide on chip from aspheric lens2 with a pair of mirrors (M1 and M2) and the collimator connected to PC1.

90% of the power from the 90:10 fiber coupler is sent to PC2 and is subsequently fed to IQ modulator to generate frequency component with frequency $f_p - f_{RF}$, which is then amplified by another C-band amplifier as the probe. The probe signal connected to PC3 to control its polarization is then coupled to the chip from the opposite as pump from a lensed fiber that is connected to port 2 of circulator2.

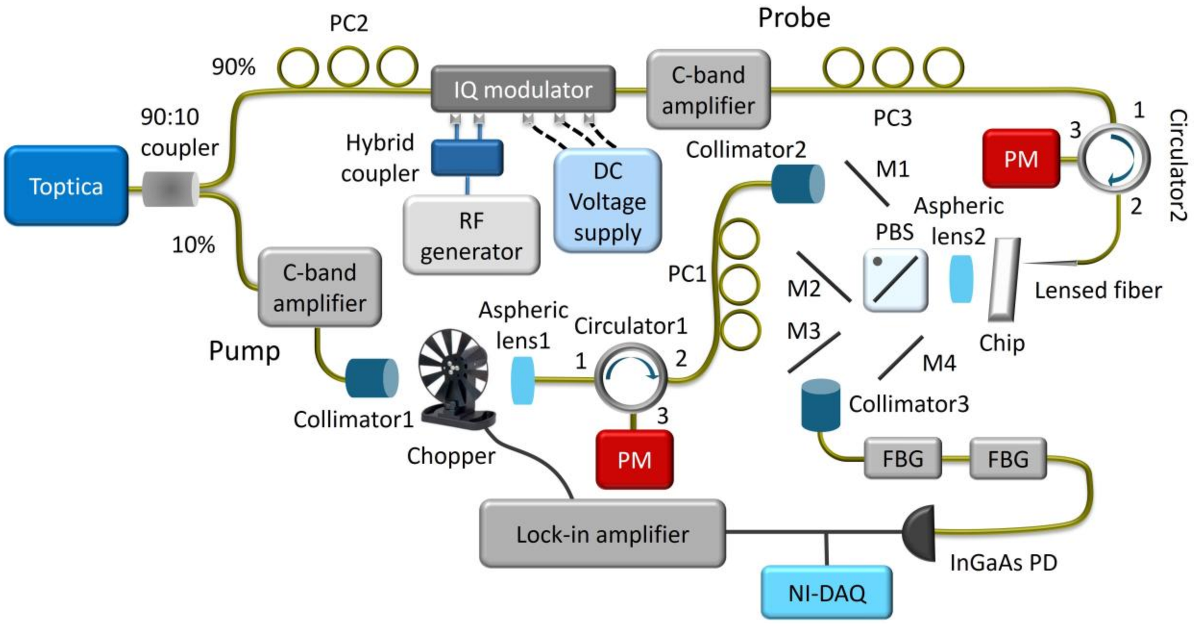

Figure 6.4: Schematic of the optical setup for SBS gain characterization. PC: polarization controller, PBS: polarizing beam splitter, FBG: fiber Bragg grating, M: mirror, PM: power meter, PD: photodetector.

For the cross-polarized case, probe with TM polarization is amplified in the spiral waveguide by the modulated pump signal propagating at the opposite direction and is outcoupled from aspheric lens2, reflected by PBS, and collected by collimator2 from the second pair of mirrors (M3 and M4). The outcoupled probe is then sent into two cascaded FBGs to spectrally filter the reflected pump from the facet of the waveguide and the residual optical signals f_p and $f_p + f_{RF}$ generated from the IQ modulator that is outcoupled along with the probe before being collected by InGaAs PD.

The voltage output of PD is then split into DC and AC components. DC component containing only unamplified probe signal by the spiral waveguide is collected by NI-DAQ while AC component only containing the amplified probe signal is collected by a lock-in amplifier whose measurement is locked at the modulation frequency of the chopper 1 kHz. Thus, the linear SBS gain at different RF frequency can be calculated from $\frac{V_{AC}+V_{DC}}{V_{DC}}$.

To locate where the SBS gain occurs, a rough step scan of the RF signal generator from 7.5 to 10 GHz every 5 MHz is conducted, and the SBS gain spectrum is shown in figure 6.5 (a).

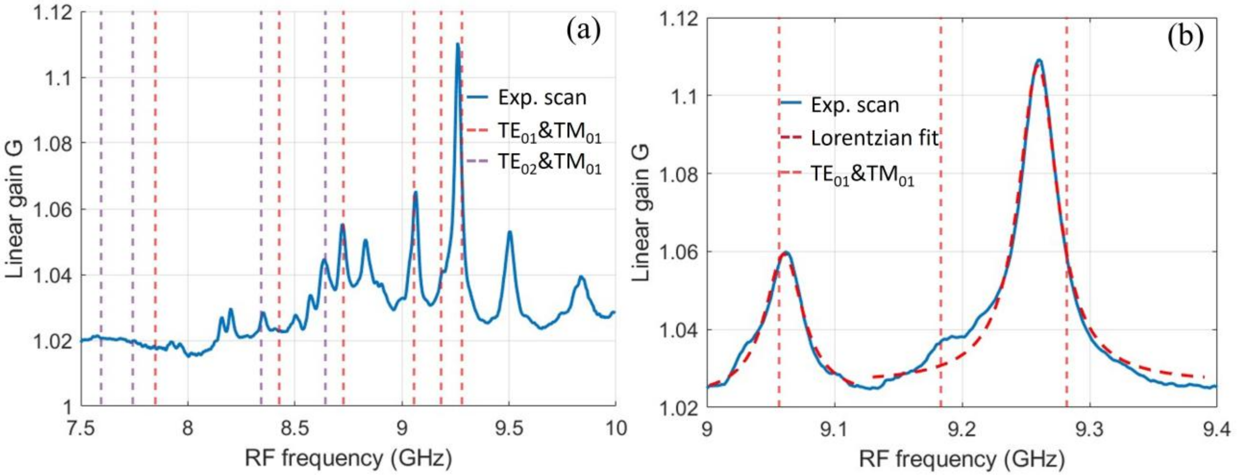

Figure 6.5: (a) SBS gain spectrum scanning from 7.5 to 10 GHz with 5 MHz as the interval; (b) SBS gain spectrum with Lorentzian fitting for three gain peaks scanning from 9 to 9.4 GHz with 2 MHz as the interval.

Although the highest gain predicted by simulation at RF frequency 7.8 GHz is not observed in experiments, there are more than 10 acoustic modes providing SBS gain from the scan. 4 of them whose counterparts can be found in the simulation as shown in figure 6.1 (b) as shown in the red dashed lines, another two peaks are contributed by the TE$_{02}$ of pump and TM$_{01}$ of the scattered wave as shown in the purple dashed lines in figure 6.5 (a). Two peaks that provide more than 6% gain occur at 9.06 and 9.265 GHz, which match well with where they are found at 9.066 and 9.282 GHz in the simulation results in figure 6.1 (b), respectively. To analyze the linewidth of these two peaks, another scan with an interval of 2 MHz from 9 to 9.4

GHz is conducted, and the spectrum with the Lorentzian fit of these two peaks is depicted in figure 5.5 (b). The linewidths of these two peaks are 36.1 and 37.4 MHz, which corresponds to quality factors of these three acoustic modes of 251 and 247, respectively.

To better estimate the normalized SBS gain G_B at 9.265 GHz, the gain spectra are collected with different on-chip pump power. The gain coefficient G_B can be expressed in equation 6.2 as:

$$G_B = \frac{lnG_{linear}}{L_{eff}P_p} \tag{6.2}$$

Where L_{eff} as the effective length of the waveguide is estimated to be 8.37 cm based on prior characterized propagation loss when the physical length is around 14 cm, and P_p is linear on-chip pump power. lnG_{linear} vs P_p is plotted in figure 6.6. By a linear polynomial fitting, $G_B L_{eff}$ is obtained from the slope of the fitted curve as 1.23 /W, therefore, G_B equals 14.7 /W/m.

The normalized gain per unit quality factor of the acoustic mode can be calculated by G_B/Q_m as 0.069 /W/m, which is 20 times higher than the simulation result. The discrepancy can be explained by the underestimation of the photo-elastic constant of thin film LN [112,113].

We also measure the SBS gain with the waveguide of 1.5 μm top width and the exact same length. The linear gain from the same acoustic mode at around 9.208 GHz is only around 2% while the linewidth of the gain is 57 MHz indicating lower quality factor of the acoustic mode than the one width top width 2 μm as shown in figure 6.7.

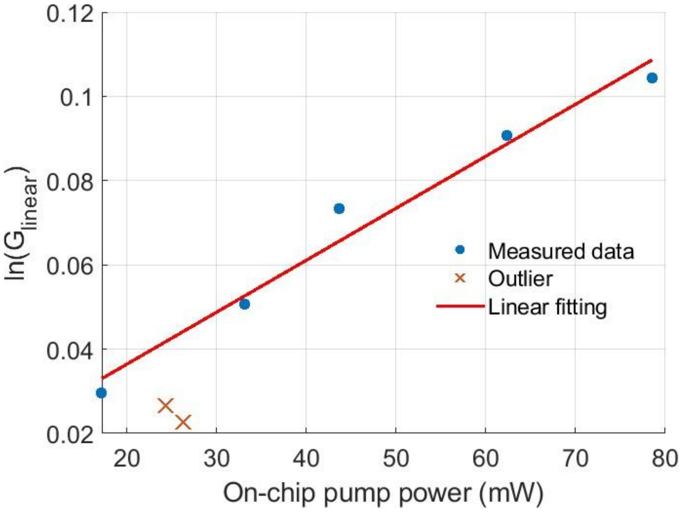

Figure 6.6: Logarithm of linear gain with natural base vs on-chip pump power with the linear polynomial fitting.

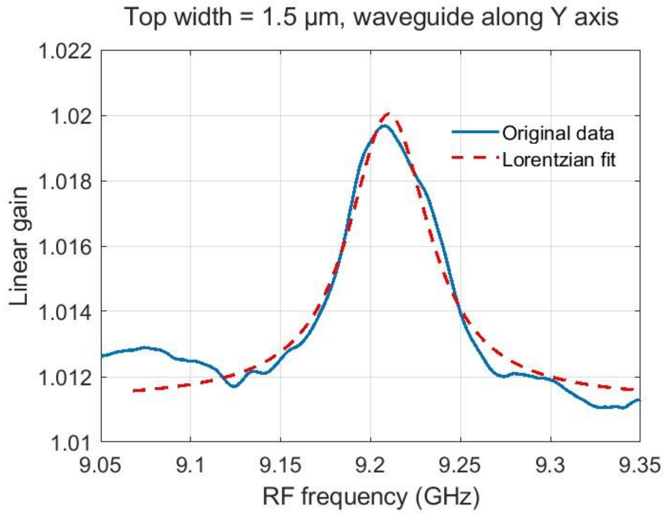

Figure 6.7: SBS gain spectrum of the Y oriented waveguide with 1.5 µm top width with on-chip pump power of 43 mW.

The calculated normalized SBS gain per unit quality factor is 0.042 /W/m with expected 0.0023 /W/m at 9.258 GHz from the simulation results, and the discrepancy between the experimental and simulated results is almost the same as the spiral waveguide with 2 μm top width as shown in the compared gain coefficient per unit gain between the simulation results and the experimental results.

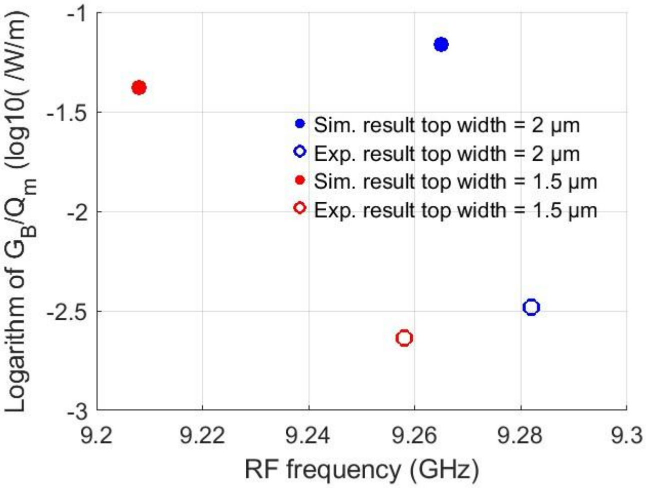

Figure 6.8: Comparison of SBS gain coefficient per unit quality factor between the simulation results and experimental results.

6.5 Summary

In this chapter, we first talk about the emerging interest of SBS on LN and its importance and potential applications of SBS on LNOI. Then, we talk about the design of the waveguide geometry to obtain high cross-polarized SBS gain on Z-cut LNOI and fabricated 14 cm-long spiral waveguides on Z-cut LNOI with the designed geometry. Finally, we experimentally observe and measure the cross-polarized SBS gain on both waveguides with top width of 1.5 μm and 2 μm. The measured normalized SBS gain for both waveguides are around 20 times of the simulated results, which might be originated from the underestimation of photo-elastic constant of thin film LN.

Chapter VII

Conclusion and outlook

7.1 Conclusion

To summarize this thesis: we start with the development and optimization of the fabrication process for LNOI with reduced sidewall roughness, the method to accurately measure the etch depth and the base angle of the fabricated structure that can be applied to all the simulation models to improve the fidelity of the designs, and the quality verification of the fabricated structure with SEM as the very foundation of the realization of miniaturized photonic devices on LNOI platform.

We then study and explore different methods to achieve optical wave coupling to LNOI chip with high coupling efficiency. Through dicing and polishing, we can typically achieve -5 to -8 dB coupling loss per facet without any specific designs. We also implement inverse design method in the low-loss broadband grating coupler design and experimentally demonstrate a grating coupler with 3.8 dB coupling loss over 1-dB and 3-dB bandwidth of 71.7 nm and over 120 nm, respectively, marking the state-of-the-art on similar LNOI platform. To further reduce the coupling loss, we design a double layer inverse taper edge coupling with sub -1 dB coupling loss over 100 nm spectral span at 1550 nm significantly reducing the power requirement of the lasers.

We then focus on the micro-ring resonator on LNOI, which is a perfect medium for diverse nonlinear interactions. We design a pulley-type coupler with circular bends wrapping around the micro-ring resonator to provide sufficient coupled power from the bus waveguide and a guideline of how we can adjust the parameters of the pulley-type coupler to achieve different coupling ratios to accommodate different application scenarios. We then discuss the importance of dispersion engineering and how to measure the GVD of the micro-ring resonator more accurately with MZI calibration system. We then measure the quality factor of a fabricated micro-ring resonator obtaining 2.2 million loaded quality factor that corresponds to the cavity finesse of over 3000 providing high cavity enhancement for nonlinear interactions.

Furthermore, we achieve quasi-phase-matching on designed waveguides with electric field periodic poling and demonstrate efficient SHG on Z-cut LNOI waveguide with both FF and SH components TM polarized to utilize the highest $\chi^{(2)}$ featuring 5200%/W/cm^2 normalized conversion efficiency, which is one the highest ever experimentally demonstrated. It also paves the way for other on-chip nonlinear interactions based on $\chi^{(2)}$ such as sum/different frequency generation, optical parametric amplification, and optical parametric oscillations.

Inspired by the recent theoretical findings on potential SBS gain on LNOI waveguide, we design and fabricate long waveguides with different top width that can potentially provide cross-polarized gain, and we, as one of the first groups, experimentally observe cross-polarized SBS gain with the normalized gain of 17 /W/m and gain linewidth 37.4 MHz, which is two narrower than the recently reported result [114]. The demonstration of cross-polarized SBS gain on LNOI will further enrich applications combined with its strong nonlinearity and electro-optic effect such as SBS enhanced frequency combs and RF filter with ultra-narrow bandwidth.

7.2 Future work

7.2.1 Parametrically driven dissipative Kerr soliton

By combining the periodic poling on the micro-ring resonator to achieve quasi-phase matching for high-efficiency SHG and the dispersion engineered micro-ring resonator with high quality factor, parametrically driven dissipative Kerr Soliton (PD-DKS) as described [41] could be achieved.

Although $\chi^{(2)}$ does not play a dominant effect in the formation of PD-DKS, it introduces perturbation on material third-order nonlinearity $\chi^{(3)}$, which dominates solitons generation in PD-DKS, from the cascaded quadratic process, and causes soliton annihilation resulting in deterministic single PD-DKS generation while operating above GVM threshold.

In our design, a continuous wave (CW) pump centered at 775 nm is used for the degenerate OPO process to generate signal at 1550 nm, which is the exact reverse process of SHG. TE modes are chosen for both pump and signal so that the minimal effective $\chi^{(2)}$ d_{11} is selected to lower the requirement of GVM between the pump and signal, which is chosen to be 124 fs/mm. The absolute GVD of the signal must be small as required by DKS generation while there is no specific requirement on GVD of the pump, and they are set to be -1.45 fs^2/mm and 270.8 fs^2/mm by the dispersion engineering design of the micro-ring resonator, respectively. TOD can no longer be ignored with such low GVD, which are added in the simulation with the calculated value 208.27 fs^3/mm and -284.51 fs^3/mm for signal and pump, respectively.

The dynamics of PD-DKS can be simulated after solving the coupled-wave equations with split-Fourier method described [41] after plugging in the forementioned values. TOD perturbed soliton at 1550 nm can be accessed with only 10 mW of on-chip power as shown in figure 7.1 (a) to (d).

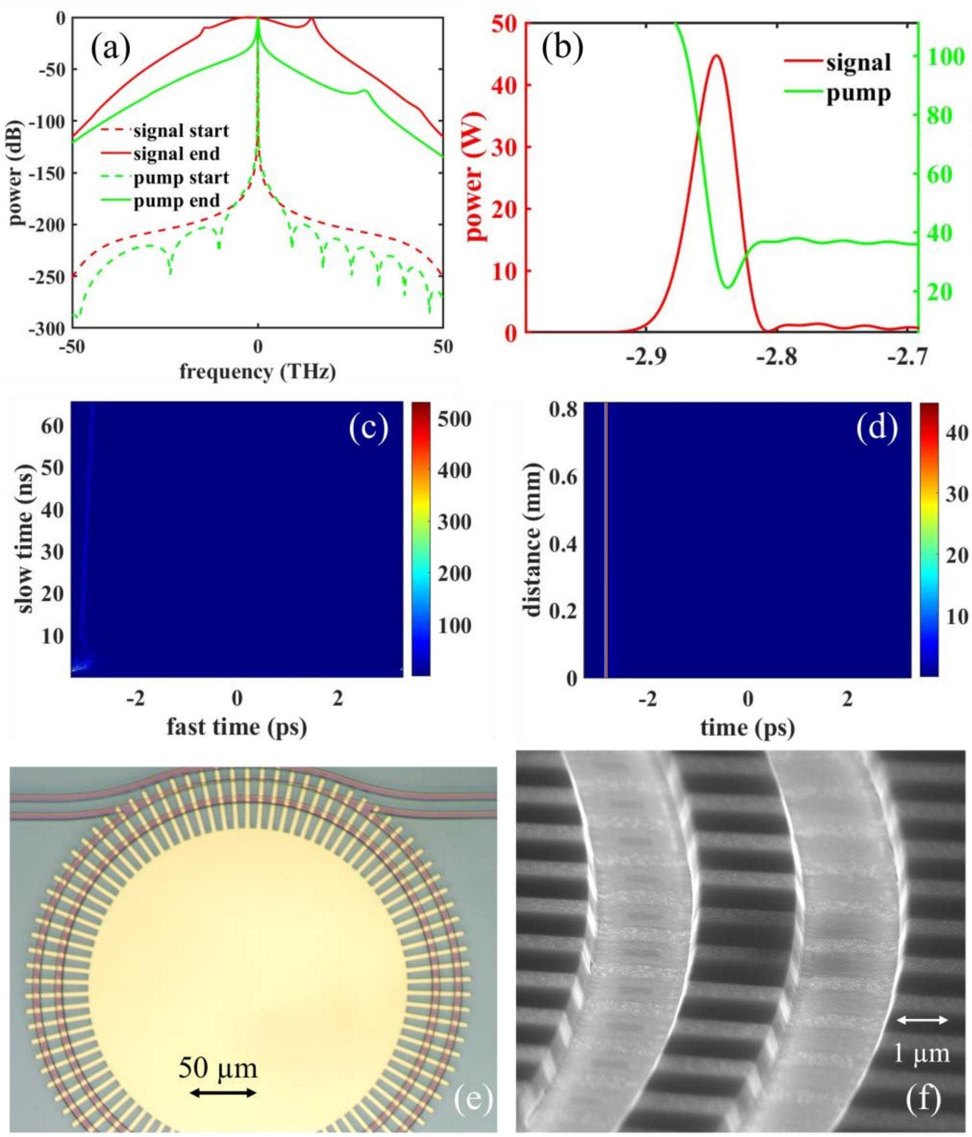

Figure 7.1: (a) Comparison of the spectra of pump and signal between the initial condition and at the end of the last roundtrip; (b) temporal profile of pump and signal at the last roundtrip; (c) temporal evolution of the signal; (d) temporal evolution of the signal within the last roundtrip; (e) microscope image of the electrodes on the fabricated micro-ring resonator; (f) SEM image of the sideview of the micro-ring resonator after periodic poling and electrodes removal.

As shown in figure 7.1 (b), pulse shorter than 100 fs is generated for signal at 1550 nm and signal soliton starts being stabilized after around 1800 roundtrips as depicted in figure 7.1 (c). Figure 7.1 (d) plots how the signal evolves within the last roundtrip in the temporal domain, which further verifies the formation of single soliton.

The electrodes for the periodic poling of prior fabricated micro-ring resonators on 450 nm-thick Z-cut LNOI are patterned with similar process described in 5.4 as shown in figure 7.1 (e), after which micro-ring resonators are periodically poled using the same setup illustrated in figure 5.4 with 600 V peak voltage while other parameters of the high-voltage pulses remain the same. Stark contrast between the poled and unpoled region of the micro-ring resonator after periodic poling and electrodes removal as shown in figure 7.1 (f) indicates successful poling providing appropriate platform for PD-DKS generation.

7.2.2 Microwave filter with ultra-narrow linewidth

As mentioned in the introduction, LN also possesses high electro-optic (EO) coefficient making it suitable for EO modulators [115] and EO frequency combs [116]. To utilize the highest EO coefficient while minimizing the scattering loss induced by the electrode pads where the voltage signal is applied, X-cut LNOI is chosen over Z-cut LNOI and the waveguide is oriented along Y axis of the crystal so that the voltage can be applied on the electrode pads patterned on both sides of the waveguide to generate the electric field for high-efficiency EO modulation.

We also fabricate such waveguide on 400 nm-thick X-cut LNOI platform with the optimized fabrication process for Z-cut LNOI and pattern the electrode pads as described in section 5.4. The microscope image of the overview of the fabricated devices with different electrode pad separations and the SEM image of the sideview of the waveguide and the electrode are shown in figure 7.2 (a) and (b), respectively.

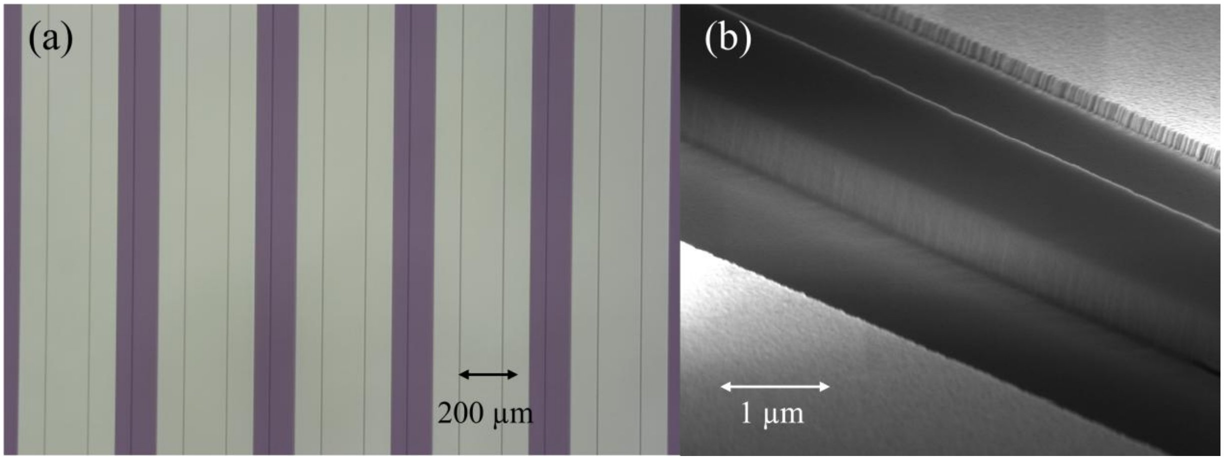

Figure 7.2: (a) Microscope image of the overview of waveguides and electrode pads with different separation; (b) SEM image of the sideview of the waveguide with electrode pads on both sides.

By measuring the output from an external interferometer with one of the arms connected to the waveguide when a ramp superimposed on a sinusoidal voltage signal with frequency 100 kHz is applied to one of the electrode pads as shown in figure 7.3 (b) while the other electrode pad is grounded, V_π can be obtained from the output of the PD as shown in figure 7.3 (a).

As shown in the upper figure in figure 7.3, the voltage output from the PD starts to be cut off on both peak and valley within one period indicating V_{pp} of the applied signal just exceeds V_π required to achieve a π phase shift. Therefore, $V_\pi L$ can be calculated by multiplying V_π and the length of the waveguide 4.5 mm to be 2.7 $V \cdot cm$, which is close to the simulated result 2.53 $V \cdot cm$.

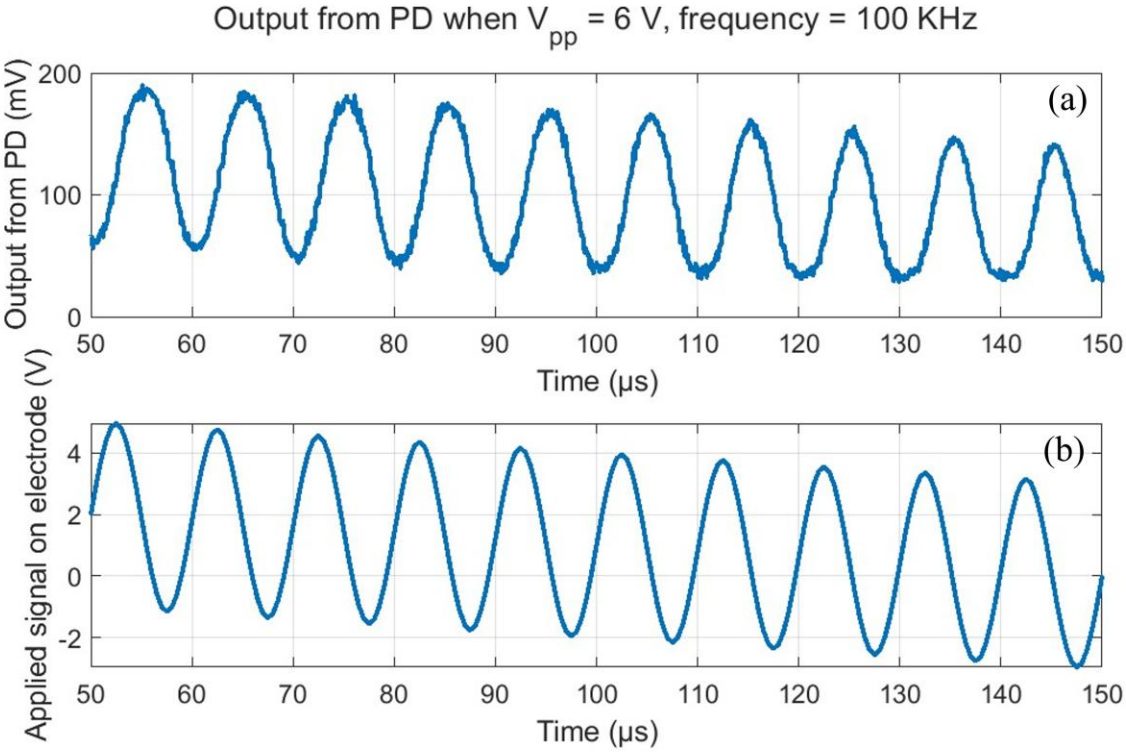

Figure 7.3: (a) Voltage output from PD; (b) Voltage signal applied to one of the electrode pads.

By combining the EO modulator and the SBS gain we demonstrate in chapter 6, we will be able to achieve tunable microwave filters with ultra-narrow bandwidth dictated by the linewidth of SBS gain on LNOI platform without the need of the integration of hybrid platforms as demonstrated in [117].

Reference

---

1 H. K. Tsang, and Y. Liu, “Nonlinear optical properties of silicon waveguides,” Semiconductor Science and Technology 23(6), 064007 (2008).

2 K. Ikeda, R. E. Saperstein, N. Alic, and Y. Fainman, “Thermal and Kerr nonlinear properties of plasma-deposited silicon nitride/silicon dioxide waveguides,” Optics express 16(17), 12987-12994 (2008).

3 X. Liu, A. W. Bruch, and H. X. Tang, “AlN nonlinear optics and integrated photonics,” Semiconductors and Semimetals 107, 223-281 (2021).

4 B. Liu, “Research progress of second-order nonlinear optical effects based on lithium niobate on insulator waveguides,” In AIP Conference Proceedings, vol. 3017(1), AIP Publishing, 2023.

5 L.Ledezma, R. Sekine, Q. Guo et al., “Intense optical parametric amplification in dispersion-engineered nanophotonic lithium niobate waveguides,” Optica 9(3), 303-308 (2022).

6 Kent C. Burr, C. L. Tang, M. A. Arbore, and M. M. Fejer, “High-repetition-rate femtosecond optical parametric oscillator based on periodically poled lithium niobate,” Applied Physics Letters 70(25), 3341-3343 (1997).

7 M. Zhang, C. Wang, P. Kharel et al., “Integrated lithium niobate electro-optic modulators: when performance meets scalability,” Optica 8(5), 652-667 (2021).

8 M. Bruel, “Silicon on insulator material technology,” Electron. Lett. 31, 1201–1202 (1995).

9 M. Levy and A. M. Radojevic, “Single-crystal lithium niobate films by crystal ion slicing,” in Wafer Bonding, Springer Series in Materials Science (Springer, 2004), 417–450 (2004).

---

10 D. Zhu, L. Shao, M. Yu et al., “Integrated photonics on thin-film lithium niobate,” Advances in Optics and Photonics 13(2), 242-352 (2021).

11 E. L. Wooten K. M. Kissa, A. Y.-Y. et al., “A review of lithium niobate modulators for fiber-optic communications systems,” IEEE Journal of selected topics in Quantum Electronics 6(1), 69-82 (2000).

12 D. Marpaung, J. Yao, and J. Capmany, “Integrated microwave photonics,” Nature photonics 13(2), 80-90 (2019).

13 C. Sun, M. T. Wade, Y. Lee et al., “Single-chip microprocessor that communicates directly using light,” Nature 528(7583) 534-538 (2015).

14 M. Karpiński, M. Jachura, L. J. Wright, and B. J. Smith, “Bandwidth manipulation of quantum light by an electro-optic time lens,” Nature Photonics 11(1) 53-57 (2017).

15 M. Li, J. Ling, Y. He et al., “Lithium niobate photonic-crystal electro-optic modulator,” Nature Communications 11(1), 4123 (2020).

16 Z. L. Newman, V. Maurice, T. Drake et al., “Architecture for the photonic integration of an optical atomic clock,” Optica 6 680–685 (2019).

17 G. Ulliac, V. Calero, A. Ndao et al., “Argon plasma inductively coupled plasma reactive ion etching study for smooth sidewall thin film lithium niobate waveguide application,” Optical Materials 53, 1-5 (2016).

18 R. Zhuang, J. He, Y. Qi et al., “High-Q Thin-Film Lithium Niobate Microrings Fabricated with Wet Etching,” Advanced Materials 35 (3), 2208113 (2023).

19 J.-Y. Chen, C. Tang, Z.-H. Ma et al., “Efficient and highly tunable second harmonic generation in Z-cut periodically poled lithium niobate nanowaveguides,” Optics Letters 45(13), 3789–3792 (2020).

---

20 J. Lu, J. B. Surya, X. Liu et al., "Periodically poled thin-film lithium niobate microring resonators with a second-harmonic generation efficiency of 250,000%/W," Optica 6(12), 1455–1460 (2019).

21 L. Ledezma, A. Roy, L. Costa et al., "Octave-spanning tunable infrared parametric oscillators in nanophotonics," Sci. Adv. 9(30), eadf9711 (2023).

22 C. Wang, M. Zhang, X. Chen et al., "Integrated lithium niobate electro-optic modulators operating at CMOS-compatible voltages," Nature 562(7725), 101–104 (2018).

23 M. Yu, B. Desiatov, Y. Okawachi et al., "Coherent two-octave-spanning supercontinuum generation in lithium-niobate waveguides," Opt. Lett. 44(5), 1222–1225 (2019).

24 M. Yu, D. Barton III, R. Cheng et al., "Integrated femtosecond pulse generator on thin-film lithium niobate," Nature 612(7939), 252–258 (2022).

25 Y. He, Q.-F. Yang, J. Ling et al., "Self-starting bi-chromatic LiNbO3 soliton microcomb," Optica 6(9), 1138–1144 (2019).

26 M. Nie and S.-W. Huang, "Quadratic soliton mode-locked degenerate optical parametric oscillator," Opt. Lett. 45(8), 2311–2314 (2020).

27 Y. Li, X. Huang, Z. Li et al., "Efficient grating couplers on a thin film lithium niobate–silicon rich nitride hybrid platform," Opt. Lett. 45(24), 6847–6850 (2020).

28 Z. Ruan, J. Hu, Y. Xue et al., "Metal based grating coupler on a thin-film lithium niobate waveguide," Opt. Express 28(24), 35615–35621 (2020).

29 B. Chen, Z. Ruan, K. Chen et al., "One-dimensional grating coupler on lithium-niobate-on-insulator for high-efficiency and polarization-independent coupling," Opt. Lett. 48(6), 1434–1437 (2023).

---

30 X. Zhou, Y. Xue, F. Ye et al., “High coupling efficiency waveguide grating couplers on lithium niobate,” Opt. Lett. 48(12), 3267–3270 (2023).

31 B. Chen, Z. Ruan, X. Fan et al., “Low-loss fiber grating coupler on thin film lithium niobate platform,” APL Photonics 7(7), 076103 (2022).

32 E. Lomonte, F. Lenzini, and W. H. P. Pernice, “Efficient self-imaging grating couplers on a lithium-niobate-on-insulator platform at near-visible and telecom wavelengths,” Opt. Express 29(13), 20205–20216 (2021).

33 S. Yang, Y. Li, J. Xu et al., “Low loss ridge-waveguide grating couplers in lithium niobate on insulator,” Opt. Mater. Express 11(5), 1366–1376 (2021).

34 Y. Xie, M. Nie, and S.-W. Huang. "Inverse-designed broadband low-loss grating coupler on thick lithium-niobate-on-insulator platform." Applied Physics Letters 124(5), (2024).

35 H. Carfagno, M. A. Guidry, J. Yang et al., “Inverse designed couplers for use in gallium arsenide photonics,” ACS Photonics 10(5), 1286–1292 (2023).

36 J. Yoon, J. Y. Kim, J. Kim et al., “Inverse design of a Si-based high-performance vertical-emitting meta-grating coupler on a 220nm silicon-on-insulator platform,” Photonics Res. 11(6), 897–905 (2023).

37 V.R. Almeida, R.R. Panepucci, and M. Lipson, “Nanotaper for compact mode conversion,” Optics letters, 28(15), 1302-1304 (2003).

38 Y. Li, T. Lan, J. Li et al., “High-efficiency edge-coupling based on lithium niobate on an insulator wire waveguide,” Applied Optics (59), 6694-6701 (2020).

39 M. Pu, L. Liu, H. Ou et al., “Ultra-low-loss inverted taper coupler for silicon-on-insulator ridge waveguide,” Optics Communications 283 (19), 3678-3682 (2010).

---

40 M. Nie, Y. Xie, B. Li, and S.-W. Huang, “Photonic frequency microcombs based on dissipative Kerr and quadratic cavity solitons,” Progress in Quantum Electronics 86, 100437 (2022).

41 M. Nie, Y. Xie, and S.-W. Huang, “Deterministic generation of parametrically driven dissipative Kerr soliton,” Nanophotonics 10 (6), 1691-1699 (2021).

42 M. Nie, and Shu-Wei Huang, “Quadratic soliton mode-locked degenerate optical parametric oscillator,” Optics Letters 45(8), 2311-2314(2020).

43 M. Nie, S.-W. Huang, “Symbiotic quadratic soliton mode-locked non-degenerate optical parametric oscillators,” Optics Letters 45 4184–4187, (2020).

44 C. Tang, M. Nie, J. Chen et al., “Broadband frequency comb generation through cascaded quadratic nonlinearity in thin-film lithium niobate micro resonators,” Optics Letters 49 (9), 2449-2452 (2024).

45 Y. Song, Y. Hu, X. Zhu et al., “Octave-spanning Kerr soliton frequency combs in dispersion-and dissipation-engineered lithium niobate microresonators,” Light: Science & Applications 13 (1), 225 (2024).

46 X. Zhu, Y. Hu, S. Lu, et al., “Twenty-nine million intrinsic Q-factor monolithic microresonators on thin-film lithium niobate,” Photonics Research 12 (8), A63-A68 (2024).

47 Q.-F. Yang, B. Shen, H. Wang et al., “Vernier spectrometer using counter propagating soliton microcombs,” Science 363 (6430) 965-968, (2019).

48 L. Stern, J.R. Stone, S. Kang et al., “Direct Kerr frequency comb atomic spectroscopy and stabilization,” Science Advances 6 (eaax6230), (2020).

49 D.T. Spencer, T. Drake, T.C. Briles et al., “An optical-frequency synthesizer using integrated photonics,” Nature 557 81–85, (2018).

---

50 M.-G. Suh, Q.-F. Yang, K.Y. Yang et al., "Microresonator soliton dual-comb spectroscopy," Science 354 600–603, (2016).

51 X. Ji, X. Yao, A. Klenner et al., "Chip-based frequency comb sources for optical coherence tomography," Optics Express 27 19896–19905, (2019).

52 P.J. Marchand, J. Riemensberger, J.C. Skehan et al. "Soliton microcomb based spectral domain optical coherence tomography," Nature Communications. 12 1–9, (2021).

53 C. Bao, M.-G. Suh, and K. Vahala, "Microresonator soliton dual-comb imaging," Optica 6, 1110–1116 (2019).

54 J. Pfeifle, V. Brasch, M. Lauermann et al., "Coherent terabit communications with microresonator Kerr frequency combs," Nature Photonics. 8, 375–380 (2014).

55 P. Marin-Palomo, J.N. Kemal, M. Karpov et al., "Microresonator-based solitons for massively parallel coherent optical communications," Nature 546, 274–279 (2017).

56 A. Fülöp, M. Mazur, A. Lorences-Riesgo et al., "Long-haul coherent communications using microresonator-based frequency combs," Optics Express 25, 26678–26688 (2017).

57 P. Trocha, M. Karpov, D. Ganin et al., "Ultrafast optical ranging using microresonator soliton frequency combs," Science 359, 887–891 (2018).

58 Z. Yang, M. Jahanbozorgi, D. Jeong et., "A squeezed quantum microcomb on a chip," Nature Communications 12, 1–8 (2021).

59 F. Vanier, C. L. Mela, A. H et al., "Intrinsic quality factor determination in whispering gallery mode microcavities using a single Stokes parameters measurement," Optics express 19 (23), 23544-23553 (2011).

60 W. Bogaerts, P. D. Heyn, T. V. Vaerenbergh et al., "Silicon microring resonators," Laser & Photonics Reviews 6 (1), 47-73 (2012).

---

61 D.-P. Cai, J.-H. Lu, C.-C. Chen et al., “Compact pulley-type microring resonator with high quality factor,” Applied Physics Express 7 (11), 112202 (2014).

62 D.-P Cai, J.-H. Lu, C.-C. Chen et al., “High Q-factor microring resonator wrapped by the curved waveguide,” Scientific reports 5 (1), 1-8 (2015).

63 M.-H. Yen, P.-Y. Feng, C.-E. Lin et al., “Optimization of pulley-type ring resonator with waveguide offset,” Micromachines 9 (5), 226 (2018).

64 P. Parra-Rivas, D. Gomila, F. Leo et al., “Third-order chromatic dispersion stabilizes Kerr frequency combs,” Optics letters 39 (10), 2971-2974 (2014).

65 S-W. Huang, H. Zhou, J. Yang et al., “Mode-locked ultrashort pulse generation from on-chip normal dispersion microresonators,” Physical review letters 114 (5), 053901 (2015).

66 G. J. Edwards, and M. Lawrence, “A temperature-dependent dispersion equation for congruently grown lithium niobate,” Optical and quantum electronics 16, 373-375 (1984).

67 Dieter H. Jundt, “Temperature-dependent Sellmeier equation for the index of refraction, n_e, in congruent lithium niobate,” Optics Letters 22 (20), 1553-1555 (1997).

68 S. Yue, M. N. Slipchenko, and J-X. Cheng, “Multimodal nonlinear optical microscopy,” Laser & photonics reviews 5(4), 496-512 (2011).

69 Z. L. Newman, V. Maurice, T. Drake et al., “Architecture for the photonic integration of an optical atomic clock,” Optica 6, 680–685 (2019).

70 X. Guo, C.-L. Zou, C. Schuck et al., “Parametric down-conversion photon-pair source on a nanophotonic chip,” Light: Science & Applications 6(5), e16249-e16249 (2017).

---

71 M. M. Fejer, G. A. Magel, D. H. Jundt, and R. L. Byer, “Quasi-phase-matched second harmonic generation: tuning and tolerances,” IEEE J. Quantum Electron. 28, 2631–2654 (1992).

72 M. Jankowski, C. Langrock, B. Desiatov, et al., “Ultrabroadband nonlinear optics in nanophotonic periodically poled lithium niobate waveguides,” Optica 7(1), 40-46 (2020).

73 R. W. Boyd, “Nonlinear Optics,” Chapter 1 and 2 (Academic Press, 2008).

74 R. Luo, “Nonlinear nanophotonics in lithium niobate,”.

75 Robert W Boyd, Alexander L Gaeta, and Enno Giese. Nonlinear optics. In Springer Handbook of Atomic, Molecular, and Optical Physics, 1097–1110. Springer, 2008.

76 R. Luo, Y. He, H. Liang et al., “Highly tunable efficient second-harmonic generation in a lithium niobate nanophotonic waveguide,” Optica 5(8), 1006-1011 (2018).

77 C. J. Xin, S. Lu, J. Yang et al., “Wavelength-accurate and wafer-scale process for nonlinear frequency mixers in thin-film lithium niobate,” arXiv preprint arXiv:2404.12381 (2024).

78 Y. Tang, T. Ding, Y. Zhang et al., “Octave-Spanning Second-Harmonic Generation in Dispersion-Engineered Lithium Niobate-on-Insulator Microwaveguide,” Advanced Photonics Research 5(12), 2400051(2024).

79 P.-K. Chen, I. Briggs, C. Cui et al., “Adapted poling to break the nonlinear efficiency limit in nanophotonic lithium niobate waveguides,” Nature Nanotechnology 19(1), 44-50 (2024).

80 R. Pant, C. G. Poulton, D.-Y. Choi et al., “Onchip stimulated Brillouin scattering,” Opt. Express 19, 8285–8290 (2011).

---

81 H. Shin, W. Qiu, R. Jarecki et al., “Tailorable stimulated Brillouin scattering in nanoscale silicon waveguides,” Nat. Commun. 4, 1944 (2013).

82 R. Van Laer, B. Kuyken, D. Van Thourhout, and R. Baets, “Interaction between light and highly confined hypersound in a silicon photonic nanowire,” Nat. Photonics 9, 199–203 (2015).

83 F. Gyger, J. Liu, F. Yang, J. He et al., “Observation of stimulated Brillouin scattering in silicon nitride integrated waveguides,” Phys. Rev. Lett. 124, 013902 (2020).

84 R. Botter, K. Ye, Y. Klaver et al., “Guided-acoustic stimulated Brillouin scattering in silicon nitride photonic circuits,” Sci. Adv. 8, eabq2196 (2022)

85 W. Loh, J. Stuart, D. Reens, et al., “Operation of an optical atomic clock with a Brillouin laser subsystem,” Nature 588(7837), 244-249 (2020).

86 Y.-H. Lai, M.-G. Suh, Y.-K. Lu et al., “Earth rotation measured by a chip-scale ring laser gyroscope,” Nature Photonics 14(6), 345-349 (2020).

87 Y.-H. Lai, Y.-K. Lu, M.-G. Suh et al., “Observation of the exceptional-point-enhanced Sagnac effect,” Nature 576(7785), 65-69 (2019).

88 M. Santagiustina, S. Chin, N. Primerov, et al., “All-optical signal processing using dynamic Brillouin gratings,” Scientific reports 3(1), 1594 (2013).

89 G. Scarcelli, and S. H. Yun “Confocal Brillouin microscopy for three-dimensional mechanical imaging,” Nature photonics 2(1), 39-43 (2008).

90 I. Remer, R. Shaashoua, N. Shemesh et al., “High-sensitivity and high-specificity biomechanical imaging by stimulated Brillouin scattering microscopy,” Nature Methods 17(9), 913-916 (2020).

---

91 F. Yang, C. Bevilacqua, S. Hambura et al., “Pulsed stimulated Brillouin microscopy enables high-sensitivity mechanical imaging of live and fragile biological specimens,” Nature Methods 20(12), 1971-1979 (2023).

92 C. L. Degen, Friedemann Reinhard, and Paola Cappellaro “Quantum sensing,” Reviews of modern physics 89(3), 035002 (2017).

93 L. Cai, A. Mahmoud, M. Khan et al., “Acousto-optical modulation of thin film lithium niobate waveguide devices,” Photonics Research 7(9), 1003-1013 (2019).

94 M. Mahmoud, L. Cai, A. Mahmoud et al., “Electro-optically controlled acousto-optic racetrack modulator etched in LNOI platform,” 2018 IEEE Micro Electro Mechanical Systems (MEMS), 743-746 (2018).

95 C. J. Sarabalis, T. P. McKenna, R. N. Patel et al., “Acousto-optic modulation in lithium niobate on sapphire,” APL Photonics 5(8), (2020).

96 C. J. Sarabalis, R. Van Laer, R. N. Patel et al., “Acousto-Optic Modulation of a Wavelength-Scale Waveguide,” Optica 8(4), 477 (2021).

97 L. Shao, M. Yu, S. Maity et al., “Microwave-to-Optical Conversion Using Lithium Niobate Thin-Film Acoustic Resonators,” Optica 6(12), 1498 (2019).

98 L. Shao, N.Sinclair, J. Leatham et al., “Integrated Microwave Acousto-Optic Frequency Shifter on Thin-Film Lithium Niobate,” Opt. Express 28(16), 23728 (2020).

99 D.Marpaung, B. Morrison, M. Pagani et al., “Low-power, chip-based stimulated Brillouin scattering microwave photonic filter with ultrahigh selectivity,” Optica 2(2), 76-83 (2015).

100 C. C. Rodrigues, R. O. Zurita, T. PM Alegre, and G. S. Wiederhecker “Stimulated Brillouin scattering by surface acoustic waves in lithium niobate waveguides,” JOSA B 40(5), D56-D63 (2023).

---

101 H. Liu, Y. Yu, K. Li et al., “High-gain lithium niobate brillouin laser with tunable phonon frequency of 1~ 31 GHz,” Frontiers in Physics 12, 1402002 (2024).

102 K. Ye, H. Feng, R. te Morsche et al., “Brillouin photonics engine in the thin-film lithium niobate platform,” arXiv preprint arXiv: 2411. 06599 (2024).

103 C. C. Rodrigues, N. J. Schilder, R. O. Zurita et al., “On-chip backward stimulated Brillouin scattering in lithium niobate waveguides,” In 2024 Conference on Lasers and Electro-Optics (CLEO), (1-2). IEEE, 2024.

104 S. Yu, R. Zhou, G. Yang et al., “On-chip Brillouin Amplifier in Suspended Lithium Niobate Nanowaveguides,” arXiv preprint arXiv: 2412. 11748 (2024).

105 M. Nie, J. Musgrave, K. Jia et al., “Turnkey photonic flywheel in a microresonator-filtered laser,” Nature Communications 15(1) 55 (2024).

106 M. Nie, J. Musgrave, and S.-W. Huang “Cross-polarized stimulated Brillouin scattering empowered photonics,” arXiv preprint arXiv: 2405. 15888 (2024).

107 G. S.Wiederhecker, P. Dainese, and T. P. Mayer Alegre “Brillouin optomechanics in nanophotonic structures,” APL photonics 4(7) (2019).

108 C. Wolff, M. J. Steel, B. J. Eggleton, and C. G. Poulton “Stimulated Brillouin scattering in integrated photonic waveguides: Forces, scattering mechanisms, and coupled-mode analysis,” Physical Review A 92(1), 013836 (2015).

109 C. C. Rodrigues, R. O. Zurita, T. P. M. Alegre, and G. S. Wiederhecker, “Dataset and simulation files for article "Stimulated Brillouin scattering by surface acoustic waves in lithium niobate waveguides",” Zenodo (2022), https://zenodo.org/record/7314443#.ZCwcMXbMKM9.

110 F. Vogelbacher, S. Nevlacsil, M. Sagmeister et al., “Analysis of silicon nitride partial Euler waveguide bends,” Optics express 27(22), 31394-31406 (2019).

---

111 X. Ji, J. Liu, J. He et al., “Compact, spatial-mode-interaction-free, ultralow-loss, nonlinear photonic integrated circuits,” Communications Physics 5(1), 84 (2022).

112 B. Pan, H. Liu, Y. Huang et al., “Perspective on lithium-niobate-on-insulator photonics utilizing the electro-optic and acousto-optic effects,” ACS Photonics 10(7), 2078-2090 (2023).

113 A. S. Andrushchak, B. G. Mytsyk, H. P. Laba et al., “Complete sets of elastic constants and photoelastic coefficients of pure and MgO-doped lithium niobate crystals at room temperature,” Journal of Applied Physics 106(7), (2009).

114 C. C. Rodrigues, N. J. Schilder, R. O. Zurita et al., “On-Chip Cross-Polarization Backward SBS in Lithium Niobate Waveguides,” arXiv preprint arXiv: 2311. 18135 (2024).

115 S. Hou, H. Hu, Z. Liu et al., “High-Speed Electro-Optic Modulators Based on Thin-Film Lithium Niobate,” Nanomaterials 14(10), 867 (2024).

116 T. Zhang, K. Yin, C. Zhang et al., “Integrated Electro-Optic Frequency Combs: Theory and Current Progress,” Laser & Photonics Reviews 230136 (2024).

117 M. Garrett, Y. Liu, M. Merklein et al., “Integrated microwave photonic notch filter using a heterogeneously integrated Brillouin and active-silicon photonic circuit,” Nature Communications 14(1), 7544 (2023).